UNIVERSITY OF CALIFORNIA SAN DIEGO

Transparent and flexible microelectrode arrays based on graphene for multimodal neural interfaces

A dissertation submitted in partial satisfaction of the requirements for the degree Doctor of Philosophy

in

Electrical Engineering (Medical Devices and Systems)

by

Yichen Lu

Committee in charge:

Professor Duygu Kuzum, Chair
Professor Takaki Komiyama
Professor Yu-hwa Lo
Professor Tse Nga Ng
Professor Piya Pal

2021

The dissertation of Yichen Lu is approved, and it is acceptable in quality and form for publication on microfilm and electronically.

University of California San Diego

2021

TABLE OF CONTENTS

LIST OF FIGURES

LIST OF TABLES

LIST OF SUPPLEMENTARY FILES

Supplementary Movies.zip

- Supplementary Movie 2.1
- Supplementary Movie 2.2
- Supplementary Movie 2.3
- Supplementary Movie 3.1
- Supplementary Movie 3.2
- Supplementary Movie 3.3

ACKNOWLEDGEMENTS

I would like to thank my PhD advisor, Prof. Duygu Kuzum, for leading me into the field of device fabrication and neuroscience since I joined her projects at University of Pennsylvania. It was also a great opportunity for me to start my PhD program in her research group at University of California, San Diego. I am truly grateful for her patience, encouragement, and financial support during my years in her group. Additionally, I am grateful for the valuable collaboration with Prof. Takaki Komiyama and Prof. Anna Devor at University of California, San Diego, Prof. Attila Losonczy at Columbia University, and Prof. Martin Thunemann at Boston University.

I appreciate my lab mates and colleagues for their support. In particular, I would like to thank Xin Liu for his tireless data analysis and Chi Ren for her dedication in animal experiments. Jeong-Hoon Kim, Madison Wilson, and David Ding helped me with device fabrication and characterization. Yuhan Shi and Sangheon Oh introduced me to non-volatile memory device.

Last but not least, I could not have accomplished my PhD research without the support from my family back home, and my friends here in the United States of America.

Chapter 1 and Chapter 5 are in part a reprint of Y. Lu, X. Liu, D. Kuzum, Graphene-based neurotechnologies for advanced neural interfaces. Current Opinion in Biomedical Engineering 6, 138-147 (2018). The dissertation author was the first author of this article.

Chapter 2 is a reprint of M. Thunemann, Y. Lu, X. Liu, K. Kılıç, M. Desjardins, M. Vandenberghe, S. Sadegh, P. A. Saisan, Q. Cheng, K. L. Weldy, H. Lyu, S. Djurovic, O. A. Andreassen, A. M. Dale, A. Devor, D. Kuzum, Deep 2-photon imaging and artifact-free optogenetics through transparent graphene microelectrode arrays, Nature Communications 9 (1), 2035 (2018). The dissertation author was the co-first author of this article.

Chapter 3 is a reprint of Y. Lu, X. Liu, R. Hattori, C. Ren, X. Zhang, T. Komiyama, D. Kuzum, Ultralow Impedance Graphene Microelectrodes with High Optical Transparency for Simultaneous Deep Two-Photon Imaging in Transgenic Mice, Advanced Functional Materials 28, 1800002 (2018). The dissertation author was the first author of this article.

Chapter 4 is a reprint of X. Liu, C. Ren, Y. Lu, Y. Liu, J. Kim, S. Leutgeb, T. Komiyama, D. Kuzum, Multimodal neural recordings with Neuro-FITM uncover diverse patterns of cortical-hippocampal interactions, Nature Neuroscience, accepted (2021). The dissertation author was the co-first author of this article.

VITA

2013 Bachelor of Engineering, Sun Yat-sen University

2016 Master of Science in Engineering, University of Pennsylvania

2021 Doctor of Philosophy, University of California San Diego

ABSTRACT OF THE DISSERTATION

Transparent and flexible microelectrode arrays based on graphene for multimodal neural interfaces

by

Yichen Lu

Doctor of Philosophy in Electrical Engineering (Medical Device and Systems)

University of California San Diego, 2021

Professor Duygu Kuzum, Chair

The advancement of neuroscience research often requires recording of complex neural activities at high spatiotemporal resolution. Electrophysiology, being the backbone of neuroscience for decades, has the advantage of high temporal resolution, yet lacks the high spatial resolution of fluorescent imaging at single cell level. On the other hand, fluorescent imaging suffers from low temporal resolution due to the slow kinetics of the indicators. Recently, optogenetics revolutionized the capacity to control selective neural populations and provides researchers with unprecedented opportunities to investigate the causal relationships among different brain circuits. However, the traditional neural electrode arrays based on silicon and noble metals are opaque and hence not suitable to integrate electrophysiology and optical modalities.

This dissertation presents a novel transparent microelectrode array based on graphene that demonstrates crosstalk-free integration of electrophysiology, calcium imaging, and optogenetics in *in vivo* experiments on mice models.

Chapter 1 reviews the recent progress in the field of graphene-based neurotechnology. Graphene is widely used for microelectrodes, field effect transistors, chemical sensing, and cell culture applications owing to its flexibility, transparency, high conductivity, low noise, and biocompatibility.

Chapter 2 presents a novel transparent graphene microelectrode array designed for multimodal neural interfaces. The fabrication process was designed to avoid crack formation and organic residue, which is essential to eliminate light-induced artifacts. *In vivo* experiments were conducted to demonstrate a crosstalk-free integration of electrophysiology, optical imaging, and optogenetics for the first time.

Chapter 3 demonstrates that electrochemical impedance of graphene is fundamentally limited by the quantum capacitance. To overcome such limit, we created an alternative conduction path with electrochemically deposited platinum nanoparticles and reduced the impedance by 100-fold while maintaining high transparency.

Chapter 4 presents a flexible implantable transparent microelectrode array that enables simultaneous electrical recordings from hippocampus during optical imaging of neural activity across large areas. Our neural probe has three advantages, flexibility, transparency, and shuttle-free implantation. We demonstrated seamless integration of simultaneous wide-field fluorescence imaging of the cortex with electrical recordings from the hippocampus.

Chapter 5 is the conclusion of this dissertation. The outlook and roadmap of graphene-based neurotechnology for both neuroscience research and medical applications are discussed.

Chapter 1. Graphene-based Neurotechnologies for Advanced Neural Interfaces

1.1 Abstract

Understanding how neuron populations process information by transforming activities of individual neurons into complex behaviors is one of the biggest challenges of neuroscience research. Studying neuronal dynamics is also critical for understanding circuit dysfunctions in neurological disorders and developing effective targeted treatments for them. Unraveling the functions of neural circuits requires monitoring and controlling neural activity with high spatial and temporal resolution. To this end, multifunctional neurotechnologies combining electrical, optical and chemical sensing and stimulation modalities have been proposed to overcome resolution limits. Research in multifunctional probes has fueled the demand for new materials, which can combine multiple sensing or stimulation functionalities, while providing a minimally invasive chronic interface to the brain. Graphene has recently emerged as a neural interface material offering several outstanding properties, such as optical transparency, flexibility, high conductivity, functionalization and biocompatibility. The unique combination of these properties in a single material system makes graphene an attractive choice for multi-modal probing of neural activity. In this review, we discuss recent advances in graphene-based neurotechnologies, highlight different approaches and consider emerging directions inspired by unique characteristics of graphene.

1.2 Introduction

The complexity of neural activities has challenged both neuroscience research and clinical practice for decades. It is estimated that human brains consist of 86 billion neurons and quadrillions of synapses [1]. Understanding neuronal dynamics and information processing performed by

neural populations requires advanced technologies with high-resolution sensing and stimulation capability. Clinical neuromodulation therapies widely used for neurological disorders also depend on the ability to manipulate the dynamics of neural circuits. Conventional neural interfaces offering electrical, optical, or chemical signals have greatly advanced our understanding of neural functions, however, most of these technologies are based on a single functionality. Combining multiple functionalities in a single system has recently been pursued as an integrative approach in new neurotechnology development.

Recently, graphene has drawn tremendous attention in neuroscience research owing to its flexibility, transparency, high conductivity, low noise, and biocompatibility [2-4]. This two-dimensional single-atom thick material, awarded Nobel Prize in Physics in 2010, has already shown to be promising for various neurotechnology applications including multimodal interfaces and closed-loop systems [5-10]. To-date, graphene has been used either passively in various microelectrode array configurations or actively in transistors. The primary signals detected and recorded by graphene neural interfaces are categorized as electrical, such as local field potentials, and chemical, such as neurotransmitter concentration. In Section 1.3, we first review the state-of-the-art designs for graphene-based neural interfaces and evaluate their advantages for different applications. Then in section 1.4 and 1.5, we discuss future directions and potential advances for graphene-based neurotechnologies in both basic neuroscience research and medical applications.

1.3 State-of-the-art Graphene-based Neurotechnologies

In this section we discuss recent work and literature on graphene-based microelectrodes, graphene field effect transistors for neural interfaces and the functionalization of graphene for chemical sensing, all of which are made possible because of the biocompatibility of graphene and its derivatives.

1.3.1 Graphene-based Microelectrodes

Electrophysiology has been the backbone of neuroscience research for several decades. It has led to numerous discoveries relating single-cell response to behavioral outcomes [2,11]. Although electrophysiological recordings have the unique advantage of high temporal resolution in monitoring neural activity, the major limitation towards studying neural circuits is inability of sampling large number of neurons (~1000 cells) in neuronal populations. Last decade has witnessed rapid advancements in optical imaging methods for monitoring neural tissue. Fluorescence imaging extended the capabilities for monitoring hundreds of cells densely packed in local neuronal microcircuits. Furthermore, there has been significant progress in development of genetically encoded calcium indicators, enabling *in vivo* studies over weeks. The major drawback of cellular imaging is the poor temporal resolution due to slow kinetics of the indicators and low frame acquisition rates of microscopy systems [12,13]. Optical imaging and electrophysiological recordings can nicely complement each other as the weaknesses of one can be addressed by the strengths of the other [14]. However, conventional metal microelectrode arrays cannot be used for simultaneous optical imaging since they block the field of view, generate shadows, and cause light-induced artifacts in neural recordings [5,8]. In order to overcome this limitation, transparent flexible microelectrode arrays graphene have been proposed. The optical transparency of graphene arrays enables simultaneous electrophysiological recordings and calcium imaging [5,15].

Recent *in vitro* work with hippocampal slices reported that high frequency population bursts could be detected with the graphene electrodes while visually resolving the neural network and identifying the exact location of the active neurons with calcium fluorescence microscopy [5]. Figure 1.1A-a shows a steady-state fluorescence image of dentate gyrus, captured through the

graphene electrode (the black square). Recordings with the graphene electrode (Figure 1.1A-b) exhibited population bursts, while calcium transient peaks ($\Delta F/F_0$) (Figure 1.1A-c) showed activity levels and spatial locations of individual cells (cell 1-6) overlapping with the graphene electrode. The temporal resolution of recordings with the graphene electrode enables detection of high frequency population spikes, which cannot be resolved by the calcium fluorescence responses. In contrast, calcium imaging responses captures complex network contributions of individual neurons, which are not evident in the electrical recordings. To illustrate, Figure 1.1A-c shows that most of the cells (cell 1-6) contribute to population bursts. However, cell 2 and cell 3 selectively responds to some of the population bursts and the peak amplitude of their response for each event varied [5]. Similarly, the transparent graphene electrode arrays were also used in conjunction with simultaneous wide-field calcium imaging in awake mice (Figure 1.1A-d). Electrical recordings synchronized with wide-field calcium imaging serves as a gold standard to confirm that wide-field calcium response was a good proxy for local activities of individual cortical modules [15].

In addition to calcium imaging, optogenetic modulation was also integrated with graphene electrode recordings [9,10]. The electrode array based on 4 layers of chemical-vapor-deposited (CVD) graphene allowed electrophysiological recording of neural activities activated by blue light of 473 nm wavelength in transgenic mice expressing channelrhodopsin-2. The biological responses induced by optogenetic stimulation were clearly detected with spatial distributions after a stimulus of 3 ms duration, however, as shown in the post-mortem control data (Figure 1.1B), the significant light-induced artifacts were observed, possibly due to increased absorption by multiple layers of graphene or relatively high impedance [9], which can be mitigated by using monolayer graphene or reducing impedance [6]. A more recent study has shown that careful design of key steps in the fabrication process for transparent graphene electrodes can mitigate the light-induced

artifact problem and that virtually artifact-free local field potential recordings can be achieved within operating light intensities for optogenetic stimulation [16]. The same study has demonstrated that transparent graphene microelectrode arrays enable crosstalk-free integration of 2-photon microscopy, optogenetic stimulation, and cortical recordings in the same in vivo experiment by eliminating light-induced artifacts.

Although previous work has demonstrated that the microelectrode arrays based on CVD graphene could record local field potentials with high signal-to-noise ratio (SNR) of 40.8 [5], the impedance of monolayer graphene is relatively high compared to other faradaic or porous electrode materials. Chemical doping of graphene with nitric acid has shown to decrease the impedance up to 50% [5,17], nevertheless the lack of faradaic reactions as indicated by cyclic voltammetry [2,5,9] limits further decrease of the impedance and impedes scaling down the electrode dimensions to the single-cell size for high spatial resolution.

Reduction in impedance is also crucial for employing monolayer graphene for neural stimulation. Neural stimulation is widely used for mapping cortical regions in clinical practice. Although monolayer graphene provides numerous desirable characteristics for neural recording and imaging, the charge injection capacity of monolayer graphene electrodes is not sufficient to evoke electrical responses. Porous graphene consisting of 3D flakes of multi-layer graphene and graphene oxide was suggested as an electrode material to fabricate low impedance and high charge injection capacity microstimulation electrodes [7]. One of the major advantages of porous graphene is the simple and scalable fabrication in large areas. 3D porous graphene layers can be formed on standard polyimide substrates using CO_2 laser pyrolysis [18]. Most of the coatings that are used for reducing impedance suffer from delamination problems particularly when used for current stimulations. The porous graphene layers are grown from the polyimide substrate itself by

pyrolysis, providing strong adhesion. Bench tests in phosphate buffered saline demonstrated that porous graphene does not exhibit any degradation or delamination after over 1 million cycles of biphasic current stimulation [7]. 3D porous structure and extremely large effective surface area provides high charge injection capacity (3.1 mC cm^{-2}), enabling high efficiency cortical microstimulation. In *in vivo* experiments with rodents, high density porous graphene arrays placed over motor cortex arrays were used to control leg muscle movement with high precision without penetrating to layer V (Figure 1.1C). High-resolution cortical microstimulation with porous graphene arrays could be utilized as a minimally invasive alternative to penetrating arrays for neural prosthesis and brain computer interface applications. Furthermore, capacitive charge transfer characteristics of porous graphene eliminates potentials risks of electrode corrosion or toxicity due to redox reactions, which are significant concerns for faradaic stimulation electrodes [2,19].

In addition to monolayer graphene and porous graphene, freestanding electrodes fabricated from liquid-crystal graphene oxide (Figure 1.1D) was shown to exhibit very high charge injection capacity (46±2.9 mC cm^{-2}) [20]. *In vitro* studies demonstrated successful stimulation of retinal ganglion cells. Both porous graphene and reduced liquid crystal graphene oxides mainly benefit from large effective surface area leading to low impedance and high charge injection capacity, important for high fidelity neural sensing and stimulation.

1.3.2 Graphene Field Effect Transistors

Graphene field effect transistors (GFET) have been investigated for neural sensing and stimulation experiments [21]. In a GFET, graphene is used as the gate material in contact with brain tissue, and the gate bias is applied though a reference electrode, typically made of Ag/AgCl, as shown in Figure 1.2A. The type and concentration of the charge carriers, and hence the

conductivity of graphene, can be modulated by shifting the potential at the graphene-electrolyte interface as illustrated in the schematic band diagram in Figure 1.2B. *In vitro* studies have investigated the impact of substrate materials (SiO_2/Si, sapphire, and polyimide) on the transconductance. GFETs on polyimide substrate demonstrate higher transconductance (1.9 $mS \cdot V^{-1} \cdot sq$) than those on SiO_2/Si (0.63 $mS \cdot V^{-1} \cdot sq$) and sapphire (0.36 $mS \cdot V^{-1} \cdot sq$) [22]. The representative recording is shown in Figure 1.2C.

The advantage of a transistor configuration is the intrinsic amplification effect, which leads to a higher SNR than the electrodes [23,24]. Compared with Pt electrodes (effective area 1962 μm^2), GFETs (effective area 300 μm^2) has a competitive average SNRs of 62±5.8 for pre-epileptic activities and 9.85±0.67 for spontaneous oscillations in visual cortex as to 53±11 and 8.33±1.05 for Pt electrodes respectively during *in vivo* recording, yet much smaller size [24]. Although transistor configuration has inherent signal amplification advantage, applied gate biases (commonly above 100 mV) constitutes a potential risk for direct uncontrolled current leakage to the brain, which may result in undesired side effects or tissue damage based on the current amplitude. Therefore, passive microelectrode arrays are the common choice of neural interface particularly for medical applications.

1.3.3 Functionalized Graphene for Chemical Sensing

The concentrations of certain biomolecules, such as neurotransmitters, have critical influence on the chemical processes and biological reactions in nervous systems. Others, such as H_2O_2, the by-product of neurotransmission can be used as the indicators for disease diagnosis. Therefore, sensitive and selective biochemical sensors are highly in need for both neuroscience research and medical applications. To this end, graphene-based neural interfaces with chemical sensing capability have been investigated using three different approaches: graphene field effect

transistors [4,25-27], graphene oxide electrodes [28-35], and optical graphene oxide assays [36-38], all of which take advantages of the easy functionalization of graphene and its derivatives [39].

In a graphene field effect transistor, the functionalization immobilizes the receptor on the surface of monolayer graphene via a linker molecular. When the receptor bonds with the target, the Dirac point of the functionalized graphene shifts. The device is then characterized to get the response calibration curve; thus, the shift of Dirac point indicates the concentration of the targets. The target-receptor pair must be carefully chosen and tested with control group to ensure the selectivity of the sensing [4]. Chemical sensing based on functionalized graphene field effect transistors has been investigated to detect neurotransmitters, and the limits of detection (LOD) were reported as 0.5 μM for acetylcholine [25], 5 μM for glutamate [26], and 10 pg/mL for opioid [27].

Alternatively, when electrode configuration is used, graphene oxides can be functionalized as the electrode materials for electrochemical sensing [39]. The electro-catalytic ability of functionalized graphene oxide is utilized to enhance the oxidation/reduction of the analyte, and the electrochemical response can be measured with voltammetry. Neurotransmitters, such as dopamine and acetylcholine are chemically active and can be reduced and oxidized at specific potentials, therefore, electrochemical sensors are considered the most effective approach for detecting dopamine [28-31] and acetylcholine (ATCh) [32-34]. The first dopamine sensor based on graphene was developed in 2009 with a LOD of 5 μM [28]. The lowest LOD of 2.3 nM for dopamine sensing was achieved with nanocomposite film consisting of ionic liquid functionalized graphene oxide and gold nanoparticles in 2017, and a linearly relation between the current response and dopamine concentration from 7 nM to 5 μM was demonstrated as well. Other compounds including amino acid, glucose, uric acid, epinephrine, and serotonin did not interfere with the

response current even at 40 -100 times concentration as dopamine, proving the high selectivity [31]. On the other hand, the lowest LOD for acetylcholine was reported to be 4 nM with a response time less than 4 seconds [34]. Similarly, as a by-product of neurotransmission, H_2O_2 can be used as an indicator during stroke attacks. Implantable H_2O_2 sensor based on reduced graphene oxide and gold nanoparticles demonstrated fast response (<5s) and low LOD (0.63 µM), providing a reliable platform for *in vivo* H_2O_2 detection in a hyperacute stroke model [35].

Furthermore, graphene oxides exhibit fluorescence and photoluminescence in the visible and near-infrared range, whose quenching and "turn-on" effects can be employed for neural interfaces as well [36-38]. Combined with 3D two-photon excitation, graphene oxide/aptamer conjugate was demonstrated to detect ATP at a concentration range of 10 µM – 3 mM *in vitro* and within a tissue depth of 0 – 270 µm *in vivo* [37]. Similarly, graphene oxide functionalized with nitrotriacetic acid and Cu^+ ion was designed as a selective detector for norepinephrine, where four other neurotransmitters, dopamine, ATP, ADP, and glutamic acid were used as negative controls. The reported detector showed at least one order of magnitude higher luminescent response to norepinephrine than the others in the control group. And the LOD was as low as 10.1 nM [38]. The materials, methods and specifications of graphene functionalization for chemical sensing discussed in this section are summarized in Table 1.1.

1.3.4 Biocompatibility of Graphene

Biocompatibility has been one of the biggest challenges in developing chronic implantable neural interfaces. Biocompatibility is especially important to prevent the undesirable tissue reactions, such as inflammatory responses. So far, the biocompatibility of graphene has been investigated by utilizing direct cell-to-graphene interfaces, where the cellular survival rates and activities are compared with other commonly used substrates [40-44]. In *in vitro* studies,

monolayer CVD graphene substrates were compared with glass slides (control) for human neural stem cell (hNSC) cultures. After one month *in vitro*, the hNSCs cultured on graphene had a significantly higher density (352±20 cells/mm^2) than those on glass (178±27 cells/mm^2) owing to the enhanced adhesion of hNSCs on graphene. Compared to glass substrate, monolayer CVD graphene substrate also increased the probability for hNSCs to differentiate toward neurons rather than glial cells, which is desirable for neural regenerative medicine [43]. A similar study compared graphene-based substrate with peptide-free and polyornithine-covered glass slides (control) for hippocampal neuronal cultures. Over 8 – 10 days *in vitro*, neuronal cell density, starting from 30 cells/mm^2, increased to 104 cells/mm^2 on graphene and to 91 cells/mm^2 on glass substrate. More importantly, the physiological neuronal activities, including the spontaneous postsynaptic currents, synaptogenesis, and short-term synaptic plasticity, were not perturbed by the graphene in comparison to the control group [44].

In addition to planar substrates, 3D biocompatible scaffolds based on graphene and/or its derivatives were developed for tissue engineering [45-48]. Graphene oxide (GO) was investigated as a bio-functioning agent in polyethylene glycol diacrylate hydrogel (PEGDA) scaffold to enhance the viability and osteogenic differentiation of human adipose-derived stem cells (hADSCs). Over 3 weeks *in vitro*, DNA contents of hADSCs in GO-functionalized PEDGA remained stable whereas those in PEGDA decreased after week 2. And at the end of week 3, the messenger RNA expression of osteogenic markers that indicated undergoing osteogenic differentiation was also larger in GO-functionalized PEGDA than in PEGDA alone [46]. In summary, graphene and its derivatives have been demonstrated as biocompatible scaffold materials to enhance cell proliferation and differentiation, suggesting its high potential as a chronic implant material.

Longevity and bio-stability of graphene is particularly important for chronic studies and long-term implants. Most of the published work on graphene neurotechnologies report acute studies with animal models. However, cell culture studies have demonstrated promising bio-stability results on graphene-based substrate for up to one month [43]. For graphene neurotechnologies based on monolayer graphene bio-stability is less of a concern since graphene layer is not free floating and mostly encapsulated by polymer insulators. On the other hand, porous graphene consists of multilayer graphene flakes randomly orientated in a 3D structure. Further studies are needed to assess long-term biocompatibility in animal models, although biocompatibility in cell cultures have already shown promising results [45].

1.4 Future Directions

The advance of neuroscience research benefits from different types of neural technologies but is also limited by their individual drawbacks. Electrophysiology has been widely used in neuroscience research and clinical practice for decades. It has high temporal resolution providing detection of fast events lasting sub-milliseconds but poor spatial resolution due to 3D inaccessibility of the brain and spatial averaging and filtering in the tissue. On the other hand, optical imaging provides superior single-cell level spatial resolution in monitoring activities of hundreds of neurons simultaneously but poor temporal resolution due to slow kinetics of indicators and low frame acquisition rates of imaging systems [13]. Additionally, optogenetics has revolutionized the neuroscience research, providing fast selective optical modulation of specific neuron populations. By leveraging the advantages of individual techniques, the combination of electrophysiology with optical modalities, such as optical imaging and optogenetics, can significantly facilitate the investigation of neural circuit functions, the role of different cell types in neural oscillations and various neural circuit mechanisms including adaptation and plasticity. In

this section, we will discuss the promising applications of graphene microelectrodes as multimodal neural interfaces and their potential advantages in both neuroscience research and clinical practice.

1.4.1 Closed-loop Devices and Multimodal Neural Interface

Understanding the input-output relationships of neural circuits requires precise perturbation and monitoring of neural population activities. To facilitate such studies, closed-loop systems have been proposed to integrate electrophysiology for fast read-out and optogenetics for effective modulation of the neural populations [14,49,50]. The system changes the optical stimulation parameters dynamically according to the real-time monitored electrical activities of neurons in order to study the mechanisms of neuronal disorders and to investigate causal relationships between different brain circuits [49,51]. However, all closed-loop optogenetic systems to-date use conventional metal neural electrodes and are not suitable for applications involving simultaneous optical modalities due to the non-transparency and light-induced artifacts. Attributed to photothermal heating and Becquerel effect [52,53], these light-induced artifacts interfere with the biological signals and require sophisticated hardware and software signal processing algorithms to remove from the recordings. To this end, the monolayer CVD graphene electrode has been demonstrated as an artifact-free multimodal interface to integrate electrophysiology with optogenetics [6,8,16]. The optical stimuli can pass through transparent graphene electrodes to the neural population right beneath the electrode contacts (Figure 1.3A) without causing any light-induced artifacts (Figure 1.3B). As shown in Figure 1.3C, a compact system is developed to integrate the graphene micro-electrodes array with an optical fiber for closed-loop operation. The simplified hardware configuration minimizes the interference of animal behaviors and therefore significantly facilitates the long-term studies on neural circuit functions of freely moving animals [6]. The system implements a voltage threshold detection algorithm and is

validated for different frequencies that are typical in neural recordings (Figure 1.3D). The system has a broad sampling frequency range of 1 kHz – 30 kHz and demonstrates a fast-optical response with a sub-millisecond time delay. Graphene-based multimodal neural interfaces, integrating high resolution optical imaging, optogenetics stimulation and electrical recordings can open up new opportunities to investigate the brain mechanisms in multiple spatial and temporal scales, from single neurons to local networks, and even different cortical regions.

1.4.2 Medical Applications

In addition to basic neuroscience research, graphene has also been considered for medical technologies, including implantable devices, disease diagnosis, and therapeutic efficacy [3]. For example, Graphene Flagship funded by the European Union dedicates a special Work Package, Biomedical Technologies to develop the clinical products [54]. These potential clinical applications can benefit from various advantages of graphene. First, graphene tissue interface is capacitive. Corrosion of the electrode, a common issue of the faradaic stimulation electrodes, is thus eliminated. Therefore, the graphene electrodes can be employed for chronic brain-machine interfaces and neural prostheses that require safe and durable neural recording and stimulation in humans. Secondly, with the high selectivity, low limits of detection and the real-time detection capability as mentioned in Section 1.3.3, graphene chemical sensors have great potential in disease diagnosis and monitoring. Thirdly, graphene-based scaffolds, with the outstanding ability to facilitate cell proliferation and differentiation, have recently attracted increasing attention for tissue engineering and regenerative medicine [43,55,56]. Furthermore, the application of closed-loop devices and multimodal neural interfaces based on transparent graphene microelectrode array in animal models will facilitate a better understanding of neural mechanisms underlying

electrocorticography and electroencephalography, commonly used neural recording techniques with human patients in clinical settings.

1.5 Acknowledgement

We would like to acknowledge Office of Naval Research Young Investigator Award (N00014161253), National Science Foundation (ECCS-1752241, ECCS-1734940), San Diego Frontiers of Innovation Scholars Program, and Kavli Institute for Brain and Mind Innovative Research for funding this research.

Chapter 1 is in part a reprint of Y. Lu, X. Liu, D. Kuzum, Graphene-based neurotechnologies for advanced neural interfaces. Current Opinion in Biomedical Engineering 6, 138-147 (2018). The dissertation author was the first author of this article.

1.6 Figures

Figure 1. 1 Graphene-based Electrodes.

(A) Simultaneous *in vitro* electrophysiology and calcium imaging of a hippocampal slice (a-c) [5], copyright 2014 Springer Nature, wide-field calcium imaging in awake mice model and synchronized calcium fluorescent response and electroencephalographical recording (d) [13], copyright 2017 Elsevier. (B) The structure of the transparent flexible graphene electrode (top panel), fluorescent image of blood vessels under the transparent electrode array (bottom left panel), and electrical recording (bottom right panel) [14,15], copyright 2014 Springer Nature. (C) Scanning microscopic image of 8-by-8 laser-induced graphene array (top left panel), spatial distribution and time latency of *in vivo* electrical recording (top right panel), scheme for *in vivo* electrical stimulation (bottom left panel), and leg flexion (bottom right panel) [7], copyright 2016 Springer Nature. (D) Freestanding electrodes based on reduced graphene oxide with high charge injection capacity for neural stimulation [19], copyright 2015 John Wiley and Sons.

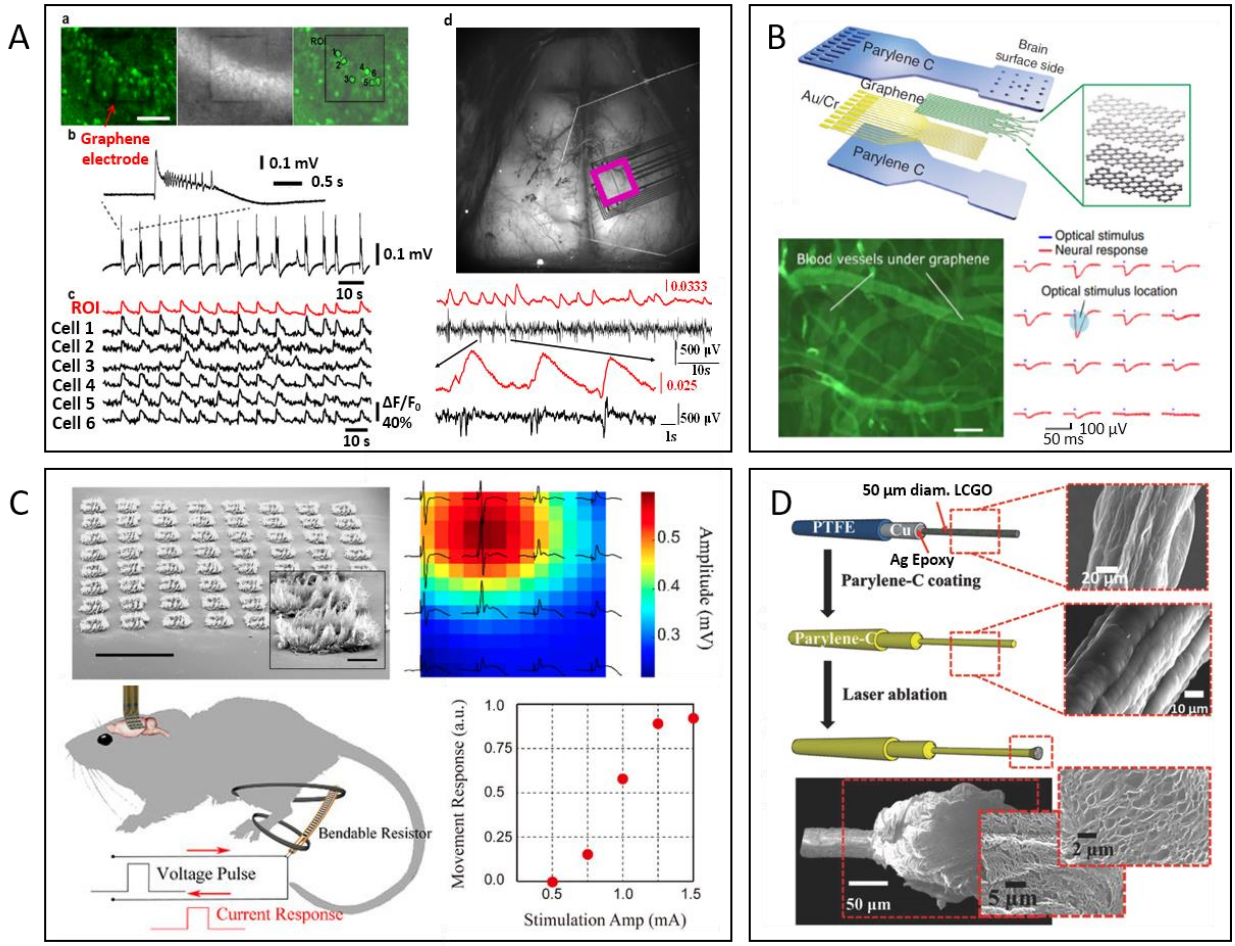
A
a
Graphene electrode
b
0.1 mV
0.5 s
0.1 mV
10 s
c
ROI
Cell 1
Cell 2
Cell 3
Cell 4
Cell 5
Cell 6
ΔF/F0
40%
10 s
d
0.0333
500 µV
10s
0.025
500 µV
1s
B
Parylene C
Brain surface side
Graphene
Au/Cr
Parylene C
Blood vessels under graphene
Optical stimulus
Neural response
Optical stimulus location
100 µV
50 ms
C
0.5
0.4
0.3
Amplitude (mV)
Bendable Resistor
Voltage Pulse
Current Response
Movement Response (a.u.)
1.0
0.75
0.5
0.25
0.0
0.5
1.0
1.5
Stimulation Amp (mA)
D
50 µm diam. LCGO
PTFE
Cu
Ag Epoxy
Parylene-C coating
20 µm
Parylene-C
Laser ablation
10 µm
2 µm
50 µm
5 µm

Figure 1. 2 Graphene Field Effect Transistors.

(A) Monolayer graphene is used as the gate material. When graphene is immersed in electrolytic solution, ions accumulate at the surface of graphene. This phenomenon is termed electrical double layer. The gate voltage is applied with a reference electrode [22], copyright 2014 IEEE. (B) Schematic band diagram of graphene-electrolyte interface. The type and concentration of charge carriers can be adjusted by shifting the gate bias [20], copyright 2013 IEEE. (C) Action potentials of HL-1 cells recorded *in vitro*, the time latency and spatial propagation is demonstrated in the middle and the right panels [21], copyright 2017 IEEE.

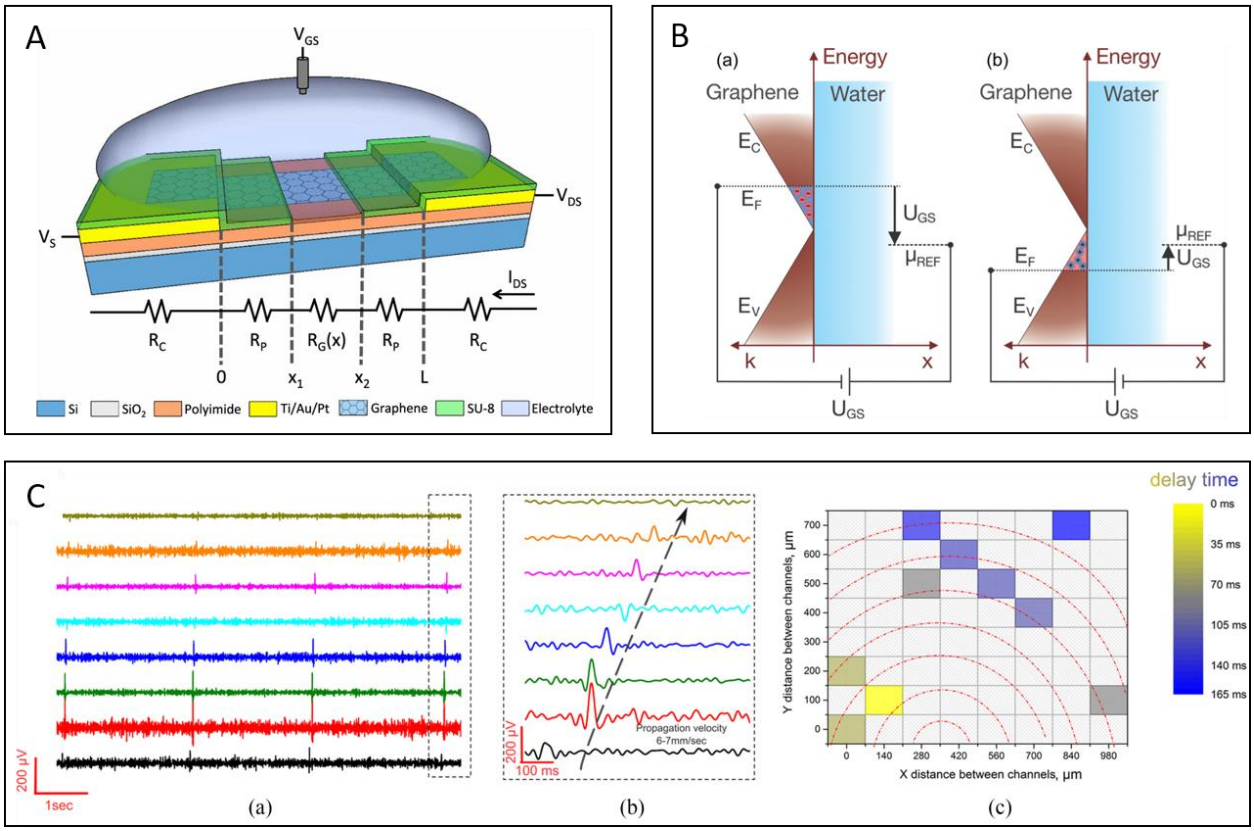
A
V_{GS}
V_{DS}
V_S
I_{DS}
R_C
R_P
$R_G(x)$
R_P
R_C
0
x_1
x_2
L
Si
SiO_2
Polyimide
Ti/Au/Pt
Graphene
SU-8
Electrolyte
B
(a)
Energy
Graphene
Water
E_C
E_F
E_V
U_{GS}
μ_{REF}
k
x
U_{GS}
(b)
Energy
Graphene
Water
E_C
E_F
E_V
μ_{REF}
U_{GS}
k
x
U_{GS}
C
200 μV
1sec
(a)
200 μV
100 ms
Propagation velocity
6-7mm/sec
(b)
delay time
0 ms
35 ms
70 ms
105 ms
140 ms
165 ms
Y distance between channels, μm
0
100
200
300
400
500
600
700
X distance between channels, μm
0
140
280
420
560
700
840
980
(c)

Figure 1. 3 Closed-loop Devices.

(A) The structure of a transparent flexible array showing graphene contacts, gold wires, a PET substrate, and encapsulation (left panel) and a photo of the flexible array. The inset shows the transparent recording area (right panel). (B) The power spectrum of recorded electrical signal under 10 Hz optogenetics stimulation for Au control electrode (left panel) and graphene electrode (right panel). (C) A picture of the closed-loop system consisting of a transparent graphene array and fiber-coupled μLED. (D) The test setup for the closed-loop system (left panel) and typical real-time recording data for one channel (right panel). A train of 10 Hz pulses (10 ms pulse duration) modulated by a 2 Hz sine wave was applied to the saline and the threshold was set to 200μV [6], copyright 2017 IEEE.

A

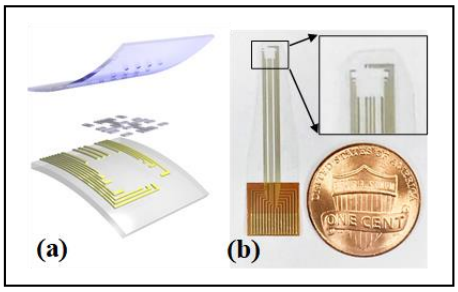
(a)
(b)
ONE CENT

B

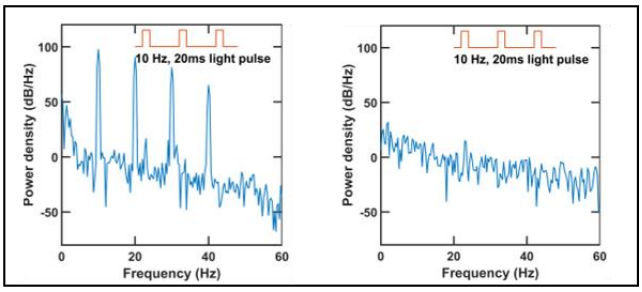
10 Hz, 20ms light pulse
Power density (dB/Hz)
Frequency (Hz)
10 Hz, 20ms light pulse
Power density (dB/Hz)
Frequency (Hz)

C

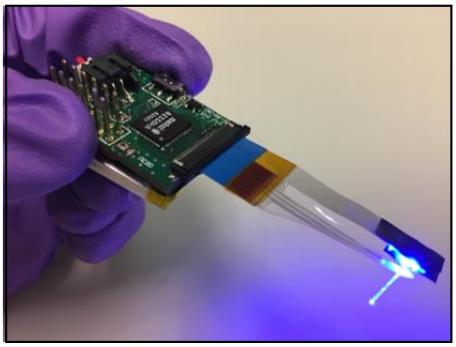

D

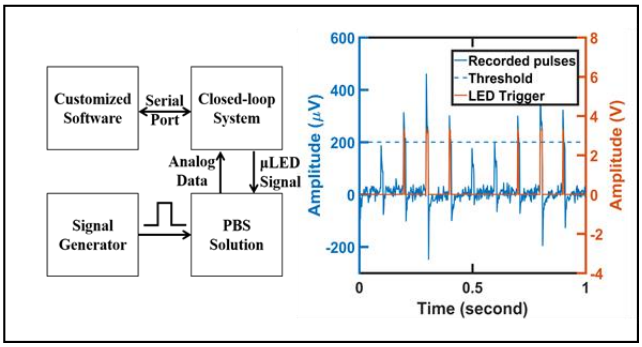
Customized Software
Serial Port
Closed-loop System
Analog Data
µLED Signal
Signal Generator
PBS Solution
Recorded pulses
Threshold
LED Trigger
Amplitude (µV)
Amplitude (V)
Time (second)

Table 1. 1 Functionalized graphene for chemical sensing

Materials	Analyte	Methods	LOD	Range	Reference
Pt-graphene	ATCh	Electrochemical	5 nM	5 nM – 700 μM	[32]
Fe_3O_4-PEDOT-GO	ATCh	Electrochemical	4 nM	4 nM – 800 μM	[33]
rGO-Chitosan	Dopamine	Electrochemical	5 μM	5 μM – 200 μM	[28]
GO-Au	Dopamine	Electrochemical	1.28 μM	1.28 – 30 μM	[29]
PEDOT-GO	Dopamine	Electrochemical	85 nM	85 nM – 10 μM	[30]
GO-Au	Dopamine	Electrochemical	2.3 nM	2.3 nM – 5 μM	[31]
rGO-Au_2O_3	H_2O_2	Electrochemical	0.63 μM	0.63 μM – 8 mM	[35]
GO-Aptamer	ATP	Optical	10 μM	10 μM – 3 mM	[37]
Cu-NTA-GO	Norepinephrine	Optical	10.1 nM	10.1 nM – 100 μM	[38]
PhO-dex-GO	AChE inhibitor	Optical	28.55 nM	28.55 – 372 nM	[36]
CVD graphene	ATCh	FET	0.5 μM	0.5 μM – 2 mM	[25]
CVD graphene	Opioid	FET	10 pg/mL	10 pg/mL – 10 ug/mL	[29]
CVD graphene	Glutamate	FET	5 μM	5 μM – 1.2 mM	[26]

1.8 Reference

1 Herculano-Houzel, S. The remarkable, yet not extraordinary, human brain as a scaled-up primate brain and its associated cost. *Proceedings of the National Academy of Sciences* **109**, 10661-10668, doi:10.1073/pnas.1201895109 (2012).

2 Ferro, M. D. & Melosh, N. A. Electronic and Ionic Materials for Neurointerfaces. *Advanced Functional Materials* **28**, 1704335 (2018).

3 Kostarelos, K., Vincent, M., Hebert, C. & Garrido, J. A. Graphene in the Design and Engineering of Next - Generation Neural Interfaces. *Advanced Materials* **29**, 1700909 (2017).

4 Yan, F., Zhang, M. & Li, J. Solution - Gated Graphene Transistors for Chemical and Biological Sensors. *Advanced healthcare materials* **3**, 313-331 (2014).

5 Kuzum, D., Takano, H., Shim, E., Reed, J. C., Juul, H., Richardson, A. G., De Vries, J., Bink, H., Dichter, M. A. & Lucas, T. H. Transparent and flexible low noise graphene electrodes for simultaneous electrophysiology and neuroimaging. *Nature communications* **5**, 5259 (2014).

6 Liu, X., Lu, Y., Iseri, E., Ren, C., Liu, H., Komiyama, T. & Kuzum, D. Transparent artifact-free graphene electrodes for compact closed-loop optogenetics systems. *2017 IEEE International Electron Devices Meeting*, 26.21.21-26.21.24. (2017).

7 Lu, Y., Lyu, H., Richardson, A. G., Lucas, T. H. & Kuzum, D. Flexible Neural Electrode Array Based-on Porous Graphene for Cortical Microstimulation and Sensing. *Scientific reports* **6**, 33526 (2016).

8 Liu, X., Lu, Y., Iseri, E., Shi, Y. & Kuzum, D. A Compact Closed-loop Optogenetics System based on Artifact-free Transparent Graphene Electrodes. *Frontiers in Neuroscience* **12**, 132 (2018).

9 Park, D.-W., Schendel, A. A., Mikael, S., Brodnick, S. K., Richner, T. J., Ness, J. P., Hayat, M. R., Atry, F., Frye, S. T. & Pashaie, R. Graphene-based carbon-layered electrode array technology for neural imaging and optogenetic applications. *Nature communications* **5**, 1-11 (2014).

10 Park, D.-W., Brodnick, S. K., Ness, J. P., Atry, F., Krugner-Higby, L., Sandberg, A., Mikael, S., Richner, T. J., Novello, J. & Kim, H. Fabrication and utility of a transparent graphene neural electrode array for electrophysiology, in vivo imaging, and optogenetics. *Nature protocols* **11**, 2201-2222 (2016).

11 Chen, R., Canales, A. & Anikeeva, P. Neural recording and modulation technologies. *Nature Reviews Materials* **2**, 16093 (2017).

12 Stosiek, C., Garaschuk, O., Holthoff, K. & Konnerth, A. In vivo two-photon calcium imaging of neuronal networks. *Proceedings of the National Academy of Sciences* **100**, 7319-7324 (2003).

13 Badura, A., Sun, X. R., Giovannucci, A., Lynch, L. A. & Wang, S. S.-H. Fast calcium sensor proteins for monitoring neural activity. *Neurophotonics* **1**, 025008-025008 (2014).

14 Kim, C. K., Adhikari, A. & Deisseroth, K. Integration of optogenetics with complementary methodologies in systems neuroscience. *Nature Reviews Neuroscience* **18**, 222-235 (2017).

15 Makino, H., Ren, C., Liu, H., Kim, A. N., Kondapaneni, N., Liu, X., Kuzum, D. & Komiyama, T. Transformation of Cortex-wide Emergent Properties during Motor Learning. *Neuron* **94**, 880-890. e888 (2017).

16 Thunemann, M., Lu, Y., Liu, X., Kılıç, K., Desjardins, M., Vandenberghe, M., Sadegh, S., Saisan, P. A., Cheng, Q., Weldy, K. L., Lyu, H., Djurovic, S., Andreassen, O. A., Dale, A. M., Devor, A. & Kuzum, D. Deep 2-photon imaging and artifact-free optogenetics through transparent graphene microelectrode arrays. *Nature Communications* **9**, 2035 (2018).

17 D'Arsié, L., Esconjauregui, S., Weatherup, R. S., Wu, X., Arter, W. E., Sugime, H., Cepek, C. & Robertson, J. Stable, efficient p-type doping of graphene by nitric acid. *RSC Advances* **6**, 113185-113192 (2016).

18 Lin, J., Peng, Z., Liu, Y., Ruiz-Zepeda, F., Ye, R., Samuel, E. L., Yacaman, M. J., Yakobson, B. I. & Tour, J. M. Laser-induced porous graphene films from commercial polymers. *Nature communications* **5**, 5714 (2014).

19 Cogan, S. F. Neural stimulation and recording electrodes. *Annu. Rev. Biomed. Eng.* **10**, 275-309 (2008).

20 Apollo, N. V., Maturana, M. I., Tong, W., Nayagam, D. A., Shivdasani, M. N., Foroughi, J., Wallace, G. G., Prawer, S., Ibbotson, M. R. & Garrett, D. J. Soft, flexible freestanding neural stimulation and recording electrodes fabricated from reduced graphene oxide. *Advanced Functional Materials* **25**, 3551-3559 (2015).

21 Hess, L. H., Seifert, M. & Garrido, J. A. Graphene transistors for bioelectronics. *Proceedings of the IEEE* **101**, 1780-1792 (2013).

22 Kireev, D., Zadorozhnyi, I., Qiu, T., Sarik, D., Brings, F., Wu, T., Seyock, S., Maybeck, V., Lottner, M. & Blaschke, B. M. Graphene Field-Effect Transistors for In Vitro and Ex Vivo Recordings. *IEEE Transactions on Nanotechnology* **16**, 140-147 (2017).

23 Mackin, C., Hess, L. H., Hsu, A., Song, Y., Kong, J., Garrido, J. A. & Palacios, T. A current–voltage model for graphene electrolyte-gated field-effect transistors. *IEEE Transactions on Electron Devices* **61**, 3971-3977 (2014).

24 Blaschke, B. M., Tort-Colet, N., Guimerà-Brunet, A., Weinert, J., Rousseau, L., Heimann, A., Drieschner, S., Kempski, O., Villa, R. & Sanchez-Vives, M. V. Mapping brain activity with flexible graphene micro-transistors. *2D Materials* **4**, 025040 (2017).

25 Hess, L. H., Lyuleeva, A., Blaschke, B. M., Sachsenhauser, M., Seifert, M., Garrido, J. A. & Deubel, F. Graphene transistors with multifunctional polymer brushes for biosensing applications. *ACS applied materials & interfaces* **6**, 9705-9710 (2014).

26 Huang, Y., Dong, X., Shi, Y., Li, C. M., Li, L.-J. & Chen, P. Nanoelectronic biosensors based on CVD grown graphene. *Nanoscale* **2**, 1485-1488 (2010).

27 Lerner, M. B., Matsunaga, F., Han, G. H., Hong, S. J., Xi, J., Crook, A., Perez-Aguilar, J. M., Park, Y. W., Saven, J. G. & Liu, R. Scalable production of highly sensitive nanosensors based on graphene functionalized with a designed G protein-coupled receptor. *Nano letters* **14**, 2709-2714 (2014).

28 Wang, Y., Li, Y., Tang, L., Lu, J. & Li, J. Application of graphene-modified electrode for selective detection of dopamine. *Electrochemistry Communications* **11**, 889-892 (2009).

29 Choo, S.-S., Kang, E.-S., Song, I., Lee, D., Choi, J.-W. & Kim, T.-H. Electrochemical Detection of Dopamine Using 3D Porous Graphene Oxide/Gold Nanoparticle Composites. *Sensors* **17**, 861 (2017).

30 Taylor, I. M., Robbins, E. M., Catt, K. A., Cody, P. A., Happe, C. L. & Cui, X. T. Enhanced dopamine detection sensitivity by PEDOT/graphene oxide coating on in vivo carbon fiber electrodes. *Biosensors and Bioelectronics* **89**, 400-410 (2017).

31 Li, J., Wang, Y., Sun, Y., Ding, C., Lin, Y., Sun, W. & Luo, C. A novel ionic liquid functionalized graphene oxide supported gold nanoparticle composite film for sensitive electrochemical detection of dopamine. *RSC Advances* **7**, 2315-2322 (2017).

32 Chauhan, N., Narang, J. & Jain, U. Highly sensitive and rapid detection of acetylcholine using an ITO plate modified with platinum-graphene nanoparticles. *Analyst* **140**, 1988-1994 (2015).

33 Qian, J., Yang, X., Jiang, L., Zhu, C., Mao, H. & Wang, K. Facile preparation of Fe3O4 nanospheres/reduced graphene oxide nanocomposites with high peroxidase-like activity for sensitive and selective colorimetric detection of acetylcholine. *Sensors and Actuators B: Chemical* **201**, 160-166 (2014).

34 Chauhan, N., Chawla, S., Pundir, C. & Jain, U. An electrochemical sensor for detection of neurotransmitter-acetylcholine using metal nanoparticles, 2D material and conducting polymer modified electrode. *Biosensors and Bioelectronics* **89**, 377-383 (2017).

35 Liu, T.-C., Chuang, M.-C., Chu, C.-Y., Huang, W.-C., Lai, H.-Y., Wang, C.-T., Chu, W.-L., Chen, S.-Y. & Chen, Y.-Y. Implantable graphene-based neural electrode interfaces for

electrophysiology and neurochemistry in in vivo hyperacute stroke model. *ACS applied materials & interfaces* **8**, 187-196 (2015).

36 Kang, T. W., Jeon, S.-J., Kim, H.-I., Park, J. H., Yim, D., Lee, H.-R., Ju, J.-M., Kim, M.-J. & Kim, J.-H. Optical detection of enzymatic activity and inhibitors on non-covalently functionalized fluorescent graphene oxide. *ACS nano* **10**, 5346-5353 (2016).

37 Yi, M., Yang, S., Peng, Z., Liu, C., Li, J., Zhong, W., Yang, R. & Tan, W. Two-photon graphene oxide/aptamer nanosensing conjugate for in vitro or in vivo molecular probing. *Analytical chemistry* **86**, 3548-3554 (2014).

38 Jeon, S.-J., Kwak, S.-Y., Yim, D., Ju, J.-M. & Kim, J.-H. Chemically-modulated photoluminescence of graphene oxide for selective detection of neurotransmitter by "turn-on" response. *Journal of the American Chemical Society* **136**, 10842-10845 (2014).

39 Thakur, V. K. & Thakur, M. K. *Chemical Functionalization of Carbon Nanomaterials: Chemistry and Applications*. 917-918 (Taylor & Francis, 2015).

40 Bendali, A., Hess, L. H., Seifert, M., Forster, V., Stephan, A. F., Garrido, J. A. & Picaud, S. Purified Neurons can Survive on Peptide-Free Graphene Layers. *Advanced healthcare materials* **2**, 929-933 (2013).

41 Sydlik, S. A., Jhunjhunwala, S., Webber, M. J., Anderson, D. G. & Langer, R. In vivo compatibility of graphene oxide with differing oxidation states. *ACS nano* **9**, 3866-3874 (2015).

42 Sahni, D., Jea, A., Mata, J. A., Marcano, D. C., Sivaganesan, A., Berlin, J. M., Tatsui, C. E., Sun, Z., Luerssen, T. G. & Meng, S. Biocompatibility of pristine graphene for neuronal interface. *Journal of Neurosurgery: Pediatrics* **11**, 575-583 (2013).

43 Park, S. Y., Park, J., Sim, S. H., Sung, M. G., Kim, K. S., Hong, B. H. & Hong, S. Enhanced differentiation of human neural stem cells into neurons on graphene. *Advanced Materials* **23**, H263-H267 (2011).

44 Fabbro, A., Scaini, D., León, V. n., Vázquez, E., Cellot, G., Privitera, G., Lombardi, L., Torrisi, F., Tomarchio, F. & Bonaccorso, F. Graphene-based interfaces do not alter target nerve cells. *ACS nano* **10**, 615-623 (2016).

45 Li, N., Zhang, Q., Gao, S., Song, Q., Huang, R., Wang, L., Liu, L., Dai, J., Tang, M. & Cheng, G. Three-dimensional graphene foam as a biocompatible and conductive scaffold for neural stem cells. *Scientific reports* **3**, 1604 (2013).

46 Martín, C., Merino, S., González-Domínguez, J. M., Rauti, R., Ballerini, L., Prato, M. & Vázquez, E. Graphene Improves the Biocompatibility of Polyacrylamide Hydrogels: 3D Polymeric Scaffolds for Neuronal Growth. *Scientific Reports* **7**, 10942 (2017).

47 Noh, M., Kim, S.-H., Kim, J., Lee, J.-R., Jeong, G.-J., Yoon, J.-K., Kang, S., Bhang, S. H., Yoon, H. H. & Lee, J.-C. Graphene oxide reinforced hydrogels for osteogenic differentiation of human adipose-derived stem cells. *RSC Advances* **7**, 20779-20788 (2017).

48 Hu, X.-B., Liu, Y.-L., Wang, W.-J., Zhang, H.-W., Qin, Y., Guo, S., Zhang, X.-W., Fu, L. & Huang, W.-H. Biomimetic graphene-based 3D scaffold for long-term cell culture and real-time electrochemical monitoring. *Analytical chemistry* **90**, 1136-1141 (2018).

49 Pashaie, R., Baumgartner, R., Richner, T. J., Brodnick, S. K., Azimipour, M., Eliceiri, K. W. & Williams, J. C. Closed-loop optogenetic brain interface. *IEEE Transactions on Biomedical Engineering* **62**, 2327-2337 (2015).

50 Chapman, C. A., Goshi, N. & Seker, E. Multifunctional Neural Interfaces for Closed-Loop Control of Neural Activity. *Advanced Functional Materials* (2017).

51 Krook-Magnuson, E., Gelinas, J. N., Soltesz, I. & Buzsáki, G. Neuroelectronics and biooptics: closed-loop technologies in neurological disorders. *JAMA neurology* **72**, 823-829 (2015).

52 Laxpati, N. G., Mahmoudi, B., Gutekunst, C.-A., Newman, J. P., Zeller-Townson, R. & Gross, R. E. Real-time in vivo optogenetic neuromodulation and multielectrode electrophysiologic recording with NeuroRighter. *Frontiers in neuroengineering* **7**, 40 (2014).

53 Grätzel, M. Photoelectrochemical cells. *nature* **414**, 338 (2001).

54 Graphene Flagship. *Biomedical Technologies*, <https://graphene-flagship.eu/project/divisions/Pages/biomedicalapplications.aspx> (2018).

55 Bressan, E., Ferroni, L., Gardin, C., Sbricoli, L., Gobbato, L., Ludovichetti, F. S., Tocco, I., Carraro, A., Piattelli, A. & Zavan, B. Graphene based scaffolds effects on stem cells commitment. *Journal of translational medicine* **12**, 296 (2014).

56 Menaa, F., Abdelghani, A. & Menaa, B. Graphene nanomaterials as biocompatible and conductive scaffolds for stem cells: impact for tissue engineering and regenerative medicine. *Journal of tissue engineering and regenerative medicine* **9**, 1321-1338 (2015).

Chapter 2. Deep 2-photon imaging and artifact-free optogenetics through transparent graphene microelectrode arrays

2.1 Abstract

Recent advances in optical technologies such as multi-photon microscopy and optogenetics have revolutionized our ability to record and manipulate neuronal activity. Combining optical techniques with electrical recordings is of critical importance to connect the large body of neuroscience knowledge obtained from animal models to human studies mainly relying on electrophysiological recordings of brain-scale activity. However, integration of optical modalities with electrical recordings is challenging due to generation of light-induced artifacts. Here, we report a transparent graphene microelectrode technology that eliminates light-induced artifacts to enable crosstalk-free integration of 2-photon microscopy, optogenetic stimulation and cortical recordings in the same *in vivo* experiment. We achieve fabrication of crack- and residue-free graphene electrode surfaces yielding high optical transmittance for 2-photon imaging down to ~1 mm below the cortical surface. Transparent graphene microelectrode technology offers a practical pathway to investigate neuronal activity over multiple spatial scales extending from single neurons to large neuronal populations.

2.2 Introduction

Multimodal integration of sensing and manipulation technologies allows comprehensive investigation of brain function across spatiotemporal scales [1]. Multi-photon imaging has enabled cellular-resolution imaging of neural populations in animal models while optogenetics has been widely employed for selective control of neural activity and casual manipulation of specific neural circuits. High temporal resolution of electrophysiological recordings is critical to complement

optical techniques for investigating fast dynamics of neural activity towards understanding functions of neural circuits. Furthermore, vast majority of early neuroscience research and clinical human studies rely on electrophysiological recordings of brain-scale activity. Combining optical techniques with electrical recordings can bridge the classical neuroscience knowledge obtained from animal models to human studies based on electrophysiological techniques. To that end, new tools allowing simultaneous measurements of multiple optical and electrical parameters are essential. Previous reports have shown proof-of-concept acquisition of local field potentials by graphene-based electrodes during simultaneous single-photon fluorescence imaging *in vitro* [2], or optogenetic (OG) photostimulation *in vivo* [3]. However, especially recordings during *in vivo* OG photostimulation have significantly suffered from light-induced artifacts, not showing any noticeable advantage over conventional platinum electrodes [3]. The problem of light-induced artifacts needs to be addressed since it constitutes a major obstacle particularly for the adaptation of transparent graphene electrode technology in chronic *in vivo* studies.

Light-induced artifacts generated by photovoltaic (Becquerel effect) and photothermal effects appear as transients or oscillations in recordings and can interfere with local field potential or spike recordings, depending on the frequency and duration of the light stimulus. The amplitudes of those artifacts are particularly higher for deep 2-photon imaging and optogenetic stimulation [4-7], due to increased laser power. Here, in the present manuscript we demonstrate that by careful design of key steps in the fabrication process for transparent graphene electrode, the light-induced artifact problem can be mitigated and virtually artifact-free LFP recordings can be achieved within operating light intensities. High optical transmittance of graphene supports simultaneous 2-photon imaging down to >1 mm directly beneath the transparent microelectrodes. For the first time, we show that transparent graphene electrodes can be employed for crosstalk-free integration of three

different modalities, 2-photon imaging, optogenetics and electrical recordings of cortical potentials at the same time in the same experiment. We combine local field potentials (LFPs) recordings from the cortical surface, with simultaneous (i) 2-photon imaging of neuronal and vascular structure down to ~1 mm below the cortical surface, (ii) 2-photon imaging of neuronal calcium activity, (iii) single-photon OG photoactivation, (iv) 2-photon imaging of arteriolar vasodilation, and (v) large-scale optical imaging of hemodynamic responses. Crosstalk-free integration of various *in vivo* optical imaging and stimulation methods with graphene electrode recordings proves that transparent graphene technology is a versatile platform applicable to numerous different experimental settings. In cases where depth-resolved electrical recordings are not required, optically transparent graphene technology allows seamless integration with depth-resolved optical imaging and stimulation circumventing the need for inserting invasive probes into brain tissue.

2.3 Results

2.3.1 Elimination of crack formation and organic residues

In order to produce transparent graphene microelectrode arrays with high yield, uniformity and artifact-free recording capability, we improved three critical steps in the fabrication process: (1) graphene transfer, (2) photoresist removal from the graphene surface, and (3) graphene surface cleaning from organic residues. We first optimized the process of graphene transfer from growth to target substrate. This process is the most critical, yet most sensitive step of the fabrication. Previously used techniques, such as wet transfer [3] and poly(methyl methacrylate) (PMMA) scaffold transfer [2] are prone to formation of cracks on the monolayer graphene sheets resulting in low yield for large-area planar arrays. In addition, copper etching used in these processes leaves residues impeding the process of PMMA removal [8]. As a result, the graphene layers may lose their structural integrity during annealing. Therefore, we adopted an alternative “bubbling transfer”

process [9] for crack-free transfer of graphene sheets onto the polymer substrate (see 2.5 Methods). To protect the graphene during photoresist stripping we used polymethylglutarimide (PMGI)-based bilayer lithography. Compared to other photoresists, PMGI leaves fewer residues on the graphene surface after resist removal. Photoresist removal is also critical to reduce crack formation in subsequent fabrication steps. To this end, we developed a four-step stripping/cleaning protocol for extensive cleaning of the graphene surface leading to a robust reduction of the average electrode impedance in the array (see 2.5 Methods and Figure 2.S1a, 2.S1b). These removal and cleaning steps are also crucial to achieve a residue- and contamination-free graphene surface, which is essential to minimize light absorption and generation of light-induced artifacts by graphene electrodes (Figure 2.S1c, 2.S1d).

We fabricated 4-by-4 arrays of 100 μm×100 μm square graphene electrodes separated by 300 μm (edge-to-edge) (Figure 2.1a). Fabrication steps for building transparent graphene arrays are shown in Figure 2.1b. The design included a gold array on the same substrate as the graphene arrays used as control sample. To fabricate transparent arrays, clear polyethylene terephthalate (PET, 50 μm thick) was chosen as substrate for its high optical transmittance (Figure 2.S2). To provide mechanical support during fabrication, the PET film was placed on a 4-inch silicon wafer covered with polymethylsiloxane (PDMS) as adhesive layer. Layers of 10 nm chromium and 100 nm gold were deposited onto PET film. Metal wires were patterned with photolithography and wet-etching. Graphene was then transferred onto the designed area with the bubbling transfer method (see 2.5 Methods). Graphene electrodes, wires and contact pads were patterned with photolithography and oxygen plasma etching and photoresist removal and cleaning of the graphene surface was performed as described in 2.5 Methods. Finally, the whole array was encapsulated by an 8-μm thick SU-8 layer with openings only at active electrode areas.

2.3.2 In vitro characterization of graphene microarrays

Following the fabrication, we characterized each graphene microelectrode array in 0.01 M phosphate-buffered saline (PBS) with electrochemical impedance spectroscopy (EIS) and cyclic voltammetry (CV) (Figure 2.1c-f). Figure 2.1e shows a uniform impedance distribution across 16 channels at 1 kHz as a representative sample. Our improved fabrication process results in a uniform impedance distribution and high yield; 95-100% of the channels have impedances less than 1.5 MΩ. Although high-impedance channels can still record neuronal activity, impedances <1.5 MΩ are desirable to minimize noise and obtain high signal-to-noise ratio (SNR) recordings (Figure 2.S3). CV measurements (Figure 2.1f) exhibit no redox peaks suggesting that the graphene/solution interface is capacitive. To test for sufficient flexibility of the graphene microelectrode array, we performed bending tests where the microarray was repeatedly bent to a radius of 5 mm without signs of device failure after 120 bending cycles (Figure 2.S4). A radius of 5 mm is within the same range as the natural curvature of mouse cortex.

To examine to which extent the presence of the graphene microarray affects the resolution of images acquired with 2-photon laser scanning microscopy, we placed microarray devices in a phantom sample above mounting medium containing 1-µm fluorescent polystyrene beads at a low concentration (Figure 2.S5). Compared to beads imaged beside the graphene microarray, a moderate (1.2-to-1.4-fold) increase in apparent bead size (FWHM within the imaging plane, i.e., across X and Y axis) and a 1.75-fold increase in apparent bead size along the Z axis size was observed for beads below microarray substrate and graphene electrode.

We investigated light-induced artifacts in graphene and gold electrodes *in vitro* using a standard optogenetics setup (fiber-coupled LED at 470 nm) (Figure 2.S6). Gold electrodes exhibit prominent light-induced artifacts during OG stimulation. Figure 2.S7a shows typical light-induced

artifacts recorded by gold electrodes for light intensities from 6.4 -54.1 mW mm^{-2} with a fixed illumination time of 20 ms. When the same experiment was repeated with transparent graphene electrodes, no measurable artifacts were detected (Figure 2.S7b). To further inspect the artifacts of gold and graphene electrodes in the frequency domain, repeated 20-ms light pulses were applied to the electrode site at 10 Hz and the power spectrum was plotted for both recordings (Figure 2.S7c, 2.S7d). For the gold electrode, we observed a 10-Hz peak corresponding to the artifact signals induced by light stimulation at this frequency. Besides the 10-Hz artifacts, some higher-order harmonic signals at 20, 30, and 40 Hz also existed in the recordings. For the graphene electrode, there were no detectable artifact components within the 0-60 Hz range. We performed an additional *in vitro* test with graphene microarrays using a 473-nm laser which illuminated the array through a 20× microscope objective (same setup as for in vivo experiments described in 2.5 Methods). The laser beam had a diameter of 230 µm (FWHM) and fully covers the area of one graphene electrode. For all tested light intensities up to 240.7 mW mm^{-2}, illumination of the substrate next to a graphene electrode does not elicit any detectable artifacts. When the laser illuminated a graphene electrode directly, artifacts were observed at light intensities higher than 60 mW mm^{-2} (Figure 2.S7e). These experiments suggest that transparent graphene electrodes can be safely used for *in vivo* OG stimulation and electrical recording experiments, ensuring crosstalk-free operation. After confirming artifact-free operation under *in vitro* conditions, we explored the capabilities of simultaneous optical imaging, OG stimulation, and electrical recordings through transparent graphene electrodes *in vivo* in the primary somatosensory cortex of anesthetized mice.

2.3.3 Deep in vivo 2-photon imaging through graphene arrays

To demonstrate deep 2-photon imaging through graphene electrodes *in vivo*, we placed the transparent array onto the exposed cortical surface, placed a glass coverslip on top, and sealed the

window (Figure 2.2a, 2.2b; see 2.5 Methods). We used 2-photon imaging in frame-scan mode to acquire image stacks, i.e., a series of images in the horizontal (XY) plane parallel to the cortical surface, with individual images spacing 3 μm along the depth (Z) axis. Figure 2.2c-f illustrates data from image stacks from the cortical surface down to 1200 μm in a GAD67-GFP transgenic mouse expressing enhanced green fluorescent protein (EGFP) in all inhibitory (GABAergic) cortical neurons [10]. EGFP was excited at its peak resonance of 905 nm and detected with a 490-560 nm bandpass filter (Figure 2.2c). Next, we injected a bolus of 2-MDa fluorescein-isothiocyanate (FITC)-dextran as intravascular tracer (see 2.5 Methods) and acquired an image stack while exciting at 950 nm (Figure 2.2d). This illumination wavelength excited both FITC and EGFP providing a compromise between efficiency of excitation (peak excitation of fluorescein is at 800 nm) and penetration of the excitation beam in tissue (950 nm penetrates better than 800 nm). FITC and EGFP have overlapping emission spectra and were detected in the same photomultiplier (PMT) channel.

To explore the possibility of deeper imaging through the graphene array, we injected an additional bolus of the intravascular tracer Alexa Fluor 680-dextran and switched the excitation to 1280 nm, which is the peak resonance of Alexa Fluor 680 [11]. This illumination wavelength lies within one of the spectral windows of opportunity, where combined effects of scattering and absorption are relatively low, and therefore allowing penetration of light through tissue. Alexa Fluor 680 was detected using a 954-nm shortpass filter. Under this regime, we could image down to 1200 μm below the cortical surface covered with the graphene array. Figure 2.2e, 2.2f show that our graphene electrodes provide virtually no obstacle for deep 2-photon imaging. That methodology can directly be applied to various research problems involving monitoring cortex-wide activation while probing the activity at deeper layers.

2.3.4 Simultaneous electrical recording and 2P Ca^{2+} imaging

We combined LFP measurements using the transparent graphene array with 2-photon calcium imaging of neuronal activity. We injected the calcium indicator Oregon Green BAPTA-1 (OGB1) into cortical layer II/III of the primary somatosensory cortex and applied Sulforhodamine 101 (SR101) to label astrocytes [12-14] before placing the graphene microelectrode array on the cortical surface and sealing the window (Figure 2.3A, 2.3b). To stimulate neuronal activity, we used a single electrical pulse (300 μs, 1 mA) delivered to the contralateral whisker pad. Fields-of-view (FOV) of ~50 μm×100 μm were imaged at ~10 Hz in frame-scan mode. Each FOV, including multiple neuronal cell bodies, was imaged continuously for ~250 s. During this time, we delivered 50 stimuli at an interval of 5 s. An example FOV is shown in Figure 2.3c; neuronal cell bodies (labeled n1-n7) are brighter than the surrounding neuropil; the FOV also contains a vessel (black) with adjacent astrocyte labeled both with OGB1 and SR101 (yellow). Stimulus-induced calcium increases were observed in neuronal cell bodies and neuropil for some of the stimulus trials (labeled by asterisks in Figure 2.3d; recordings of all six trials in Supplementary Movie 2.1). For the same "responsive" trials, a robust LFP response was detected by all working electrodes in the array (Figure 2.3e). In a more detailed analysis, we found that LFP responses have large amplitudes and are spatially broad in trials where Ca^{2+} responses are observed, while in trials without detectable Ca^{2+} response, LFP responses are comparatively weak and more localized (Figure 2.4a and Supplementary Movie 2.1). Furthermore, we found a positive correlation between LFP amplitude (from channels above the FOV or next to the FOV where calcium data was recorded) and Ca^{2+} signal amplitude (Figure 2.4b, 2.4c), which is consistent with previous reports in the literature [15]. Results obtained in another preparation are shown in Figure 2.S8. These experiments and additional data shown in Figure 2.S9 demonstrate that transparent graphene

electrodes are well suited for simultaneous *in vivo* 2-photon imaging providing sufficient transparency at the operating spectra and offering simultaneous 2-photon imaging and electrical recordings with no photovoltaic artifacts. Importantly, successful LFP recordings were obtained even with the graphene electrode directly above the imaging FOV (blue trace in Figure 2.3e); virtually artifact-free recording was achieved, as evident from the comparison of SNR for blue and black traces. This combined methodology can be used to investigate correlations between field potentials or cortical rhythms and dynamic cellular calcium responses.

2.3.5 Simultaneous electrical recordings, 2P imaging and optogenetics

Crosstalk-free integration of optical imaging, optogenetics and electrophysiological recordings is critical for investigating neural activity on a circuit or population level, while, at the same time, examining the causal role of individual neurons or groups of neurons in circuit function. We investigated the performance of graphene electrode arrays in studies involving both 2-photon imaging and single-photon OG photostimulation. To this end, we performed electrical recordings with graphene arrays and OG stimulation via a cylinder-shaped blue (473 nm) laser beam delivered through the microscope objective with ~210 μm in diameter (FWHM); this stimulation protocol has been used in a recent study from one of our laboratories [16]. Experiments were performed in Thy1-ChR2 transgenic mice expressing the optogenetic actuator channelrhodopsin-2 (ChR2) in layer V pyramidal neurons (Figure 2.5). We illuminated the cortical surface at one graphene electrode with 3 different laser powers (0.5, 1 and 2 mW) for 1, 5 and 10 ms. The LFP responses to OG stimulation scale with power and duration of the laser pulse (Figure 2.5a); the strongest response was recorded at the "targeted" electrode, and amplitudes decline with distance from the illumination target. To investigate artifacts resulting from direct illumination of the graphene electrode with the 473-nm laser, we tested two illumination geometries: overlapping with the

recording graphene electrode ("on graphene") versus in-between electrodes ("on substrate") (Figure 2.5b, 2.5c). We used four laser powers (0.5, 1, 2, and 7 mW) and illumination times of 1, 5, and 10 ms and performed the same OG stimulation protocol *in vivo*, post mortem, as well as with arrays placed on agar phantoms (blocks of 2% agar in ACSF). Virtually no artifact was observed at laser powers $\leq$2 mW or 50 mW mm^{-2} (Figure 2.5d; see Figure 2.S7e for in vitro results), while light-induced potentials were clearly visible upon illumination of the electrode but not the surrounding substrate with a laser power of 7.1 mW (or 210 mW mm^{-2}), which is considerably higher than the power typically used for OG photostimulation [16,17].

Next, we performed simultaneous LFP measurements and 2-photon imaging of arteriolar dilation induced by OG photostimulation in Thy1-ChR2 mice. Therefore, 2-MDa FITC-dextran was injected as intravascular tracer (Figure 2.6a) and line-scan imaging was used to follow changes in arteriolar diameter. Here, transitions between (dark) background and (bright, FITC-dextran-filled) intravascular lumen are used to estimate vessel diameters and their dynamic changes in response to OG stimulation (Figure 2.6b, 2.6c). Consistent with our previous reports, OG stimulation resulted in robust arteriolar dilation, mediated through messengers released by neurons in response to OG stimulation that are sensed by cells of the vasculature [16]. To exclude that vascular responses were elicited through tissue heating (see [18]), especially due to light absorption by the microarray, we applied the same OG stimulus in a ChR2-negative mouse and did not observe any stimulus-induced changes of arteriole diameters, which were measured close to the cortical surface (Figure 2.S10). Simultaneously obtained surface LFP recordings exhibited clear responses to the OG stimulus (Figure 2.6). To elicit detectable vascular responses, intensity and duration of the OG stimulus (illumination for 50-100 ms at 7 mW) were relatively high (and larger compared to stimuli in Figure 2.5a), so that the spatial distribution of measured LFP

responses became almost independent from the location of OG photostimulation (compare spatial LFP response profiles upon OG stimulation at site 1 and site 2 in Figure 2.6c). These data demonstrate for the first time (to the best of our knowledge) that transparent graphene electrode array technology can be successfully employed in combination with both 2-photon imaging and single-photon OG photostimulation without causing any crosstalk between three modalities.

2.3.6 Simultaneous electrical recordings and hemodynamic imaging

Comprehensive investigation of brain activity often requires bridging between measurements on different scales. Surface LFP recordings can provide such a bridge when combined with both micro- and mesoscopic optical measurements. To this end, we sought to demonstrate the utility of graphene devices for integration with camera-based mesoscopic imaging of intrinsic hemodynamic signals. We used spectral imaging of oxyhemoglobin (HbO), deoxyhemoglobin (Hb) and total hemoglobin (HbT) to detect stimulus-induced cortical hemodynamic activity (as a combination of changes in cerebral perfusion and oxygen metabolism) while imaging through a graphene surface array for simultaneous LFP recordings (Figure 2.7). For spectral imaging of hemoglobin oxygenation and its change in response to neuronal activation, light from a tungsten-halogen light source was filtered through a rotating filter wheel with individual filters ranging from 560 to 610 nm; illumination of the graphene array had no influence on LFP recordings (not shown). Six electrical 300-μs pulses delivered to the contralateral whisker pad over 2 s (at 3 Hz) induced neuronal activity and a hemodynamic response. The hemodynamic response measured below the graphene array (see overview in Figure 2.7a, 2.7b) is characterized by a rapid HbO increase 1 s after stimulus onset and a delayed decrease in HbR and takes about 20 s to return to baseline (Figure 2.7c); Figure 7f-h show the spatiotemporal dynamics of HbO, Hb, HbT changes. LFP responses to every of the 6 electrical stimuli are separated in time and show

different amplitudes in different channels, i.e. across space (Figure 2.7d; electrical recordings also in Supplementary Movie 2.3). The center of neuronal activity with largest LFP amplitudes (lower right corner of the array in Figure 2.7e) overlaps spatially with the initial (<2 s after stimulus onset) hemodynamic response (Figure 2.7f-h). Thus, this data shows that transparent graphene technology provides a versatile platform for combination with a suite of optical tools for imaging and manipulation of cortical activity across scales, ranging from monitoring of cellular activity with 2-photon microscopy to large-scale optical monitoring of hemodynamic response.

2.4 Discussion

Transparent graphene array technology provides a viable complementary alternative to needle arrays for multimodal measurements/manipulations within the penetration depth of multiphoton microscopy. In cases where depth-resolved electrical recordings are not required, optically transparent graphene surface arrays allow seamless integration with depth-resolved optical imaging modalities while circumventing the need to insert invasive probes into brain tissue. This technology is also well-suited for neurovascular and neurometabolic studies providing a "gold standard" neuronal correlate for optical measurements of vascular, hemodynamic, and metabolic activity.

Advancements in measurement technology play a critical role in neuroscience enabling scientific inquiry and powering discovery. This is also the goal of the ongoing BRAIN Initiative [19,20]. Several recent publications have demonstrated successful combination of electrode array recordings with OG photostimulation through integration of optical waveguides or incorporation of light emitting diodes (LEDs) along penetrating electrode shanks [21-26]. As a further step in this direction, ongoing efforts are focused on the addition of photodetectors along the electrode shanks that would provide optical imaging capability alongside with electrical recordings and OG

photoactivation [21]. This strategy is particularly attractive for deep brain studies targeting beyond the penetration limits of multiphoton microscopy [27,28]. Within these limits, however, simultaneous electrical recordings and optical imaging/manipulation can be achieved by engineering optically transparent electrode arrays [2,3,29-31]. To this end, in the present study, we introduced a new transparent graphene microelectrode array and demonstrated its unique capabilities for integration with 2-photon imaging and single-photon OG photostimulation.

In this study, transparent graphene array technology has been significantly advanced beyond previously reported transparent electrode demonstrations by incorporating a new graphene-friendly fabrication process. This new fabrication process avoids any crack formation in the transfer process proving 95-100% yield for the electrode arrays. Such techniques can as well be directly employed to fabricate high-density large area transparent arrays to monitor brain-scale cortical activity in large animal models. The fabrication process is also CMOS-compatible, so that graphene arrays can be directly integrated with amplifying and multiplexing circuits on the same chip [32].

With this technology, we demonstrate simultaneous mapping of surface LFP and high-resolution 2-photon imaging of neuronal calcium transients. LFP signals recorded from the cortical surface reflect flow of currents along the vertically aligned pyramidal cells' apical dendrites, largely produced by synaptic inputs. Therefore, these signals provide a measure of circuit activity [33,34]. Thus, combination of surface LFP recordings with 2-photon imaging of neuronal calcium would allow investigation of spiking activity in specific neurons (resolved with 2-photon imaging) in the context of circuit behavior, e.g., "up" and "down" states [35,36].

This combination of measurements is also of relevance for studies aiming to bridge neuronal activity across scales and, ultimately, connect the large body of classical neuroscience

knowledge, obtained from research in model systems (cell cultures, brain slices, *in vivo* mouse recordings, etc.), to human noninvasive electro-/magnetoencephalography (EEG/MEG) measurements [1]. Likewise, simultaneously acquired surface LFP and 2-photon measurements of single-vessel dilation as well as mesoscopic measurements of cortical hemodynamics would help neurovascular studies aiming towards the physiological underpinning of human noninvasive functional magnetic resonance imaging (fMRI) signals [37].

With rapid advancement in multiphoton microscopy and a growing arsenal of synthetic and genetically-encoded optical probes, we envision that recordings with optically transparent graphene electrode arrays will be combined with a wide range of microscopic physiological parameters related to neuronal activity [38,39], glial function [40], vascular dynamics [16,37], immune response [41], energy consumption [42], and more. With the current trends to move away from anesthesia and towards longitudinal imaging in awake behaving mice [43], incorporation of graphene surface arrays within a chronic cranial window implant [44] would facilitate the adoption of our technology. To this end, ongoing efforts in our laboratories are focused on engineering such double-duty implants providing a transparent optical window and capability of space-resolved surface LFP measurements. For multiphoton imaging, further improvement of image quality can be achieved by addition of adaptive optics to correct for distortions of the excitation wavefront due to mismatched refractive indices between graphene/PET substrate and cortical tissue [45].

Compatibility with large FOV imaging, exemplified in previous studies [2,3,31] by combination with CCD-based imaging of vascular/hemodynamic signals, can provide an intermediate step in bridging brain phenomena across scales. Scaled up to cover a larger cortical area, our technology may also be very informative for studies of large-scale, multi-area neuronal activity/connectivity [46] as well as for neuronal underpinning of large-scale spontaneous

hemodynamic oscillations and their correlation across different regions of the cerebral cortex [47]. As a nonmagnetic material, graphene array technology can also be utilized to develop fMRI-compatible implantable arrays.

To conclude, we envision that our transparent graphene-based electrode array technology will find application in multiple areas, advancing our understanding of how microscopic neuronal activity at the cellular scale translates into macroscopic activity of large neuronal populations and providing a neuronal correlate for optical measurement of vascular, hemodynamic, or metabolic activity.

2.5 Methods

2.5.1 Graphene transfer

The bubbling transfer method [9] was adopted to protect graphene from cracking during the process. Therefore, 300-nm thick 495 PMMA A4 was spin-coated on the graphene/copper bilayer structure. This PMMA/graphene/copper tri-layer was then connected to the cathode of a 20-V DC power supply, whereas the anode was submerged in 0.05 M NaOH in deionized water. As the tri-layer was gently and gradually immersed into the NaOH solution, hydrogen gas bubbles formed in-between the graphene and copper layer and exfoliated PMMA/graphene from the copper foil. The graphene layer needed to be thoroughly cleansed by floating on the surface of deionized water for three times before it was placed onto the gold pads on the flexible substrate.

2.5.2 Four-step cleaning procedure for photoresist removal

Graphene electrode impedance and susceptibility towards light-induced artifacts are highly dependent on photoresist residue. Therefore, we developed a 4-step stripping/cleaning protocol to remove organic residues from the graphene surface that was crucial to achieve arrays with low

impedance at high yield. After oxygen plasma etching, the sample was soaked in AZ 1-Methyl-2-pyrrolidon (NMP) and Remover PG to remove AZ1512 and PMGI, respectively. Another acetone bath was used to remove Remover PG residue. All three rinses were conducted at room temperature with gentle agitation. The last cleaning step included ten cycles of isopropanol/deionized water rinse.

2.5.4 Graphene microelectrode array fabrication

Using the new graphene transfer and photoresist removal methods, we developed the following fabrication process (see also Figure 2.1b). 50 μm thick clear PET (Mylar 48-02F-OC, elastic modulus: 4.9-5.1 GPa) is used as substrate for its high optical transmittance. To provide mechanical support during fabrication, 20-μm thick PDMS was spin-coated on a 4-inch silicon wafer, and PET film was placed on the PDMS adhesive layer. 10 nm chromium and 100 nm gold were deposited onto the PET film with a Denton Discovery 18 Sputter System. Metal wires were patterned with photolithography and wet-etching. Graphene was then transferred onto the designed area as described above. The device was dried completely at room temperature first and baked at 125 ˚C for 5 minutes to enhance bonding between graphene and PET substrate. The PMMA scaffold was removed in a room-temperature acetone bath for 20 minutes, following by ten cycles of isopropanol/deionized water rinse. Graphene contact pads were patterned with PMGI/AZ1512 bilayer photolithography and oxygen plasma etching (Plasma Etch PE100), followed by the 4-step cleaning method as described above. Finally, an 8-μm thick SU-8 2005 encapsulation layer with openings only at active electrode areas was patterned with photolithography, followed by 10 cycles of isopropanol/deionized water rinse to cleanse SU-8 residue.

2.5.5 Animal procedures

All experimental procedures were performed in accordance with the guidelines established by the UCSD Institutional Animal Care and Use Committee. We used 9 adult mice of either sex including 3 Thy1-ChR2-YFP (Jackson Stock Number 007612; heterozygous on a mixed C57Bl6/ICR background), 2 GAD67-GFP [10], and 6 wild type ICR mice. Surgical procedures in mice expressing channelrhodopsin-2 (ChR2) were performed in a dark room using a 515 nm longpass filter (Semrock) in the surgical microscope light source to avoid OG photostimulation during installation of the cortical window. Mice were anesthetized with isoflurane during surgical procedures (5% initially, 1-1.5% during all procedures). A catheter was inserted into the femoral artery. A metal holding bar was glued to the temporal bone for immobilization of the head during imaging. A ~4x4 mm cranial window was centered on the whisker area of primary somatosensory cortex (SI); overlying skull contralateral to the holding bar was exposed and dura mater removed.

In calcium imaging experiments, 50 μg calcium indicator Oregon Green 488 BAPTA-1 AM ester (OGB1; O-6807, Thermo Fisher) was first dissolved in 4 μl of 20% Pluronic F-127 in DMSO (P3000MP, Thermo Fisher); 80 μl of artificial cerebrospinal fluid (ACSF) were added to the OGB1 solution to yield a final concentration of 0.5 mM OGB1. OGB1 solution was pressure-microinjected into the cortical tissue [13] within the whisker area of the somatosensory cortex. Sulforhodamine 101 (SR101; S7635, Sigma) in ACSF was applied topically for ~2 min to label astrocytes [12] providing a contrast in tissue that was used for visual assessment of potential damage due to experimental procedures. Excess dye was washed away with ACSF.

The graphene array was placed on the cortical surface, a drop of 0.7% (w/v) agarose (A9793, Sigma) in ACSF was applied on top of the array, and the exposure was covered with a rectangular glass coverslip and sealed with dental acrylic. To avoid herniation of the exposed brain due to excessive intracranial pressure, the dura mater over the IVth cerebral ventricle was

punctured, thus allowing drainage of CSF. After the exposure was closed, the drainage hole was sealed with agarose.

After closing the exposure, mice were left to rest under 1% isoflurane for 45 min, which minimized leakage of drugs onto the exposed cortical tissue through cut dural blood vessels. Then, isoflurane was discontinued, and anesthesia was maintained with α-chloralose (50 mg/kg/h, C0128, Sigma or 100459, MP Biochemicals). Mice were paralyzed with pancuronium bromide (0.4 mg/kg/h, P1918, Sigma) [48] and ventilated (~110 min^{-1}) with 100% O_2. α-chloralose, pancuronium bromide, or 5% dextrose in saline were supplied through the femoral line every 30 min for the duration of data acquisition. Expired CO_2 was measured continuously using a micro-capnometer (Cl240, Columbus Instruments). Heart rate, blood pressure, and body temperature were monitored continuously. Blood gas was analyzed to cross-validate micro-capnometer measurements. Respiration was adjusted to achieve a $PaCO_2$ between 30 and 40 mmHg and pH between 7.35 and 7.45.

For vascular imaging experiments, 2-MDa dextran-conjugated Fluorescein isothiocyanate (FITC) (FD-2000S, Sigma) or 2-MDa dextran-conjugated Alexa Fluor 680 were injected through the femoral line (50-100 μl of 5% (w/v) solution in phosphate-buffered saline). To prepare 2-MDa Alexa Fluor 680-dextran, Alexa Fluor 680 NHS ester (A20008, Thermo-Fisher) was conjugated to 2-MDa amino dextran (AD2000x150, Finabio) using a custom conjugation protocol that can be found on the Devor lab academic website http://nil.ucsd.edu/ under “Resources”.

2.5.6 Two-photon imaging

Images were obtained using an Ultima 2-photon laser scanning microscopy system from Bruker Fluorescence Microscopy (formerly Prairie Technologies) equipped with an Ultra II

femtosecond Ti:Sapphire laser (Coherent) tuned to 905 nm for imaging of EGFP and 950 nm for imaging of FITC. For penetration deeper than ~600 μm, an optical parametric oscillator (Chameleon Compact OPO, Coherent) pumped by the same Ti:Sapphire laser was tuned to 1280 nm. The OPO was used in conjunction with intravascular administration Alexa Fluor 680-dextran [11]. FITC, EGFP, and Alexa Fluor 680 were imaged using cooled GaAsP photomultiplier tube (PMT) detectors (H7422P-40, Hamamatsu). SR101 was imaged using a multialkali PMT (R3896, Hamamatsu).

In experiments involving OG stimulation, the main dichroic mirror contained a 460-480 nm notch (Chroma ZT470/561/NIR TPC). An additional filter that blocks wavelengths in between 458-473 nm (Chroma ZET458-473/561/568/NIR M) was added in front of the PMT block. Nevertheless, residual bleed-through of the 473-nm light prevented us from using GaAsP PMT detectors. Therefore, in these experiments, FITC was imaged using a multialkali PMT. For imaging Alexa Fluor 680-dextran, custom-made filters (Chroma) were used; the main dichroic mirror contained a 440-480 nm notch and allowed light transmission from 780-1400 nm, the corresponding filter in front of the PMT blocks light between 440-480 nm and above 750 nm.

We used 4× (Olympus XLFluor4x/340, NA=0.28) or 5× (Zeiss Plan-NEOFLUAR, NA=0.16) objectives to obtain low-resolution images of the exposure. Olympus 20× (XLUMPlanFLNXW, NA=1.0 and UMPlanFI, NA=0.5) water-immersion objectives were used for high-resolution imaging. The laser beam diameter was adjusted to overfill the back aperture. Arteriolar diameter measurements were performed in a “free-hand” line-scan mode with a scan rate of 25-50 Hz. The scan resolution was 0.5 μm or less. Calcium imaging was performed in frame-scan mode at ~10 Hz per frame.

2.5.7 Sensory stimulation

Electrical stimulation was delivered to the whisker pad contralateral to the cortical exposure through a pair of thin needles inserted under the skin using 300-μs, 1-mA electrical pulses. For calcium imaging, 50 trials with 5 s interstimulus interval (ISI) were delivered at each measurement location. For mesoscopic imaging of cortical hemodynamics, a train of 6 electrical pulses (300 μs, 1 mA) were delivered at a rate of 3 Hz with an ISI of 30 s.

The stimulation device (A365 stimulus isolator, WPI) was triggered using a separate PC that also acquired timing signals for data acquisition ("trigger out" signals for each frame/line) and physiological readings using a National Instruments IO DAQ interface (PCI-6229) controlled by custom-written software in MATLAB (MathWorks Inc.). The timing of electrophysiological acquisition as well as each optical frame/line relative to the stimulus onset was determined during data analysis based on acquired triggering signals.

2.5.8 OG stimulation

In 2-photon experiments, OG stimulation was delivered though the objective using a 473-nm cylinder-shaped CW laser beam ~210 μm in diameter (FWHM) [16]. The beam was directed to defined locations in the sample using a dedicated set of galvanometer mirrors. The duration of the light pulse was controlled by a dedicated shutter and synchronized with imaging. Laser power was measured by directing the entire beam into the sensor of a broadband power meter (13PEM-001, Melles-Griot). The beam diameter was measured with a CCD-based laser beam profiler (LBP-2, Newport).

2.5.9 Recording and analysis of electrophysiological data

The electrophysiological data were recorded by the RHD2000 amplifier board and the RHD2000 evaluation system from Intan Technologies. The sampling rate was 10 kHz. The DC

offset was removed by the built-in filters of the system. Data were analyzed in MATLAB using custom-written software. After import and conversion into MATLAB files, trigger signals were detected, artifacts from electrical stimulation were removed by linear interpolation, if necessary, and the sampling rate was reduced to 1 kHz for trial average and further processing. For normalization, data recorded 50 ms before stimulus delivery were averaged and used as baseline value.

2.5.10 Analysis of imaging data

Data were analyzed in MATLAB using custom-written software as described in [16,37,40]. For analysis of calcium imaging data, neuronal cell bodies were segmented from composite red (SR101) and green (OGB1) images. For individual ROIs, the calcium signal per frame was calculated as average OGB1 fluorescence of all pixels within the ROI. This calculation was repeated for each frame in the time series to generate a single-ROI time-course. All pixels outside astrocytic and vascular ROIs and neuronal cell bodies were specified as neuropil. Vessel diameters were measured using continuous line scans across the vessel that form a space-time image when stacked sequentially. Diameters are extracted from profile changes resulting from expansion or contraction of the intravascular lumen, which is labeled with FITC- or Alexa Fluor 680-dextran.

2.5.11 Spectral imaging of blood oxygenation

Spectral imaging of blood oxygenation was performed as previously described in [49]. Briefly, six different bandpass filters were placed on a six-position filter wheel (Thorlabs), which was mounted on a DC motor. The center wavelength of the filters ranged from 560 to 610 nm with 10-nm intervals. Light from a tungsten-halogen light source (Oriel, Spectra-Physics) was directed through the filter wheel, which was coupled to a 12-mm fiber bundle. Images were acquired with

a cooled 16-bit CCD camera (Cascade 512B, Photometrics). Image acquisition was triggered at ~18 Hz by individual filters in the filter wheel passing through an optic sensor. The image set at each wavelength was averaged across trials and averaged data was converted to changes in HbO and Hb at each pixel using the modified Beer Lambert relationship as detailed in ref. [49]. Baseline concentrations of 60 μM and 40 μM were assumed for HbO and Hb, respectively [50,51].

2.5.12 Two-photon imaging of fluorescent polystyrene beads

The graphene microarray device was fixed at its connecting wire to a 22×22 mm glass coverslip with UV-curable optical adhesive (Norland 61). Four 3-mm coverslips serving as spacers were fixed at each corner of the coverslip. 1-mm fluorescent polystyrene beads (Fluoresbrite YG Microspheres, Polysciences, 18860) were diluted to a final dilution of 1:10,000 in ProLong Gold mounting medium (Thermo Fisher, refractive index: 1.47 after curing). A drop of bead-containing mounting medium was added onto a glass slide and the coverslip with array was placed on top. Two-photon imaging was performed after curing of the mounting medium at an excitation wavelength of 800 nm using a 20× UMPlanFI (NA=0.5) water-immersion objective. Data was analyzed in ImageJ using the MetroloJ plugin [52].

2.5.13 Statistics

Improved array performance in vitro has been shown in 4 independent manufacturing processes with 3 arrays in each batch.

Animal experiments were designed as proof-of-principle experiments to demonstrate graphene microarray performance in vivo; statistical comparison of experimental groups is therefore not applicable. Structural imaging in GAD67-GFP was performed in two independent experiments; calcium imaging with OGB was performed in four independent experiments;

experiments involving OG stimulation were performed in three Thy1-ChR2 animals and one wild-type animal; macroscopic hemodynamic imaging was performed in one animal.

2.5 Acknowledgements

We would like to acknowledge Office of Naval Research Young Investigator Award (N00014161253), National Science Foundation (ECCS-1752241, ECCS-1734940), NIH (U01NS094232, MH111359, NS057198 and S10RR029050), the Research Council of Norway (#223273, #226971), San Diego Frontiers of Innovation Scholars Program, and Kavli Institute for Brain and Mind Innovative Research for funding this research. This work was performed in part at the San Diego Nanotechnology Infrastructure (SDNI) of UCSD, a member of the National Nanotechnology Coordinated Infrastructure, which is supported by the National Science Foundation (Grant ECCS-1542148). M. Thunemann was supported by postdoctoral fellowship from the German Research Foundation (DFG TH 2031/1).

Chapter 2 is a reprint of M. Thunemann, Y. Lu, X. Liu, K. Kılıç, M. Desjardins, M. Vandenberghe, S. Sadegh, P. A. Saisan, Q. Cheng, K. L. Weldy, H. Lyu, S. Djurovic, O. A. Andreassen, A. M. Dale, A. Devor, D. Kuzum, Deep 2-photon imaging and artifact-free optogenetics through transparent graphene microelectrode arrays, Nature Communications 9 (1), 2035 (2018). The dissertation author was the co-first author of this article.

2.6 Figures

Figure 2. 1 Graphene microelectrode array fabrication and electrochemical characterization.

(a) Design of the graphene microelectrode array. Each electrode is a 100 μm×100 μm square and the spacing in-between two adjacent electrodes is 300 μm (edge-to-edge). Scale bar, 500 μm. (b) Fabrication of graphene microelectrode arrays. Step 1: clear 50-μm thick PET film. Step 2: 10 nm Cr and 100 nm Au sputtered onto the PET film. Step 3: metal wires patterned with photolithography and wet-etching. Step 4: graphene transfer with bubbling method. Step 5: graphene contact pads patterned with photolithography and oxygen plasma-etching. Step 6: Spin-coating of SU-8 and patterning of openings with lithography. (c)-(d). Electrochemical impedance spectroscopy of all 16 channels on an array. (e) Impedance at 1 kHz; channels have an average impedance of 963 kΩ. (f) Cyclic voltammetry of a representative channel shows no redox peaks.

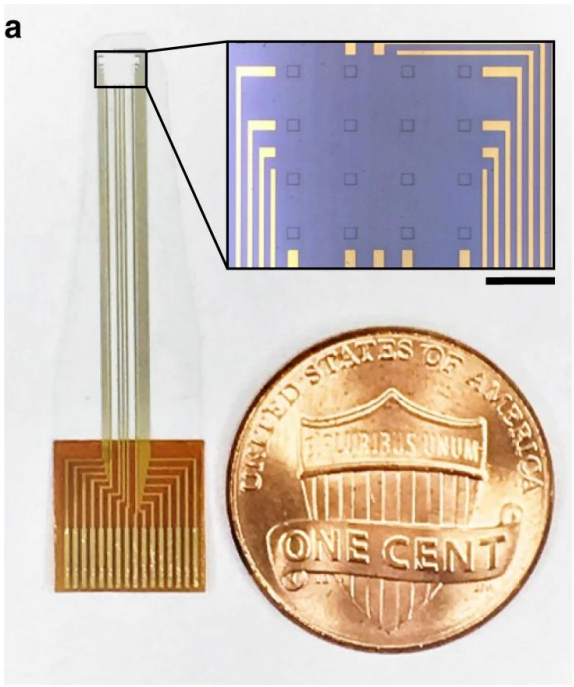
a
UNITED STATES OF AMERICA
E PLURIBUS UNUM
ONE CENT

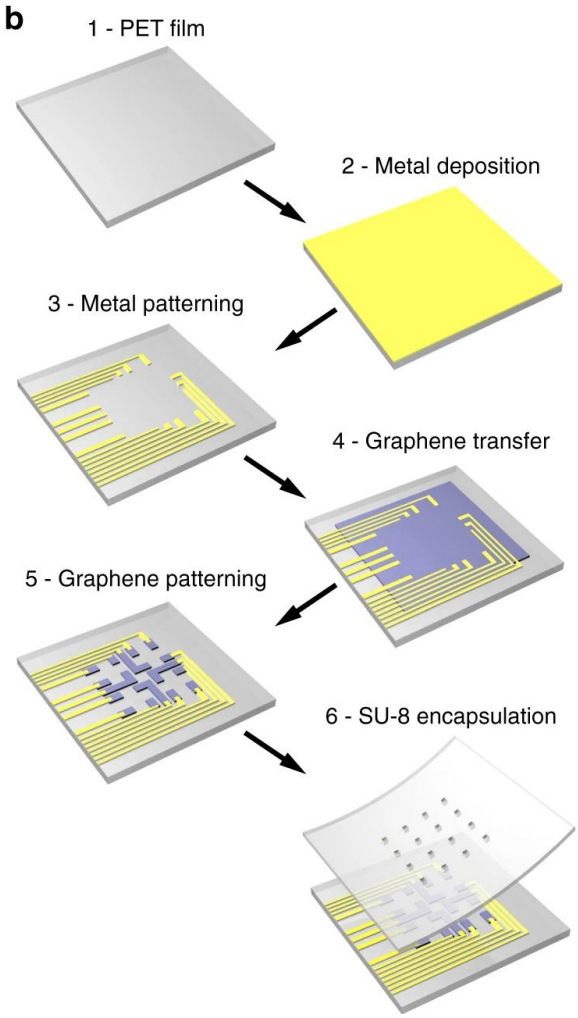
b
1 - PET film
2 - Metal deposition
3 - Metal patterning
4 - Graphene transfer
5 - Graphene patterning
6 - SU-8 encapsulation

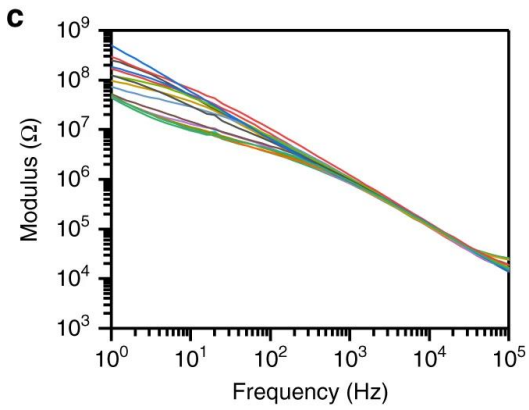
c
Modulus (Ω)
Frequency (Hz)

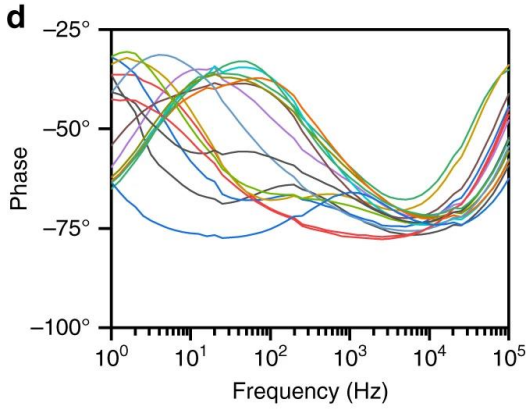
d
Phase
Frequency (Hz)

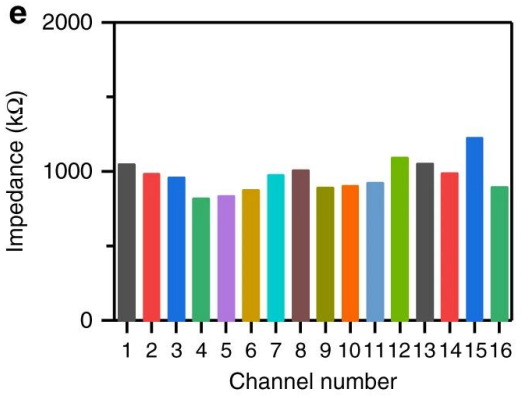
e
Impedance (kΩ)
Channel number

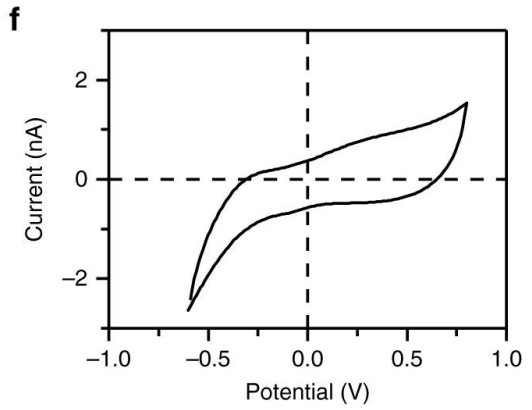
f
Current (nA)
Potential (V)

Figure 2. 2 Structural 2-photon imaging through a graphene microelectrode array.

(a) After placement of head-post (not shown), craniotomy and dura removal, the graphene microelectrode array is placed on the surface of the primary somatosensory cortex (SI). The exposure is covered with agarose and closed with a coverslip. Dental acrylic is used to fix the coverslip and the arrays' connecting wires to reduce motion. (b) Bright-field image of an exposure with graphene microelectrode array. Graphene electrodes and wires in the center of the array are not visible, but the gold wires for connection to the amplifier board. Scale bar, 500 µm. (c) Detection of EGFP-expressing interneurons in GAD67-GFP mice below a single graphene electrode (yellow outline). Images were acquired using 2-photon excitation at 905 nm (laser power from 3 mW at the surface to 57 mW at 600 µm cortical depth). (d) The same region as in panel c is shown, but after intravascular injection of FITC-dextran (2 MDa); images were acquired using 2-photon excitation at 950 nm (laser power from 8 mW at the surface to 77 mW at 600 µm cortical depth). (e) The same region as in panel c, d is shown, but after additional intravascular injection of Alexa Fluor 680-dextran (2 MDa); images were acquired using 2-photon excitation at 1280 nm (laser power from 2 mW at the surface to 44 mW at 1200 µm cortical depth). Panels c-e show maximum intensity projections (MIPs) of images acquired at different depths (step size: 3 µm) below the cortical surface (MIP range is indicated above individual images). Scale bar for c-e, 100 µm. (f) Orthogonal (XZ) MIP of the Alexa Fluor 680-dextran dataset shown in panel E; graphene microelectrode array (A) and cortical surface (S) are on the top of the image. Scale bar, 100 µm.

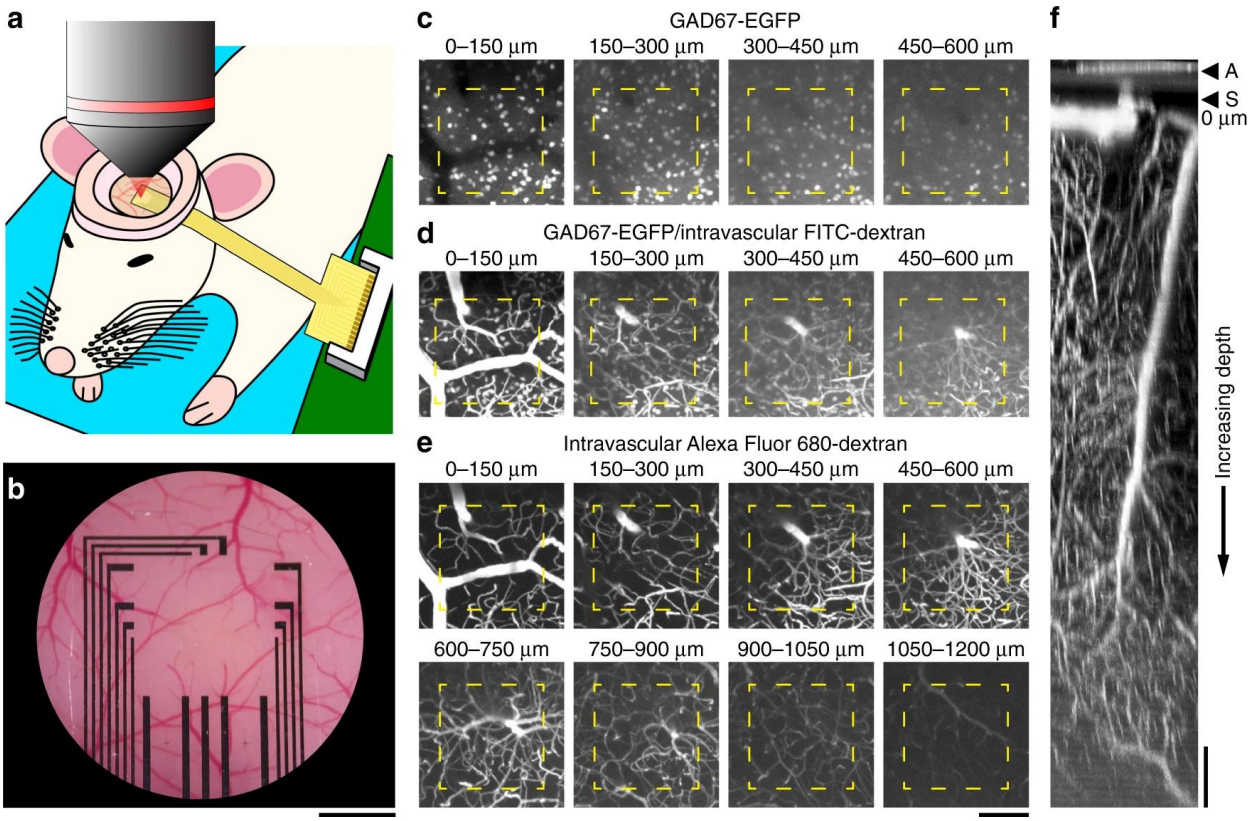
a
b
c
GAD67-EGFP
0–150 µm
150–300 µm
300–450 µm
450–600 µm
d
GAD67-EGFP/intravascular FITC-dextran
0–150 µm
150–300 µm
300–450 µm
450–600 µm
e
Intravascular Alexa Fluor 680-dextran
0–150 µm
150–300 µm
300–450 µm
450–600 µm
600–750 µm
750–900 µm
900–1050 µm
1050–1200 µm
f
A
S
0 µm
Increasing depth

Figure 2. 3 Combination of 2-photon-based calcium imaging with electrical recordings.

Before placement of the graphene microelectrode array, the calcium indicator Oregon Green 488 BAPTA-1 (OGB1) AM ester was pressure-microinjected and astrocytes were stained with Sulforhodamine 101 (SR101). Scale bar, 500 µm. (a) Overview image of OGB1 (green) and SR101 (red) staining below the graphene microelectrode array. Yellow outlines indicate single graphene electrodes, white rectangles indicate imaging sites shown in panel b and c. Scale bar, 100 µm. (b) 2-photon imaging of OGB1 (green) and SR101 (red) below a single graphene electrode (yellow outline). Maximum intensity projections (MIPs) of images acquired at different depths (step size: 3 µm) below the cortical surface are shown (MIP range indicated above individual images). Scale bar, 100 µm. (c) Image of the region (size: 140 µm × 32.6 µm) used for functional Ca^{2+} imaging as shown in panel d. In the center, a vessel (dark) passes the imaging plane. For analysis, images were segmented into individual neurons (n1-n7; bright OGB1, no SR101 staining), astrocytes (bright OGB1 and SR101 staining), and neuropil (OGB1 staining, no SR101 staining). (d) Calcium traces (OGB1 fluorescence change relative to pre-stimulus baseline, ΔF/F) of individual neurons (n1-n7 as shown in panel c) and neuropil (np). Single electric stimuli (300 µs, 1 mA) were delivered every 5 s (red arrows) to the whisker pad. Imaging was performed 150 µm below the cortical surface at 12 Hz with 2-photon excitation at 800 nm and a power of 50 mW. Asterisks (*) indicate "responsive" trials. (e) Corresponding electrical responses to electrical whisker pad stimulation (red arrow) measured with graphene microelectrode array; traces from 4 individual trials matching stimulations no. 1, 2, 3, 6 in panel d are shown. Graphene electrodes are numbered 1 (top left in panel a) to 16 (lower right in panel a); electrode 3 is non-functional and 2-photon Ca^{2+} imaging was performed right below electrode 15 (highlighted in blue) leading to slightly increased noise in this channel. Artifacts resulting from electrical stimulation were removed by linear interpolation.

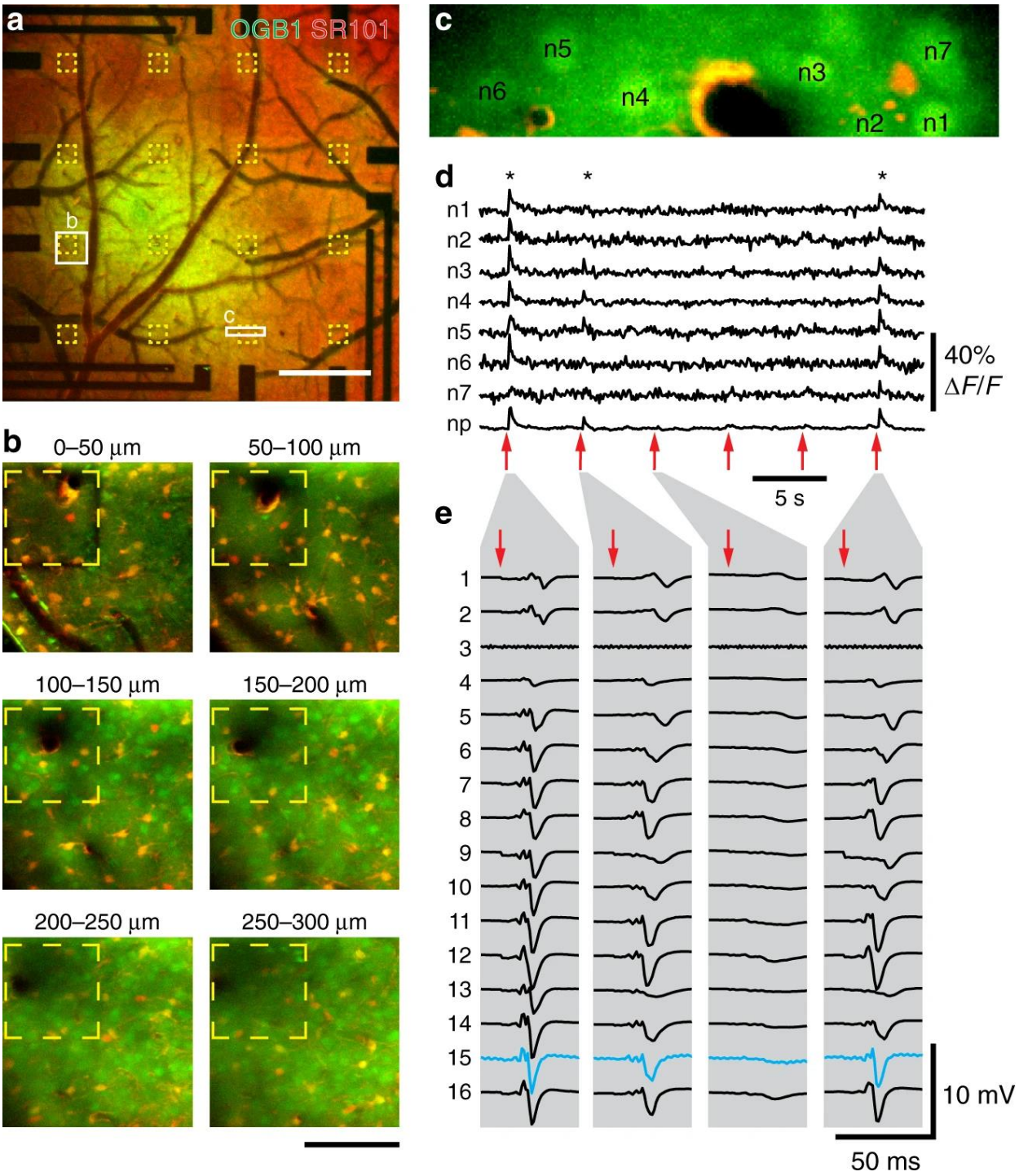
a
OGB1 SR101
b
c
b
0–50 µm
50–100 µm
100–150 µm
150–200 µm
200–250 µm
250–300 µm
c
n5
n7
n3
n6
n4
n2
n1
d
*
*
*
n1
n2
n3
n4
n5
n6
n7
np
40%
ΔF/F
5 s
e
1
2
3
4
5
6
7
8
9
10
11
12
13
14
15
16
10 mV
50 ms

Figure 2. 4 Relationship between local field potential (LFP) and Ca^{2+} transients

(a) Comparison of LFP amplitudes across the array in trials where Ca^{2+} transients were observed (left; 10 trials) or not observed (right; 13 trials, only trials with LFP response amplitudes <−500 µV are included); amplitudes (heatmap) and traces are trial averages; channel 15 (where Ca^{2+} data was acquired) is highlighted. Data from experiment shown in Figure 3c-e. (b), (c) Correlation between LFP and Ca^{2+} peak amplitude per trial; trials with LFP responses <−400 µV are included. Calcium signal amplitudes are derived from two different animals; representative experimental data for panel b (37 trials included) is shown in Figure 2.3, representative data for panel c (100 trials included) is shown in Figure 2.S8.

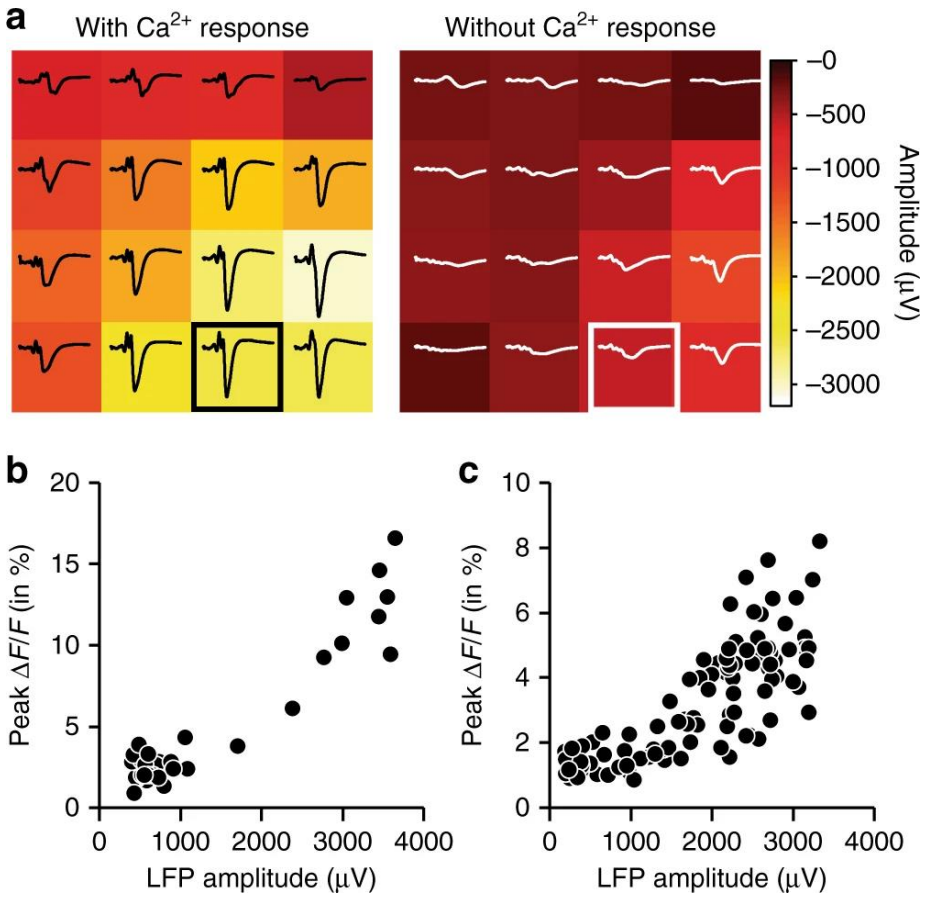
a
With Ca2+ response
Without Ca2+ response
–0
–500
–1000
–1500
–2000
–2500
–3000
Amplitude (µV)
b
Peak ΔF/F (in %)
LFP amplitude (µV)
c
Peak ΔF/F (in %)
LFP amplitude (µV)

Figure 2. 5 Measurement of optogenetic photostimulation-induced electrical potentials in Thy1-ChR2 mice that express channelrhodopsin-2 (ChR2) in layer-V pyramidal neurons.

(a) A 473-nm laser beam (diameter: 210 µm full-width-half-maximum) was sent through a 20× objective next to one graphene electrode (highlighted in grey). Different illumination times (1, 5 and 10 ms) and powers (0.5, 1 and 2 mW) were used. Heatmaps represent maximal response amplitude of the 16 electrodes in the array; example traces are shown for 0.5 mW/1 ms (top left) and 2 mW/10 ms (bottom right). (b) Two-photon image of the illumination target after intravascular injection of FITC-dextran (2 MDa); the yellow outline indicates the position of the graphene electrode. Scale bar, 100 µm. (c) Per condition, illumination with the 473-nm laser beam was targeted to 12 sites 'on substrate' (circles with broken lines) and to 4 sites 'on graphene' (circles with closed lines) where the laser beam directly irradiates part of the electrode (yellow outline). (d) Electrical response of the single graphene electrode within the illumination target in a live Thy1-ChR2 mouse ('Thy1-ChR2'), in the same animal after death ('post mortem'), and in vitro on an agarose phantom ('on phantom'). Laser pulses of 1, 5 and 10 ms length with powers of (0.5, 1, 2, and 7 mW) were used. Average responses of 12 'on substrate' or 4 'on graphene' illuminations per condition are shown; averaged responses from 'on substrate' illuminations were used for response amplitude comparison across the microelectrode array as shown in panel a.

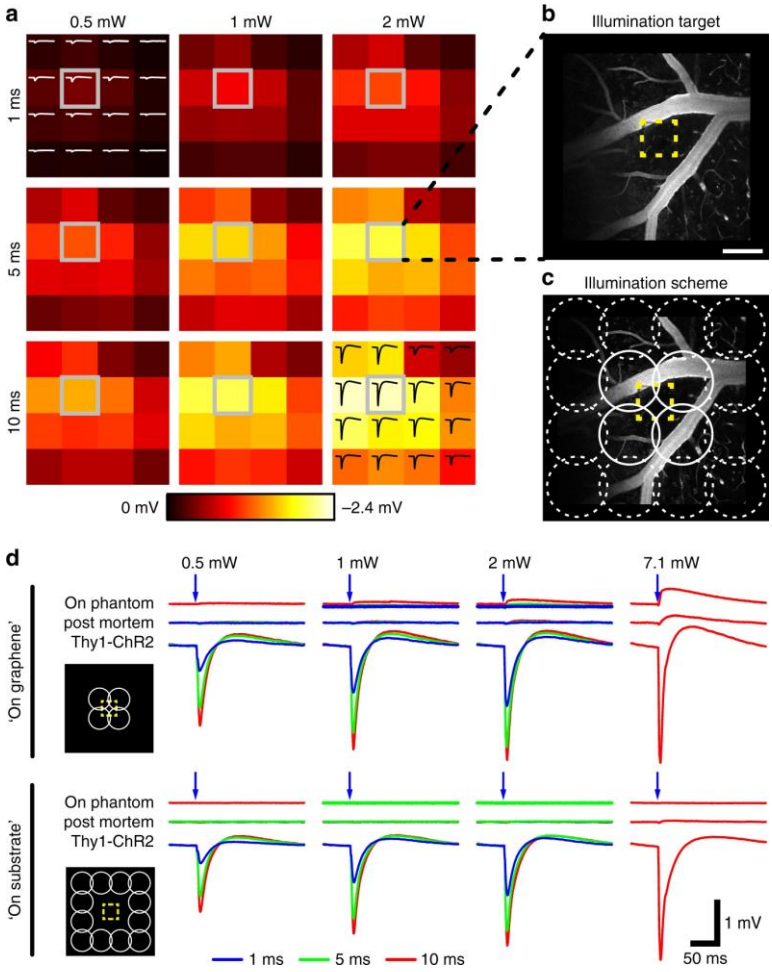
a
0.5 mW
1 mW
2 mW
1 ms
5 ms
10 ms
0 mV
–2.4 mV
b
Illumination target
c
Illumination scheme
d
0.5 mW
1 mW
2 mW
7.1 mW
'On graphene'
On phantom
post mortem
Thy1-ChR2
'On substrate'
On phantom
post mortem
Thy1-ChR2
1 mV
50 ms
1 ms
5 ms
10 ms

Figure 2. 6 Measurement of vascular responses to optogenetic (OG) photostimulation below graphene microelectrode arrays in Thy1-ChR2 mice.

(a) Location of diving arterioles for diameter measurements with 2-photon imaging as shown in panels b, c. Yellow outlines indicate single graphene electrodes. Data was acquired after intravascular injection of FITC-dextran (2 MDa). Scale bar, 500 μm. (b) Line-scan mode was used to measure time courses of single arteriole diameters; blue arrows indicate when a 473-nm laser stimulus was delivered, red lines indicate computed vessel borders used for estimation of diameter changes. (c) High-magnification scans of arteriole segments are shown on the left (scale bars: 50 μm); red arrows indicate line scan location. Vascular responses (diameter change relative to pre-stimulus baseline, Δd/d) averaged from 5-6 photostimulation events (indicated by blue arrow) are shown in the middle; respective electrical responses to photostimulation measured with the graphene array are shown on the right. Note that stimulus intensities and illumination times used to elicit detectable vascular responses (50-100 ms at 7 mW) are larger than photostimulation shown in Figure 2.5. Control experiment with a ChR2-negative animal is shown in Supplementary Figure 2. S10.

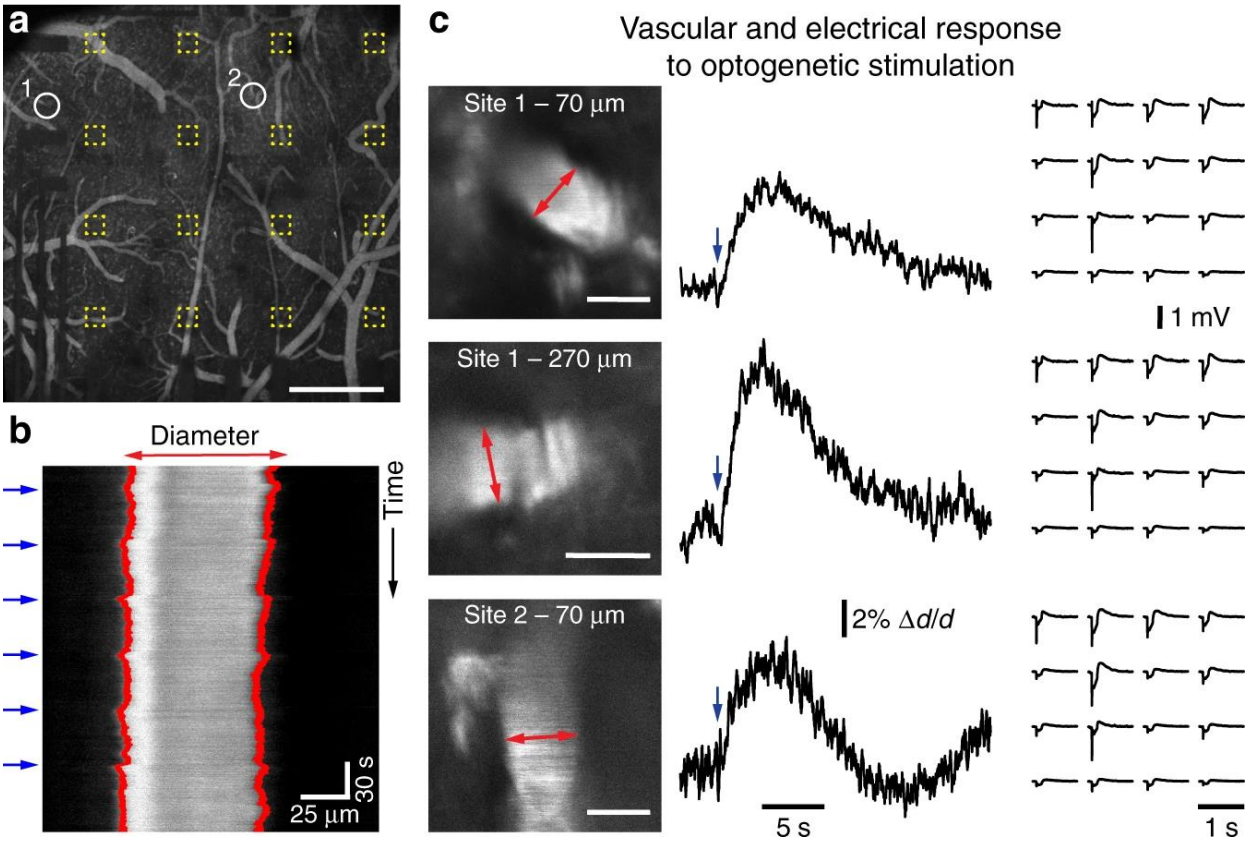
a
1
2
b
Diameter
Time
30 s
25 µm
c
Vascular and electrical response
to optogenetic stimulation
Site 1 – 70 µm
Site 1 – 270 µm
Site 2 – 70 µm
1 mV
2% Δd/d
5 s
1 s

Figure 2. 7 Combination of macroscopic hemodynamic optical imaging with electrical recordings.

Light absorption at six wavelength ranges (560-610 nm, 10 nm step size) was recorded with a CCD camera at an acquisition frequency of ca. 18 Hz. Absorption at these wavelengths was converted to concentrations of oxyhemoglobin (HbO), deoxyhemoglobin (HbR), and total hemoglobin (HbT) measured as changes relative to pre-stimulus baseline. A train of six electric pulses (1 mV for 2 s at 3 Hz, pulse width: 300 µs) was delivered to the whisker pad. (a) Image of the exposure and graphene microelectrode array with region of interest (yellow line) used for evaluation of hemodynamic signals. (b) Image of the exposure with location and numbering of graphene electrodes. Scale bars for A and B, 500 µm. (c) Changes in HbO, HbR, and HbT in response to electrical whisker pad stimulation (average of 10 trials across the region of interest shown in panel a). (d) Corresponding recordings from the graphene microelectrode array; voltage traces recorded during stimulation period are shown (average of 10 trials; channel positions as indicated in panel b). (e) Spatiotemporal analysis of the electrical response to one electrical stimulus (red highlight in panel d). The sequence of 24 images covers a recording period of 42 ms (time between two images: 2 ms); the yellow rectangle indicates stimulus delivery. (f)-(h) Spatiotemporal analysis of changes in HbO, HbR, HbT in response to whisker pad stimulation. The sequence of 24 images covers a recording period of 8.4 s (time between two images: 400 ms); red rectangles indicate stimulation onset.

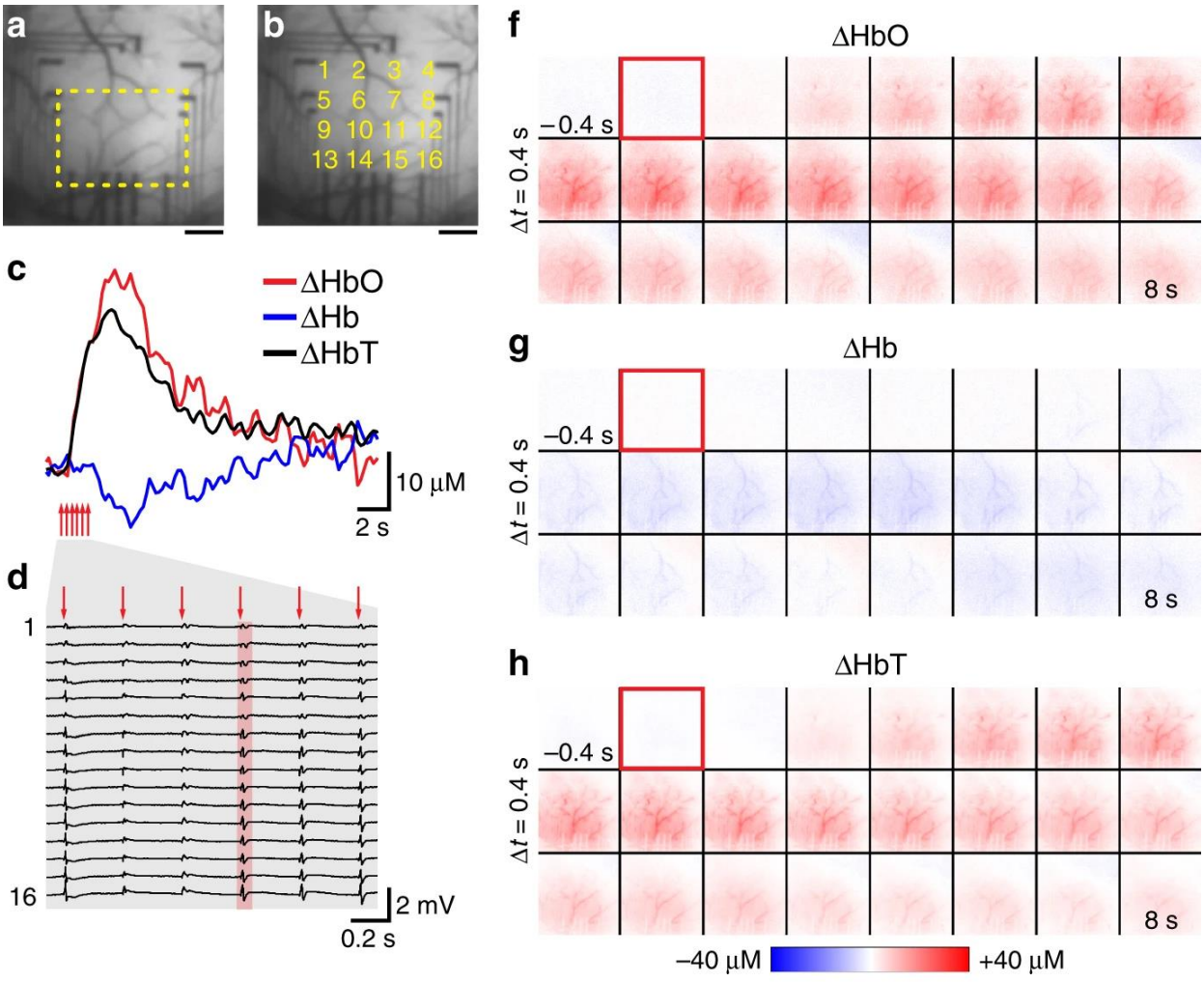
a
b
1 2 3 4
5 6 7 8
9 10 11 12
13 14 15 16
c
ΔHbO
ΔHb
ΔHbT
10 μM
2 s
d
1
16
2 mV
0.2 s
f
ΔHbO
−0.4 s
Δt = 0.4 s
8 s
g
ΔHb
−0.4 s
Δt = 0.4 s
8 s
h
ΔHbT
−0.4 s
Δt = 0.4 s
8 s
−40 μM
+40 μM
e
−2 ms
Δt = 2 ms
40 ms
−650 μV
+650 μV

2.7 Supplementary Informtion

Figure 2. S1 The 4-step cleaning method (4SCM) reduces impedance and light-induced artifacts.

(a) The 4SCM decreases average impedance (average from 16 channels on one array) from 4.03 MΩ to 963 kΩ. Error bars represent standard deviation of 16 channels from 3 arrays on one wafer. (b) Electrochemical impedance spectroscopy of one representative channel from an array cleaned with the 4SCM and from one graphene electrode where 4SCM was not applied. (c) Scanning electron microscopy image of a graphene electrode without 4SCM applied. Residue covers a large portion of the surface of the graphene electrode; white arrows indicate large pieces of residue, the white dashed line indicates the boundary between residue-covered graphene (left, lighter) and clean graphene (right, darker). Scale bar, 20 μm. (d) Illumination-induced artifacts (10-ms light pulses from a fiber-coupled 470-nm LED at 10 Hz, see also Supplementary Figures 6 and 7) are readily visible when a high-impedance graphene electrode (blue curve, 6.71 MΩ) is illuminated, while no observable light-induced artifacts were recorded upon illumination of a low-impedance graphene electrode (red curve, 0.88 MΩ) on the same array.

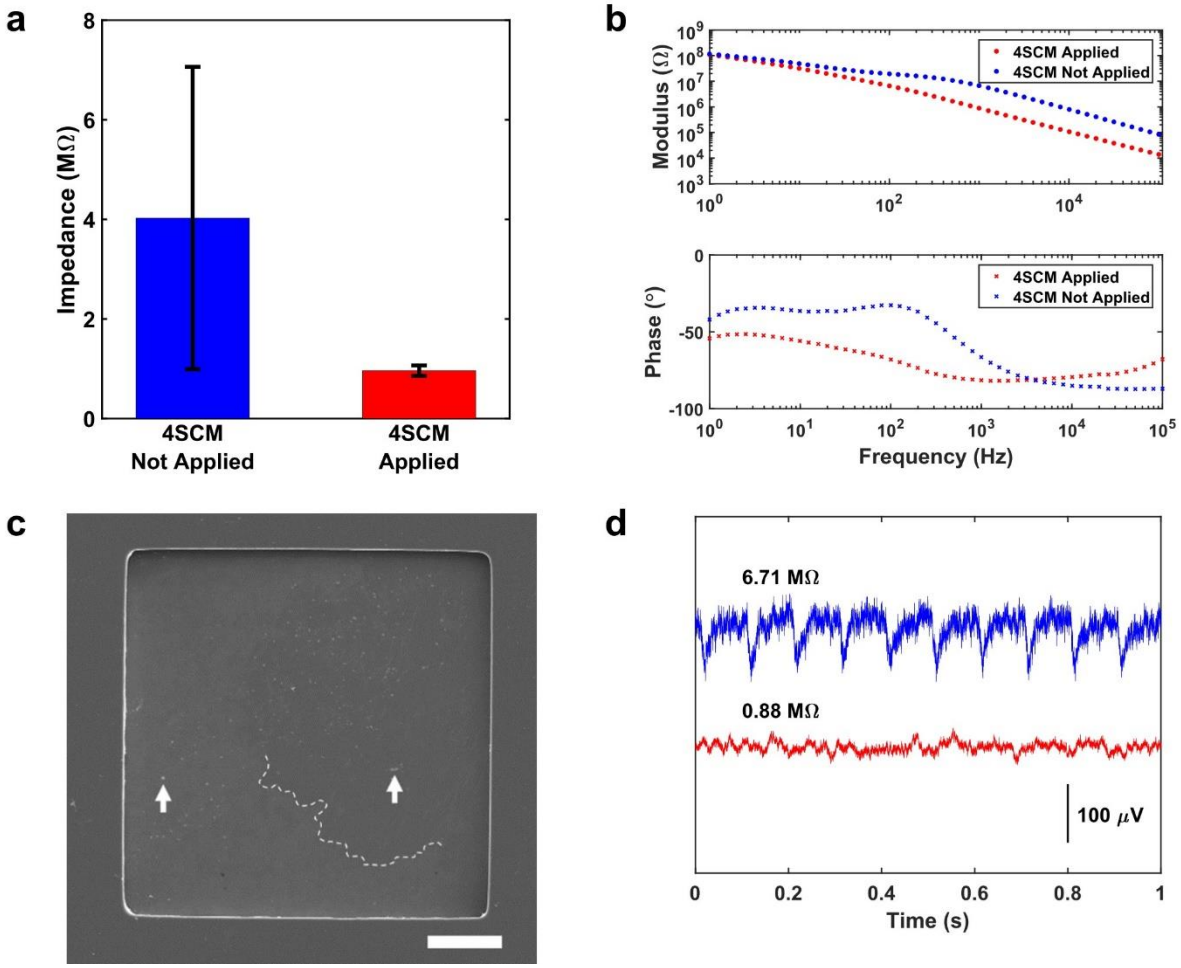
a
Impedance (MΩ)
8
6
4
2
0
4SCM
Not Applied
4SCM
Applied
b
Modulus (Ω)
4SCM Applied
4SCM Not Applied
Phase (°)
0
-50
-100
Frequency (Hz)
c
d
6.71 MΩ
0.88 MΩ
100 μV
Time (s)

Figure 2. S2 Transmission spectrum of graphene on polyethylene terephthalate (PET) compared to 10 nm Cr on PET or Kapton.

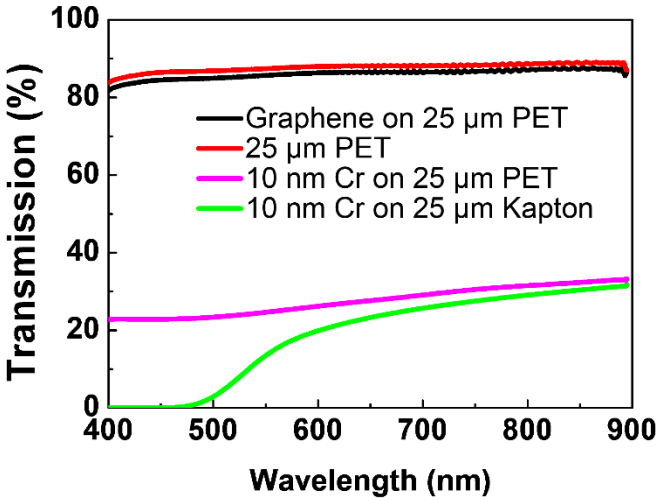
Transmission (%)
Wavelength (nm)
Graphene on 25 μm PET
25 μm PET
10 nm Cr on 25 μm PET
10 nm Cr on 25 μm Kapton
100
80
60
40
20
0
400
500
600
700
800
900

Figure 2. S3 Relationship between electrode impedance and noise levels.

(a) Noise levels were estimated for all electrode channels from 16 recording sessions, i.e. 16 data points for each impedance. The root mean square (rms) values of the noise were calculated from high-pass filtered (2 Hz) neural recordings. (b) Noise level for high-impedance channels (>1.5 MΩ) is significantly higher than for low-impedance channels (<1.5 MΩ). Error bars represent standard error of the mean; *** indicate $p=5.9\times10^{-20}$ (rank sum test in MATLAB).

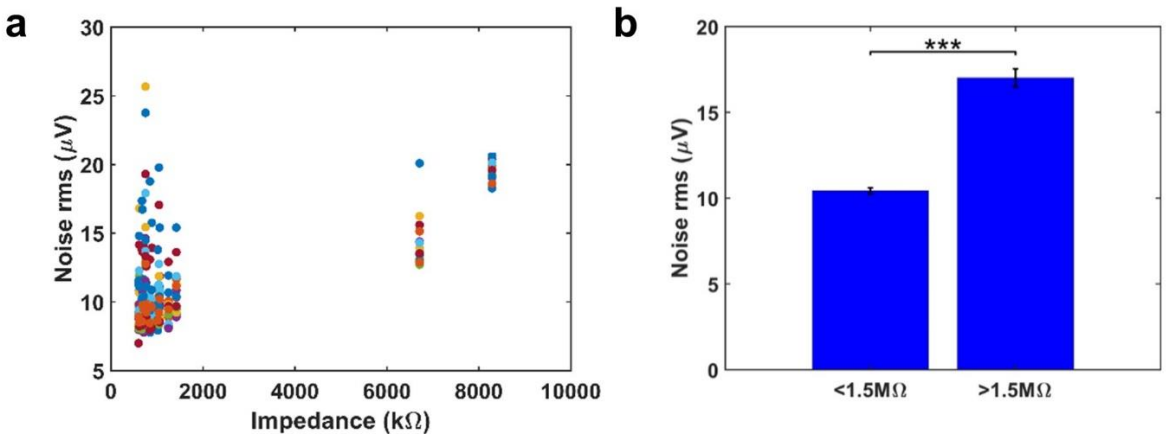
a
Noise rms (μV)
Impedance (kΩ)
b
Noise rms (μV)
***
<1.5MΩ
>1.5MΩ

Figure 2. S4 Bending test of the graphene microelectrode array.

(a) The array is wrapped around a test tube (radius: 5 mm) to demonstrate the flexibility of the array. (b) Impedance at 1 kHz remains stable for at least 120 bending cycles (mean ± standard deviation of 3 measured channels in the same array are shown). During one cycle, the array is bent manually to a radius of 5 mm around the test tube (as shown in panel A) and released. Impedance measurements were performed after 20 consecutive bending cycles.

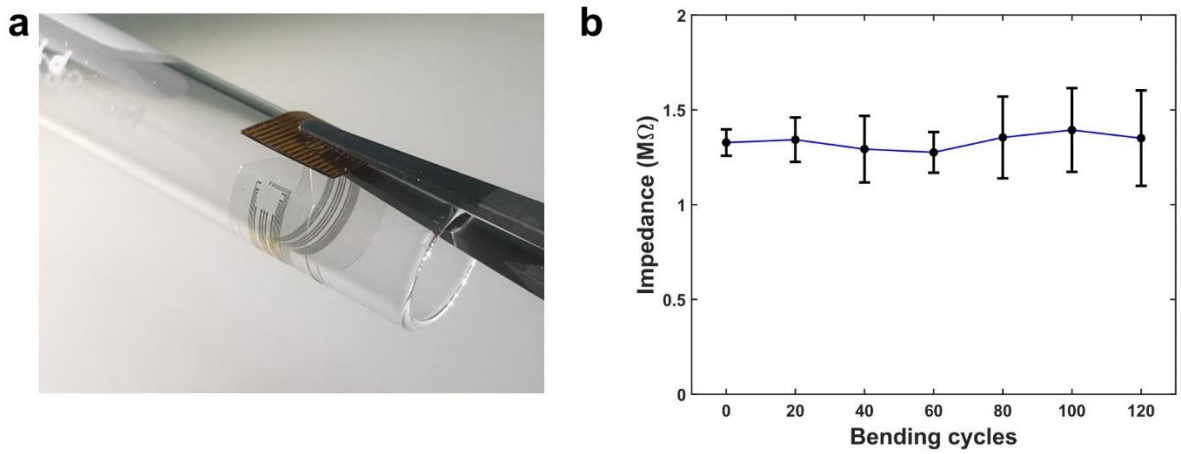
a
b
Impedance (MΩ)
Bending cycles
0
0.5
1
1.5
2
0
20
40
60
80
100
120

Figure 2. S5 *In vitro* test of 2-photon imaging resolution with fluorescent beads.

(a) 1-µm fluorescent beads were embedded in mounting medium. Z stacks (200×200 pixels, pixel size: 100×100 nm, Z step size: 1 µm) of individual beads beside the array (Control), below the array substrate (Substrate), and below graphene microelectrode (Graphene) were acquired with 2-photon excitation at 800 nm through a 20×/0.5 NA objective. (b) Representative intensity profiles (after normalization to maximum intensity within the image) of beads beside the array (Control) and below the array (Substrate). The XY image shows the focal plane with respective line profiles along X and Y axis; XZ and YZ images are maximum intensity projections (MIPs) along the third axis. Scale bars, 1 µm (c) Quantification of full width at half-maximum (FWHM) with a Gaussian peak function (performed in MetroloJ plugin in ImageJ). Mean ± standard deviation of 3-4 beads per condition are shown (symbols represent average of 3 measurements of an individual bead).

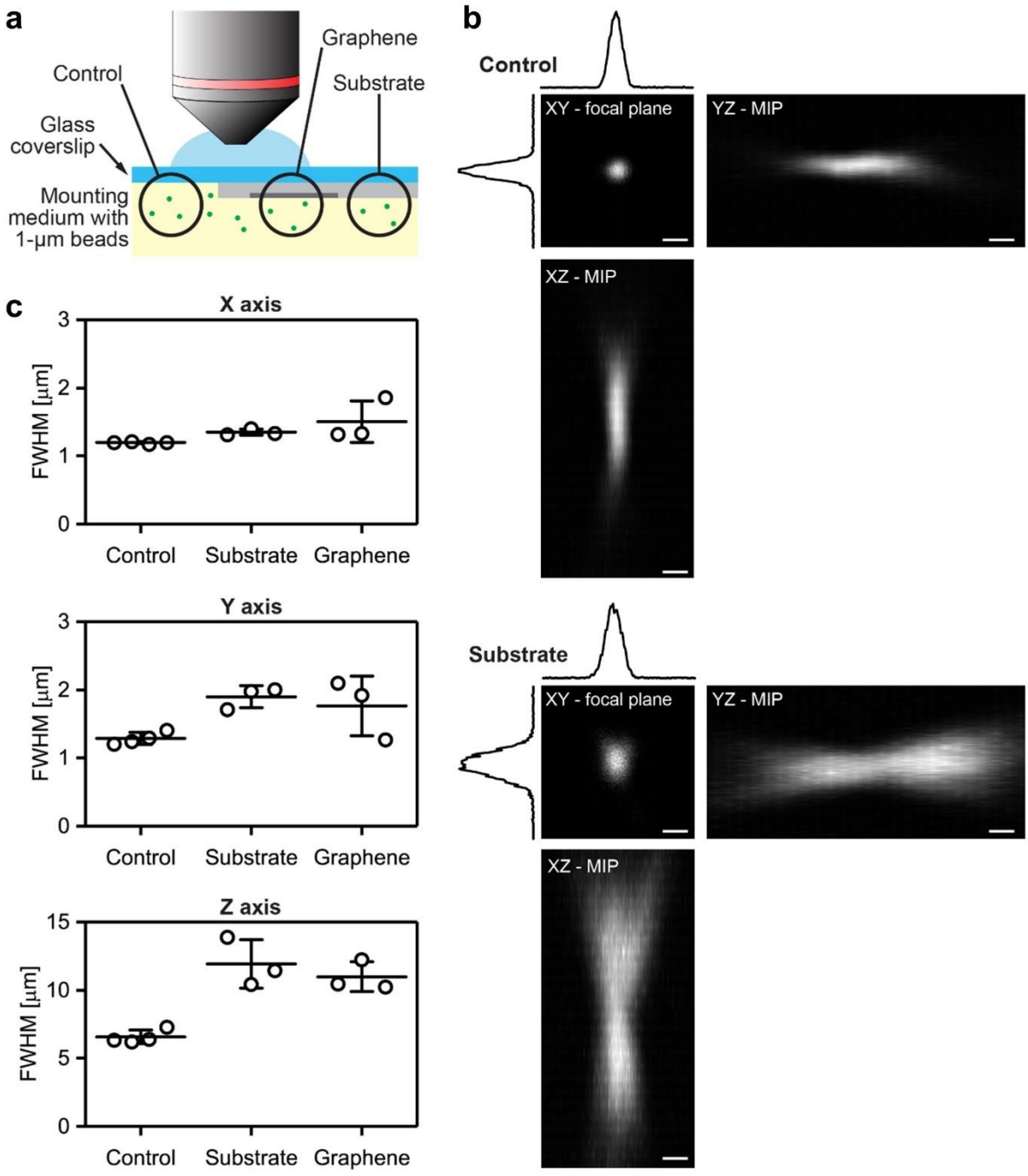
a
Control
Graphene
Substrate
Glass coverslip
Mounting medium with 1-µm beads
b
Control
XY - focal plane
YZ - MIP
XZ - MIP
Substrate
XY - focal plane
YZ - MIP
XZ - MIP
c
X axis
FWHM [µm]
0
1
2
3
Control
Substrate
Graphene
Y axis
FWHM [µm]
0
1
2
3
Control
Substrate
Graphene
Z axis
FWHM [µm]
0
5
10
15
Control
Substrate
Graphene

Figure 2. S6 Setup for in-vitro characterization of light-induced artifacts.

Panels shown here are a gold electrode array with (a) 470-nm LED stimulation off and (b) 470-nm LED stimulation on.

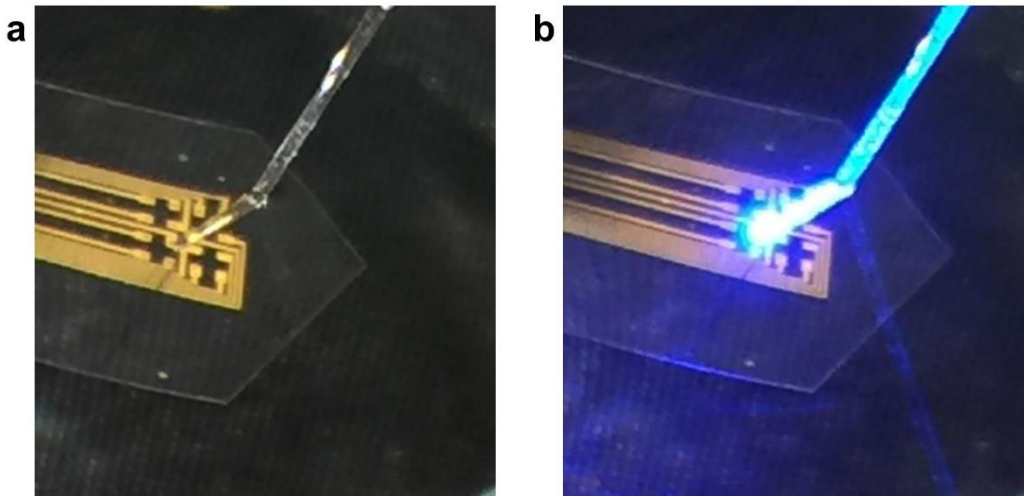
a
b

Figure 2. S7 *In vitro* analysis of light-induced artifacts in graphene and gold microelectrode arrays.

(a) Time series of light-induced artifacts in gold microelectrode arrays upon illumination with 0-54.1 mW mm^{-2} (20-ms light pulse from a fiber-coupled 470-nm LED). Measurements were performed in PBS (b) Artifact amplitudes for graphene and gold electrode in dependence of laser pulse intensity. (c), (d) Power spectra for 10-Hz illumination of graphene (C) or gold electrode (d). (e) Amplitudes of light-induced artifacts for a graphene electrode upon illumination with 473-nm laser light with 0-240.7 mW mm^2 for 1, 5, or 10 ms through a 20× microscope objective (using the same setup as for animal experiments shown in Figure 5 and 6). Amplitude of the light-induced artifact of the graphene electrode is below the noise level for light pulse intensities <60.2 mW mm^{-2}. In this setup, the graphene microelectrode array was placed on an agarose phantom and covered with a glass coverslip.

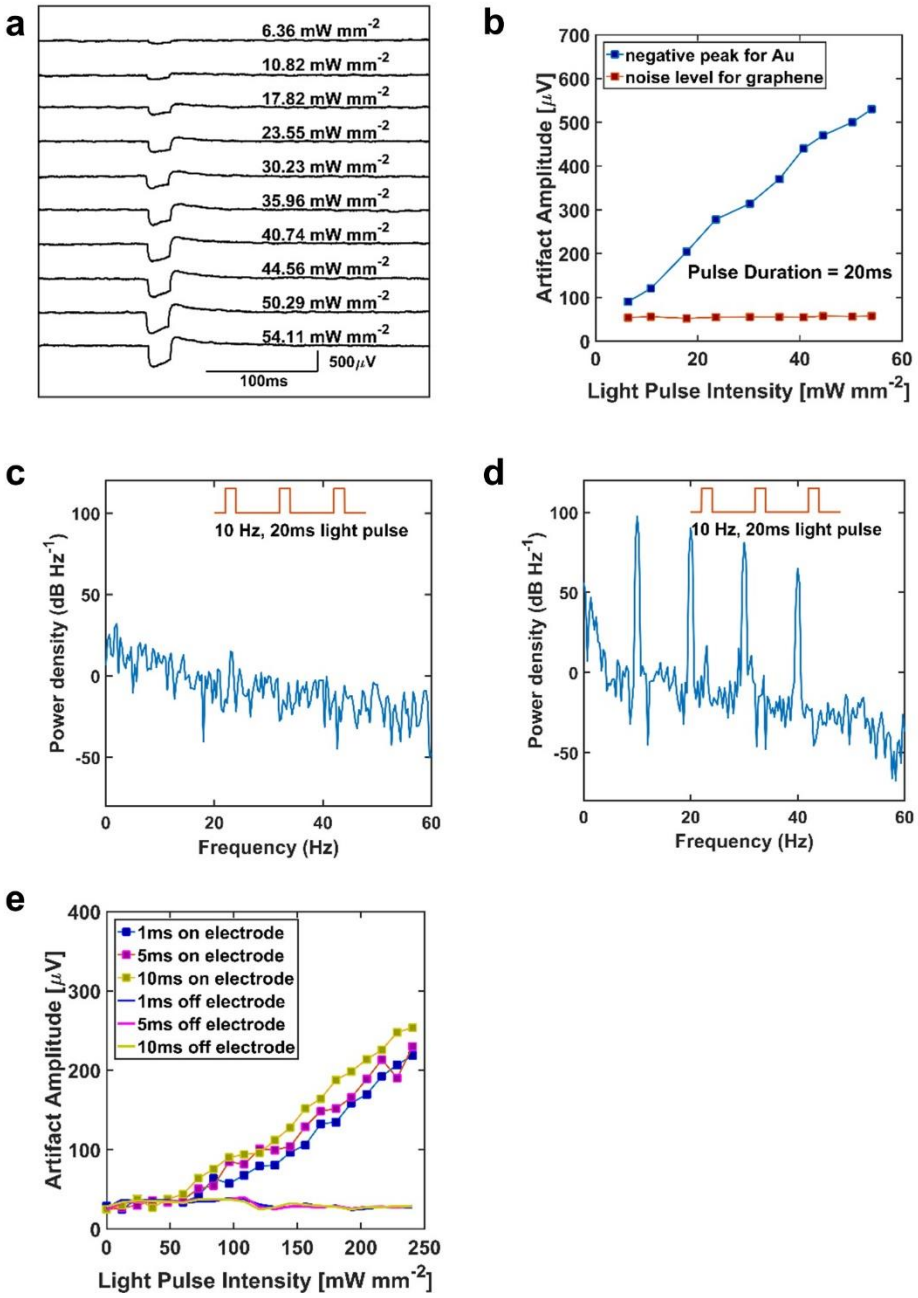
a
6.36 mW mm-2
10.82 mW mm-2
17.82 mW mm-2
23.55 mW mm-2
30.23 mW mm-2
35.96 mW mm-2
40.74 mW mm-2
44.56 mW mm-2
50.29 mW mm-2
54.11 mW mm-2
500μV
100ms
b
negative peak for Au
noise level for graphene
Pulse Duration = 20ms
Artifact Amplitude [μV]
Light Pulse Intensity [mW mm-2]
c
10 Hz, 20ms light pulse
Power density (dB Hz-1)
Frequency (Hz)
d
10 Hz, 20ms light pulse
Power density (dB Hz-1)
Frequency (Hz)
e
1ms on electrode
5ms on electrode
10ms on electrode
1ms off electrode
5ms off electrode
10ms off electrode
Artifact Amplitude [μV]
Light Pulse Intensity [mW mm-2]

Figure 2. S8 Additional experiment for correlation of Ca^{2+} signal and LFP amplitude.

A representative field of view (FOV, top) containing six OGB1-stained neurons (green) and one SR101/OGB1-stained astrocyte (yellow), respective Ca^{2+} traces (middle) of neurons (n1-n6) and neuropil (np) given as ΔF/F, and corresponding LFP recordings (bottom) of the graphene microelectrode adjacent to the FOV used for Ca^{2+} imaging (6 trials in one run are shown). Red arrows indicate delivery of a single electric stimulus (300 μs, 1 mA) to the contralateral whisker pad.

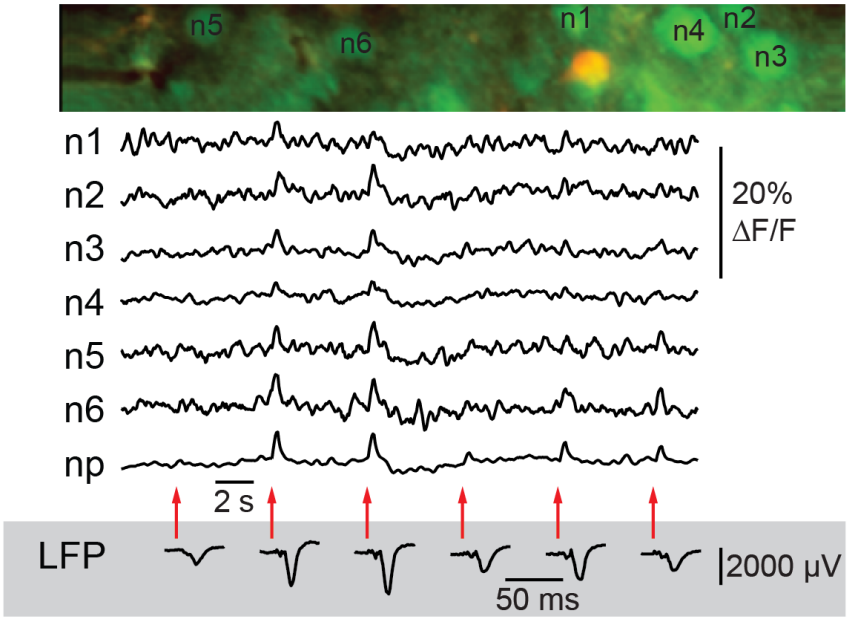
n5
n6
n1
n4
n2
n3
n1
n2
n3
n4
n5
n6
np
20%
ΔF/F
2 s
LFP
2000 μV
50 ms

Figure 2. S9 Two-photon laser scanning induces only minor artifacts in electrical recordings with graphene electrodes in vivo.

(a) Overview of the preparation with graphene microelectrode array. Yellow outlines represent single graphene electrodes, white rectangles indicate locations of 2-photon imaging, the green rectangle indicates which electrode traces are shown in panels B-D. Scale bar, 500 µm. (b) Imaging was performed between two graphene electrodes. (c) The 2-photon laser beam was focused on a gold wire (highlighted in yellow in panel A); the respective electrode channel is highlighted in red. (d) The 2-photon laser beam is focused on a graphene electrode; the corresponding electrode channel is highlighted in red. In B-D, recordings from 6 electrodes (corresponding to the green rectangle in panel A) are shown. For each location, imaging was performed at a depth of 250 µm below the surface with a laser power of 5 mW and at a depth of 500 µm with a power of 20 mW. The laser was set to an excitation wavelength of 800 nm; imaging was performed with a 20× objective and 4× optical zoom to acquire images with a size of 150 µm×150 µm at a resolution of 512×512 pixels.

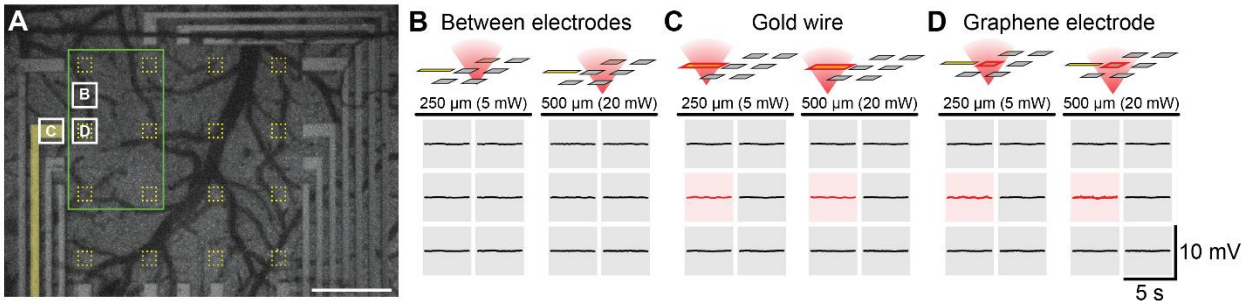
A
B
C
D
B Between electrodes
C Gold wire
D Graphene electrode
250 µm (5 mW)
500 µm (20 mW)
250 µm (5 mW)
500 µm (20 mW)
250 µm (5 mW)
500 µm (20 mW)
10 mV
5 s

Figure 2. S10 Vascular responses are absent upon 473-nm laser illumination in a wild-type (ChR2-negative) animal.

(a) As in experiments with Thy1-ChR2 mice (see **Figure 2.6**), blood plasma was labeled with 2-MDa FITC-dextran, and single cortical arterioles (at locations 1, 2, and 3) were imaged in line-scan mode. Yellow squares indicate positions of individual graphene electrodes. Scale bar, 500 μm. (b) Reference images of the 3 arterioles (left) and corresponding time courses of vessel diameters changes (right, 3 trials per arteriole). Red arrows indicate where line scans were performed, blue arrows indicate illumination with 473-nm laser through the objective (100 ms, 7.1 mW). Scale bars, 20 μm.

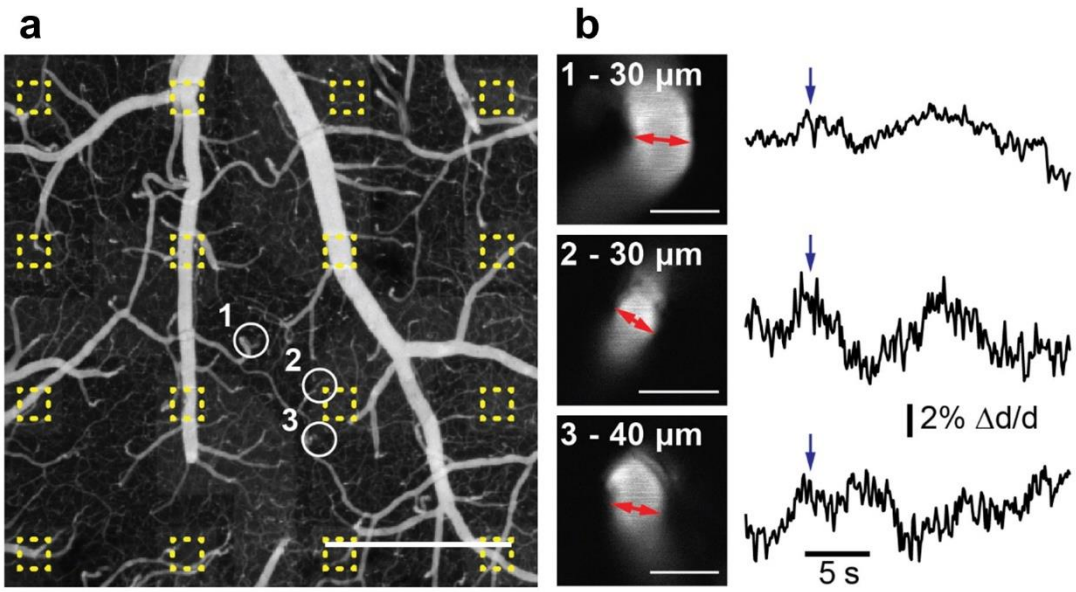
a
b
1
2
3
1 - 30 µm
2 - 30 µm
3 - 40 µm
2% Δd/d
5 s

2.8 Reference

1 Uhlirova, H., Tian, P., Sakadžić, S., Gagnon, L., Thunemann, M., Desjardins, M., Saisan, P. A., Nizar, K., Yaseen, M. A. & Hagler Jr, D. J. The roadmap for estimation of cell-type-specific neuronal activity from non-invasive measurements. *Philosophical Transactions of the Royal Society B: Biological Sciences* **371**, 20150356 (2016).

2 Kuzum, D., Takano, H., Shim, E., Reed, J. C., Juul, H., Richardson, A. G., De Vries, J., Bink, H., Dichter, M. A. & Lucas, T. H. Transparent and flexible low noise graphene electrodes for simultaneous electrophysiology and neuroimaging. *Nature communications* **5**, 5259 (2014).

3 Park, D.-W., Schendel, A. A., Mikael, S., Brodnick, S. K., Richner, T. J., Ness, J. P., Hayat, M. R., Atry, F., Frye, S. T. & Pashaie, R. Graphene-based carbon-layered electrode array technology for neural imaging and optogenetic applications. *Nature communications* **5**, 1-11 (2014).

4 Cardin, J. A., Carlén, M., Meletis, K., Knoblich, U., Zhang, F., Deisseroth, K., Tsai, L.-H. & Moore, C. I. Targeted optogenetic stimulation and recording of neurons in vivo using cell-type-specific expression of Channelrhodopsin-2. *Nature protocols* **5**, 247 (2010).

5 Wu, F., Stark, E., Im, M., Cho, I.-J., Yoon, E.-S., Buzsáki, G., Wise, K. D. & Yoon, E. An implantable neural probe with monolithically integrated dielectric waveguide and recording electrodes for optogenetics applications. *Journal of neural engineering* **10**, 056012 (2013).

6 Mikulovic, S., Pupe, S., Peixoto, H. M., Do Nascimento, G. C., Kullander, K., Tort, A. B. & Leão, R. N. On the photovoltaic effect in local field potential recordings. *Neurophotonics* **3**, 015002 (2016).

7 Han, X., Qian, X., Bernstein, J. G., Zhou, H.-h., Franzesi, G. T., Stern, P., Bronson, R. T., Graybiel, A. M., Desimone, R. & Boyden, E. S. Millisecond-timescale optical control of neural dynamics in the nonhuman primate brain. *Neuron* **62**, 191-198 (2009).

8 Lin, Y.-C., Lu, C.-C., Yeh, C.-H., Jin, C., Suenaga, K. & Chiu, P.-W. Graphene annealing: how clean can it be? *Nano letters* **12**, 414-419 (2012).

9 Wang, Y., Zheng, Y., Xu, X., Dubuisson, E., Bao, Q., Lu, J. & Loh, K. P. Electrochemical delamination of CVD-grown graphene film: toward the recyclable use of copper catalyst. *ACS nano* **5**, 9927-9933 (2011).

10 Tamamaki, N., Yanagawa, Y., Tomioka, R., Miyazaki, J. I., Obata, K. & Kaneko, T. Green fluorescent protein expression and colocalization with calretinin, parvalbumin, and somatostatin in the GAD67-GFP knock-in mouse. *Journal of Comparative Neurology* **467**, 60-79 (2003).

11 Kobat, D., Durst, M. E., Nishimura, N., Wong, A. W., Schaffer, C. B. & Xu, C. Deep tissue multiphoton microscopy using longer wavelength excitation. *Optics express* **17**, 13354-13364 (2009).

12 Nimmerjahn, A., Kirchhoff, F., Kerr, J. N. & Helmchen, F. Sulforhodamine 101 as a specific marker of astroglia in the neocortex in vivo. *Nature methods* **1**, 31-37 (2004).

13 Stosiek, C., Garaschuk, O., Holthoff, K. & Konnerth, A. In vivo two-photon calcium imaging of neuronal networks. *Proceedings of the National Academy of Sciences* **100**, 7319-7324 (2003).

14 Garaschuk, O., Milos, R.-I. & Konnerth, A. Targeted bulk-loading of fluorescent indicators for two-photon brain imaging in vivo. *Nature protocols* **1**, 380-386 (2006).

15 Helmchen, F., Svoboda, K., Denk, W. & Tank, D. W. In vivo dendritic calcium dynamics in deep-layer cortical pyramidal neurons. *Nature neuroscience* **2**, 989-996 (1999).

16 Uhlirova, H., Kılıç, K., Tian, P., Thunemann, M., Desjardins, M., Saisan, P. A., Sakadžić, S., Ness, T. V., Mateo, C. & Cheng, Q. Cell type specificity of neurovascular coupling in cerebral cortex. *elife* **5**, e14315 (2016).

17 Wang, H., Peca, J., Matsuzaki, M., Matsuzaki, K., Noguchi, J., Qiu, L., Wang, D., Zhang, F., Boyden, E. & Deisseroth, K. High-speed mapping of synaptic connectivity using photostimulation in Channelrhodopsin-2 transgenic mice. *Proceedings of the National Academy of Sciences* **104**, 8143-8148 (2007).

18 Rungta, R. L., Osmanski, B.-F., Boido, D., Tanter, M. & Charpak, S. Light controls cerebral blood flow in naive animals. *Nature communications* **8**, 1-9 (2017).

19 Devor, A., Bandettini, P. A., Boas, D. A., Bower, J. M., Buxton, R. B., Cohen, L. B., Dale, A. M., Einevoll, G. T., Fox, P. T. & Franceschini, M. A. The challenge of connecting the dots in the BRAIN. *Neuron* **80**, 270-274 (2013).

20 Insel, T. R., Landis, S. C. & Collins, F. S. The NIH brain initiative. *Science* **340**, 687-688 (2013).

21 Segev, E., Reimer, J., Moreaux, L. C., Fowler, T. M., Chi, D., Sacher, W. D., Lo, M., Deisseroth, K., Tolias, A. S. & Faraon, A. Patterned photostimulation via visible-wavelength photonic probes for deep brain optogenetics. *Neurophotonics* **4**, 011002 (2016).

22 Pisanello, F., Sileo, L. & De Vittorio, M. Micro-and nanotechnologies for optical neural interfaces. *Frontiers in neuroscience* **10**, 70 (2016).

23 Pisanello, F., Sileo, L., Oldenburg, I. A., Pisanello, M., Martiradonna, L., Assad, J. A., Sabatini, B. L. & De Vittorio, M. Multipoint-emitting optical fibers for spatially addressable in vivo optogenetics. *Neuron* **82**, 1245-1254 (2014).

24 Wu, F., Stark, E., Ku, P.-C., Wise, K. D., Buzsáki, G. & Yoon, E. Monolithically integrated μLEDs on silicon neural probes for high-resolution optogenetic studies in behaving animals. *Neuron* **88**, 1136-1148 (2015).

25 Kampasi, K., Stark, E., Seymour, J., Na, K., Winful, H. G., Buzsáki, G., Wise, K. D. & Yoon, E. Fiberless multicolor neural optoelectrode for in vivo circuit analysis. *Scientific reports* **6**, 1-13 (2016).

26 Lee, J., Ozden, I., Song, Y.-K. & Nurmikko, A. V. Transparent intracortical microprobe array for simultaneous spatiotemporal optical stimulation and multichannel electrical recording. *Nature methods* **12**, 1157-1162 (2015).

27 Kobat, D., Horton, N. G. & Xu, C. In vivo two-photon microscopy to 1.6-mm depth in mouse cortex. *Journal of biomedical optics* **16**, 106014 (2011).

28 Theer, P. & Denk, W. On the fundamental imaging-depth limit in two-photon microscopy. *JOSA A* **23**, 3139-3149 (2006).

29 Kunori, N. & Takashima, I. A transparent epidural electrode array for use in conjunction with optical imaging. *Journal of neuroscience methods* **251**, 130-137 (2015).

30 Theriot, J. J., Toga, A. W., Prakash, N., Ju, Y. S. & Brennan, K. Cortical sensory plasticity in a model of migraine with aura. *Journal of Neuroscience* **32**, 15252-15261 (2012).

31 Park, D.-W., Brodnick, S. K., Ness, J. P., Atry, F., Krugner-Higby, L., Sandberg, A., Mikael, S., Richner, T. J., Novello, J. & Kim, H. Fabrication and utility of a transparent graphene neural electrode array for electrophysiology, in vivo imaging, and optogenetics. *Nature protocols* **11**, 2201-2222 (2016).

32 Yu, K. J., Kuzum, D., Hwang, S.-W., Kim, B. H., Juul, H., Kim, N. H., Won, S. M., Chiang, K., Trumpis, M. & Richardson, A. G. Bioresorbable silicon electronics for transient spatiotemporal mapping of electrical activity from the cerebral cortex. *Nature materials* **15**, 782-791 (2016).

33 Buzsáki, G., Anastassiou, C. A. & Koch, C. The origin of extracellular fields and currents—EEG, ECoG, LFP and spikes. *Nature reviews neuroscience* **13**, 407-420 (2012).

34 Einevoll, G. T., Kayser, C., Logothetis, N. K. & Panzeri, S. Modelling and analysis of local field potentials for studying the function of cortical circuits. *Nature Reviews Neuroscience* **14**, 770-785 (2013).

35 Haslinger, R., Ulbert, I., Moore, C. I., Brown, E. N. & Devor, A. Analysis of LFP phase predicts sensory response of barrel cortex. *Journal of Neurophysiology* **96**, 1658-1663 (2006).

36 Castro-Alamancos, M. A. Cortical up and activated states: implications for sensory information processing. *The Neuroscientist* **15**, 625-634 (2009).

37 Tian, P., Teng, I. C., May, L. D., Kurz, R., Lu, K., Scadeng, M., Hillman, E. M., De Crespigny, A. J., D'Arceuil, H. E. & Mandeville, J. B. Cortical depth-specific microvascular dilation underlies laminar differences in blood oxygenation level-dependent functional MRI signal. *Proceedings of the National Academy of Sciences* **107**, 15246-15251 (2010).

38 Peterka, D. S., Takahashi, H. & Yuste, R. Imaging voltage in neurons. *Neuron* **69**, 9-21 (2011).

39 Grienberger, C. & Konnerth, A. Imaging calcium in neurons. *Neuron* **73**, 862-885 (2012).

40 Nizar, K., Uhlirova, H., Tian, P., Saisan, P. A., Cheng, Q., Reznichenko, L., Weldy, K. L., Steed, T. C., Sridhar, V. B. & MacDonald, C. L. In vivo stimulus-induced vasodilation occurs without IP3 receptor activation and may precede astrocytic calcium increase. *Journal of Neuroscience* **33**, 8411-8422 (2013).

41 Davalos, D., Grutzendler, J., Yang, G., Kim, J. V., Zuo, Y., Jung, S., Littman, D. R., Dustin, M. L. & Gan, W.-B. ATP mediates rapid microglial response to local brain injury in vivo. *Nature neuroscience* **8**, 752-758 (2005).

42 Sakadžić, S., Yaseen, M. A., Jaswal, R., Roussakis, E., Dale, A. M., Buxton, R. B., Vinogradov, S. A., Boas, D. A. & Devor, A. Two-photon microscopy measurement of cerebral metabolic rate of oxygen using periarteriolar oxygen concentration gradients. *Neurophotonics* **3**, 045005 (2016).

43 Dombeck, D. A., Khabbaz, A. N., Collman, F., Adelman, T. L. & Tank, D. W. Imaging large-scale neural activity with cellular resolution in awake, mobile mice. *Neuron* **56**, 43-57 (2007).

44 Goldey, G. J., Roumis, D. K., Glickfeld, L. L., Kerlin, A. M., Reid, R. C., Bonin, V., Schafer, D. P. & Andermann, M. L. Removable cranial windows for long-term imaging in awake mice. *Nature protocols* **9**, 2515 (2014).

45 Ji, N., Milkie, D. E. & Betzig, E. Adaptive optics via pupil segmentation for high-resolution imaging in biological tissues. *Nature methods* **7**, 141-147 (2010).

46 Sofroniew, N. J., Flickinger, D., King, J. & Svoboda, K. A large field of view two-photon mesoscope with subcellular resolution for in vivo imaging. *Elife* **5**, e14472 (2016).

47 Ma, Y., Shaik, M. A., Kozberg, M. G., Kim, S. H., Portes, J. P., Timerman, D. & Hillman, E. M. Resting-state hemodynamics are spatiotemporally coupled to synchronized and symmetric neural activity in excitatory neurons. *Proceedings of the National Academy of Sciences* **113**, E8463-E8471 (2016).

48 Shin, H. K., Jones, P. B., Garcia-Alloza, M., Borrelli, L., Greenberg, S. M., Bacskai, B. J., Frosch, M. P., Hyman, B. T., Moskowitz, M. A. & Ayata, C. Age-dependent cerebrovascular dysfunction in a transgenic mouse model of cerebral amyloid angiopathy. *Brain* **130**, 2310-2319 (2007).

49 Dunn, A. K., Devor, A., Bolay, H., Andermann, M. L., Moskowitz, M. A., Dale, A. M. & Boas, D. A. Simultaneous imaging of total cerebral hemoglobin concentration, oxygenation, and blood flow during functional activation. *Optics letters* **28**, 28-30 (2003).

50 Jones, M., Berwick, J. & Mayhew, J. Changes in blood flow, oxygenation, and volume following extended stimulation of rodent barrel cortex. *Neuroimage* **15**, 474-487 (2002).

51 Mayhew, J., Johnston, D., Berwick, J., Jones, M., Coffey, P. & Zheng, Y. Spectroscopic analysis of neural activity in brain: increased oxygen consumption following activation of barrel cortex. *Neuroimage* **12**, 664-675 (2000).

52 Matthews, C. & Cordelieres, F. P. in *ImageJ User & Developer Conference proceedings.*

Chapter 3. Ultralow Impedance Graphene Microelectrodes with High Optical Transparency for Simultaneous Deep Two-Photon Imaging in Transgenic Mice

3.1 Abstract

The last decades have witnessed substantial progress in optical technologies revolutionizing our ability to record and manipulate neural activity in genetically modified animal models. Meanwhile, human studies mostly rely on electrophysiological recordings of cortical potentials, which cannot be inferred from optical recordings, leading to a gap between our understanding of dynamics of microscale populations and brain-scale neural activity. By enabling concurrent integration of electrical and optical modalities, transparent graphene microelectrodes can close this gap. However, the high impedance of graphene constitutes a big challenge towards the widespread use of this technology. Here, we experimentally demonstrate that this high impedance of graphene microelectrodes is fundamentally limited by quantum capacitance. We overcome this quantum capacitance limit by creating a parallel conduction path using platinum nanoparticles. We achieve a 100 times reduction in graphene electrode impedance, while maintaining the high optical transparency crucial for deep 2-photon microscopy. Using a transgenic mouse model, we demonstrate simultaneous electrical recording of cortical activity with high fidelity while imaging calcium signals at various cortical depths right beneath the transparent microelectrodes. Multimodal analysis of Ca^{2+} spikes and cortical surface potentials offers unique opportunities to bridge our understanding of cellular dynamics and brain-scale neural activity.

3.2 Introduction

Electrophysiology has been the backbone of neuroscience research for decades [1,2]. Despite many advantages, it is often difficult to record from large number of neurons (~1000 cells)

simultaneously and from large areas across different brain regions. Last decades have witnessed rapid advancements in optical imaging, such as two-photon calcium imaging, for monitoring hundreds of cells in neuronal microcircuits.[3-6] However, slow kinetics of indicators and low frame acquisition rates of typical imaging setups substantially limit the maximum temporal resolution that can be achieved using optical imaging [7,8]. Furthermore, neuronal populations display emergent features such as oscillations, waves, synchrony, and sequential activation patterns, which have been historically used as the basis of electrocorticography (ECoG) recordings in clinical studies with human patients. Linking these macro-scale features to activities of individual neurons and global effects of these features on the brain activity remain elusive due to the lack of technologies permitting concurrent cellular-scale recordings and whole brain activity monitoring.

To this end, transparent graphene electrodes have recently been suggested to enable integration of electrophysiology with optical imaging techniques in multimodal experiments [9-11]. Owing to unique combination of properties including high mobility, low noise, flexibility and optical transparency, graphene has been intensively investigated for electronics [12-18] and sensing applications [19,20]. On the other hand, for neural recordings, the impedance of graphene microelectrodes has been relatively high impacting sensitivity of measurements and wide-spread adaptation of the technology for various basic neuroscience and medical applications. Furthermore, high impedance of monolayer graphene constitutes a fundamental roadblock towards scaling graphene microelectrode dimensions to record single neuron activity. In addition, it constitutes a big challenge towards use of graphene electrodes for electrical stimulation in future. Chemical doping techniques have been shown to reduce the impedance of monolayer graphene to some extent [21,22]. However, the decrease in impedance is not sufficient to scale electrode dimensions

to single cell regime. In addition, other techniques such as deposition of porous films or multilayer graphene flakes cannot be employed since they penalize the optical transparency. Transparent materials, such as indium tin oxide (ITO) have also been investigated as the electrode material for transparent microelectrode arrays [23,24]. However, ITO is brittle; though widely employed in solar cells and display panels, it is susceptible to cracking and mechanical degradation when used for flexible neural interfaces.[10,23,24] Here we show that the impedance of the graphene electrodes is fundamentally limited by quantum capacitance, which originates from the graphene's low density of states around Dirac point [25]. We report an effective method to electrodeposit platinum nanoparticles (PtNPs) on transparent chemical vapor deposited (CVD) graphene electrodes to beat the quantum capacitance limit and lower the impedance 100 times while maintaining optical transparency. Employing electrochemical impedance analysis and equivalent circuit modeling, we explain how electrodeposited PtNPs can overcome the quantum capacitance limit and decrease the impedance. PtNPs do not impede the transparency of neural electrodes or obstruct delivery of light to deeper layers in the tissue. Using graphene/PtNP microelectrode arrays, we demonstrate simultaneous *in vivo* calcium imaging of cellular activity at multiple cortical depths while recording field potentials generated by neural populations from the cortical surface. Multimodal analysis of Ca^{2+} spikes and cortical surface potentials suggest that somatic Ca^{2+} activity in layer II/III significantly contributes to high frequency gamma band for the surface potentials, while the dendritic Ca^{2+} activity from layer I increases the power in low frequency bands.

3.3 Result and Discussion

3.3.1 Quantum Capacitance Limit for Graphene Microelectrodes

In this work, we first fabricated graphene microelectrode arrays with 100 μm electrode size and 400 μm spacing (Figure 3.1a). 10 nm chromium and 100 nm gold were deposited on to polyethylene terephthalate (PET) substrate to form the metal wires and the contact pads. Preventing crack formation during graphene transfer and protecting graphene surface from chemical contamination are particularly important to achieve high yield in large area transparent arrays. To that end, we used the "bubbling" transfer method [26] and AZ1512/PMGI bilayer lithography. Graphene pads were then patterned with oxygen plasma etching. And finally, the SU-8 encapsulation layer was defined with photolithography. Details of the fabrication process are described in the methods section and Figure S3.1. Figure 3.1b displays the trilayer structure of the array, where CVD graphene lays between PET substrate and SU-8 encapsulation. Scanning electron microscopy images (Figure S3.2) show that SU-8 encapsulation was well defined by photolithography (no cracks) and the graphene surface has no obvious polymer residue. The graphene/electrolyte interface was then characterized with electrochemical impedance spectroscopy (EIS) and cyclic voltammetry (CV) in 0.01 M phosphate buffered saline (PBS) [27]. EIS was measured at the open circuit potential of the graphene/PBS interface from 1 Hz to 100 KHz (Figure S3.3a). Impedance distribution of a representative array measured at 1 KHz is shown in Figure 3.1c, the average impedance is 872.9 KΩ. Electrodes with impedances lower than 1.5 MΩ can record neural activity with high signal-to-noise ratio, and those with impedance from 1.5 to 3.0 MΩ might still get acceptable signals [28]. Our fabrication process provides 100% yield with all the electrodes in the array exhibiting impedances less than 1.5 MΩ. CV measured from -0.6 to 1.1 V (Figure S3.3b) shows the capacitive characteristics of the graphene interface with no redox peaks, indicating that no Faradaic reactions take place at the interface.

We investigated the origin of high impedance of the graphene microelectrodes by equivalent circuit analysis (Figure 3.1d). The unique band structure of graphene gives rise to quantum capacitance (C_Q), which is used to describe the total charge ($Q=q(p-n)$ where q is the electron charge) as a function of electrostatic potential [25]. C_Q around Dirac point is small due to low density of states. Therefore, conventional equivalent circuit models, such as Randles cell used for metal microelectrodes cannot be directly applied to the graphene electrodes. We modified the equivalent circuit model for transparent graphene electrodes to include the quantum capacitance effect (Figure 3.1d). In the equivalent circuit model, R_s is the resistance of the solution, CPE is the constant phase element representing Helmholtz double layer capacitance [27], W_B is the bounded Warburg element used to simulate the diffusion process, and R_{ct} is the charge transfer resistance used to simulate Faradaic reactions. Quantum capacitance of graphene (C_Q) is in series with the CPE. Experimental EIS curves and the fitted equivalent circuit model are plotted in Figure 3.1e. The parameters for the equivalent circuit model are listed in Table 3.1 including mean values and standard deviations (SD), and the corresponding formulae in Note 3.S1. The quantum capacitance of graphene is measured as 2.45 μFcm^{-2}, consistent with experimental and theoretical results in literature [29-31]. The effect of quantum capacitance on the total capacitance is shown in Figure 3.1f. The Helmholtz double layer capacitance is obtained directly from the fitting result. The quantum capacitance is simulated using Equation (3.1) [31], where for graphene $v_F \sim c/300$, and impurity concentration n^* is estimated to be $10^{12}\,cm^{-2}$ to match the fitting result. As the open circuit potential of graphene electrodes typically lies within -100 to 100 mV, quantum capacitance dominates the total capacitance in this region [32] decreasing the total capacitance and giving rise to high impedance for the graphene microelectrodes.

$$C_Q = \frac{2e^2}{\hbar v_F \sqrt{\pi}} \left(\left(\frac{eV}{\hbar v_F \sqrt{\pi}} \right)^2 + \left| n^* \right| \right)^{1/2} \quad (3.1)$$

3.3.2 Overcoming Quantum Capacitance Limit

Introducing dopants by chemical means can increase the quantum capacitance slightly and lead to up to 2-fold decrease in electrochemical impedance [21,22]. However, much larger reductions in impedance cannot be achieved by chemical doping since it only shifts Fermi level slightly away from the Dirac point, and hence the quantum capacitance still dominates the electrochemical characteristics of the interface. Here we propose to overcome quantum capacitance limit of transparent graphene electrodes by creating an alternative conduction path with redox catalysts at the electrode/electrolyte interface. Deposition of platinum nanoparticles (PtNPs) on reduced graphene oxide (RGO) [33-35], functionalized graphene sheet [36], glassy carbon (GC) [37] and graphene/glassy carbon bilayer substrate [38] have been shown to be a compelling approach to boost electroactivity in fuel cell and biochemical sensor applications. In a previous study platinum, gold, and gold-platinum alloy nanoparticles as electrochemical catalysts. PtNPs demonstrated stronger faradaic reaction and pseudo-capacitance than the gold and gold-platinum alloy counterparts, which make PtNPs the best choice for catalysis [34]. However, for those applications, optical transparency was not a requirement. Boosting electroactivity of monolayer graphene while maintaining transparency is yet to be demonstrated. Here we developed a process for electrodeposition of Pt nanoparticles (PtNPs) on monolayer CVD graphene as follows. In a two-electrode cell configuration, the graphene array was connected to the working electrode, and a Pt wire (gauge 25) to the auxiliary electrode (Figure S3.4). Both electrodes are immersed into 5 mM H_2PtCl_6 and 10 mM K_2HPO_4 solution. A current of 500 nA was flown out from the graphene array for multiple time periods (5, 10, 20, 30, and 50 seconds) to deposit PtNPs. SEM

images were taken to validate in the electrodeposition, as shown in Figure 3.2. Comparing Figure 3.2a, 3.2b, and 3.2c, as the deposition time increases, PtNPs coverage of the graphene surface increases. The coverage percentage with respect to deposition time is shown in Figure S3.5. The bottom row (Figure 3.2d, 3.2e, and 3.2f) emphasizes the shape and size of the PtNPs. Diameters of PtNPs are mostly below 100 nm for 5 seconds deposition and above 250 nm for 50 seconds. 20 seconds deposition has some particles with 100 nm diameter, while the others around 200 nm. Similar trend applies for the surface roughness, longer deposition results in larger particle size and rougher surface. The size and surface roughness effect can be explained by the location of the reduction of $PtCl_6^{2-}$ ions [37]. If the reduction happens on graphene surface, it produces PtNPs with smooth surface and small size, as is the case for most PtNPs in 5 seconds deposition. If the reduction happens on an existing PtNP, it increases the surface roughness and the size, as is the case for most of the PtNPs in 50 seconds deposition.

The PtNPs/Graphene electrodes were characterized with EIS and CV. EIS of PtNP/Graphene shows that the impedance significantly decreases as deposition time increases (Figure 3.3a). The impedances at 1 KHz are plotted as a function of deposition time including the impedance of the bare graphene microelectrodes in Figure 3.3b. PtNPs deposition achieves a 100-time decrease in the impedance. CV curves of PtNPs/Graphene electrodes show oxide reduction peaks at around -270 mV and hydrogen adsorption peaks at -900 to -400 mV (Figure 3.3c), all of which indicate that Pt is actively engaged in the charge transfer process at electrode/electrolyte interface [37,39,40]. As for simultaneous optical imaging or optogenetics experiments, high transmittance is equally important as the low impedance. We measured the optical transmittance spectra of PtNP/Graphene microelectrodes with different deposition time at the wavelength range from 450 to 850 nm, as shown in Figure 3.3d. Monolayer graphene electrodes have an overall

transmittance above 90%, and PtNP/Graphene electrodes with 30 seconds or less deposition time maintain a transparency above 50%, which is acceptable for simultaneous optical imaging and stimulation experiments.

Circuit models of electrode/electrolyte interface of Pt electrodes have been studied in detail in the literature [41]. We modified equivalent circuit model for the graphene electrodes (Figure 3.1d) to include the effect of PtNPs on the electrochemical interface. Since there are two types of materials, namely PtNPs and graphene, two circuit blocks for PtNPs and graphene respectively are constructed as shown in Figure 3.4a. In the PtNPs block, the infinite Warburg element (W_I) and the pseudo-capacitance (C_p) describing the pseudo-capacitor [42] are needed to simulate how redox energy is stored at the PtNP surface. The parameters for the graphene block are calculated based on the fitting results from Table 1 and surface coverage according to SEM images and then fixed in the model fitting; whereas solution resistance (R_s), Helmholtz double layer capacitance (CPE_{Pt}), W_I, and C_p for the PtNP block are obtained from fitting the model to the experimental results. Figure 4b and 4c demonstrate how the PtNP block (blue dashed curve) dominates the EIS characteristics over the graphene block (red dashed curve) for both 5 seconds and 50 seconds depositions, respectively. Even 5 seconds of electrodeposition cause PtNP block to dominate the total EIS over the graphene block, except at high frequency (above 40 KHz) where solution resistance (R_s) starts to be the dominant factor. This effect becomes more pronounced for 50 seconds deposition, where EIS of the Pt block is around two orders of magnitudes lower than that of the graphene block, so that the Pt dominates the characteristics of the electrode/electrolyte interface. These results suggest that the electrodeposition of PtNPs clearly overcomes the limitation of quantum capacitance of graphene and substantially decreases the total impedance. In addition to the EIS at open circuit potential, Figure 3.4d demonstrates the fitted pseudocapacitance

with respect to the voltage bias at three different regions, namely hydrogen absorption, oxide reduction, and oxide formation, which are characteristic to Pt-based electrochemical interfaces. C_p increases as the voltage bias approaches the hydrogen absorption region, which is consistent with the electrochemical behavior of Pt electrodes reported previously.[20] These results clearly demonstrate that PtNP deposition can overcome quantum capacitance limit of graphene electrodes by introducing a parallel redox path governed by electrochemical characteristics of Pt.

3.3.3 Multimodal Monitoring of Cortical Potentials and Cellular Activity

We investigated whether PtNPs/graphene electrode cause obstruction of light penetration during optical imaging. Simultaneous *in vivo* two-photon calcium imaging and cortical field potential recordings were conducted in transgenic mouse models (cross between CaMKIIa-tTA [43] and tetO-GCaMP6s [44]). The PtNPs/graphene electrode array was placed on cortex centered at 2.2 mm posterior and 2.1 mm lateral relative to bregma, as shown in Figure 3.5a. Details about the surgery for implanting the transparent arrays above cortex and under optical imaging window are described in the methods section. Two-photon imaging was performed at two depths, 50 μm and 250 μm to record signals from different sources. Dense neuropils, including axons and dendrites, were located at 50 μm (Supplementary Movie 3.1) while cell bodies of excitatory neurons were abundant at 250 μm (Supplementary Movie 3.2 and S3.3). Since there are no detected cell bodies at 50 μm, the main source of activity is the potential fluctuations in the neuropil. At 250 μm Ca^{2+} responses from cell bodies are clearly detectable (Figure 3.5b and Supplementary Movie 3.3). Gold wires (yellow dashed lines) connecting transparent graphene electrodes to recording amplifiers and active area of the electrodes (white dashed lines) where PtNPs were deposited are outlined. Electrodes marked as A, B, C and D in Figure 3.5b correspond to PtNPs deposition times of 10, 50, 5, and 5 seconds, respectively. Comparison of two-photon images

directly beneath these electrodes suggests that PtNPs have no impact on the calcium imaging at 250 μm deep regardless of deposition time. Figure 3.5c is the maximum intensity projection of image stacks from 5min record at Electrode B clearly showing cell bodies due to increased magnification. While opaque Au wires block the field of view and prevent imaging of the neurons directly beneath them, the neurons beneath the PtNP/graphene electrodes were clearly imaged with single cell resolution at 250 μm depth due to the high transmittance of the electrodes. Figure S3.7 shows calcium imaging at 5 additional electrodes.

The calcium responses of 4 individual cells (highlighted in Figure 3.5c) are compared to illustrate the high transmittance of PtNP/graphene electrode. Cell 1 and 2 are directly beneath the PtNP/graphene electrode, Cell 3 and 4 do not overlap with PtNP/graphene area. To quantify the Ca^{2+} activities of these cells as shown in Figure 3.5d, we calculated $(F-F_0)/F_0$, where F is the mean fluorescence intensity of pixels under each electrode and F_0 is the 8th percentile of the intensity distribution for the entire recording session. Due to the high transmittance of PtNP/graphene electrode, calcium response of Cell 1 and 2 has a similar signal-to-noise ratio as Cell 3, and 4. These recordings confirm that PtNP/graphene electrodes do not obstruct deep calcium imaging directly beneath the electrodes.

The cortical potentials (μECoG) and the spectrogram recorded by Electrode B are plotted in Figure 3.5e, synchronized with calcium responses in Figure 3.5d. μECoG recordings by Electrode A, C, and D are shown in Figure S3.8. The μECoG shows spontaneous cortical activity recorded in awake animals without any distinct sensory stimulus. It includes contributions from both local and background neural activities. In that sense, similarity or correlation analysis cannot be directly applied to investigate contributions from different depths. Therefore, to further investigate the source of these surface potentials with respect to Ca^{2+} activities, we analyzed

multimodal data consisting of Ca^{2+} spikes and μECoG potentials as explained in Figure 3.5g. The Ca^{2+} response is first smoothed by an 8^{th} order Butterworth low-pass filter, and then a threshold is applied to find the time of each peaks. A 2-second time window prior to each Ca^{2+} peak is applied to the μECoG data, and the power within that time window across different frequency bands is obtained and converted to ratios. As is shown in Figure 3.5f, the power of ECoG oscillations prior to Ca^{2+} peaks at both depths have the same trend over a wide frequency range from δ to high-γ band. However, the power ratios corresponding to Ca^{2+} signals at 50 μm are higher in the low-frequency band (δ and θ band) but lower at high-frequency band (γ and high-γ band), compared to those at 250 μm. This result suggests that synaptic activity from the neuropil mainly contributes to slower ECoG oscillations while spiking activity from cell bodies in deeper layers contributes to higher frequency bands such as γ and high-γ.

Application of transparent graphene microelectrode array technology in animal models combined with various optical techniques will pave the way towards better understanding of neural mechanisms underlying ECoG and electroencephalogram (EEG) signals. This is also important for clinical settings, as ECoG and EEG are often used in humans to indirectly infer underlying neural dynamics and disease mechanisms. The transparent nature of the current technology allows a combination with many existing optical technologies, including voltage imaging, optogenetics, wide-field imaging, in addition to two-photon calcium imaging demonstrated in this manuscript. Transparent graphene array implantation method can also be directly integrated with drug injection in the craniotomy, followed by implantation of the imaging windows. Drug injection procedure [4,45,46] is perfectly compatible with the transparent graphene ECoG array for pharmacological experiments.

3.4 Conclusion

In conclusion, we demonstrated a novel microelectrode array with low impedance and high transmittance for simultaneous electrical recording and optical imaging of neural activity. PtNPs were electrodeposited on monolayer graphene to overcome the quantum capacitance limit and the lack of Faradaic reaction for the graphene electrodes. Equivalent circuit models for both graphene and PtNPs/graphene electrodes are developed to investigate how PtNPs serve as the redox catalyst at the electrode/electrolyte interface and how they decrease the electrochemical impedance by 100 times. Furthermore, *in vivo* experiments with transgenic mice models validated that low impedance transparent graphene electrodes can be successfully employed for combining electrophysiology with optical imaging to support multimodal analysis that cannot be attainable using other approaches. Given the effectiveness of PtNP-electrodeposition, we envision that this technique is potentially applicable to fabricate transparent microelectrode arrays with various geometries specifically tailored towards probing different neural circuits and mechanism in multimodal experiments providing unprecedented spatiotemporal resolution.

3.5 Experimental Section

3.5.1 Graphene Transfer and cleansing

In traditional transfer method, the metal substrate, copper in this case, was removed with wet-etching process [47-49]. However, recent studies report copper etching leaves nanoscale copper residue and makes poly(methyl methacrylate) (PMMA) scaffold more difficult to be removed afterwards [50]. Although the polymer residue is removable in H_2/Ar gas flow at above the decomposition temperature of PMMA (>200˚C) [51], our PET substrate will lose its structure integrity starting at 150 ˚C. Therefore, to protect graphene from chemical contamination and mechanical damage, we adopted the "bubbling" transfer method [26] with a 20 V DC power supply, and 0.05 M NaOH solution. Graphene was also doped in 35% nitric acid for 30 seconds as an

effective way to increase charge carrier concentration during transfer (Figure S3.6). After transfer, the sample needs to be dried completely at room temperature. The dried sample was then baked at 125˚C on a hotplate for 5 minutes to anneal PMMA wrinkles and enhance graphene/substrate bonding. PMMA can be removed by soaking the sample in acetone at room temperature for 20 minutes with gentle agitation. 10 cycles of IPA and DI water (1 minute each cycle each batch) is highly useful as mechanical cleansing.

3.5.2 Device Fabrication

The fabrication started with a 4-inch silicon wafer, cleaned and dehydrated (Figure S3.1a). 30 µm thick Polydimethylsiloxane (PDMS) was spin-coated on the wafer and annealed at 150˚C for 10 min (Figure S3.1b). This silicon wafer coated with PDMS was used as a holder to keep the PET substrate flat during the following processes. A 50 µm thick PET film was then placed on top of the PDMS layer (Figure S3.1c). 10 nm chromium and 100 nm gold were sputtered onto the PET substrate with Denton Discovery 18 Sputter System (Figure S3.1d). Metal wires and contact pads were patterned with photolithography and wet-etching (Gold Etchant TFA, Chromium Etchant 1020AC) (Figure S3.1e). Monolayer graphene was transferred with the method described in detail above (Figure S3.1f). To protect graphene from chemical and mechanical damage during photoresist removal, AZ1512/PMGI bilayer lithography is adopted: (i) 100 nm PMGI SF3 is spin-coated at 3000 rpm for 45 seconds and soft-baked at 125˚C for 5 minutes; (ii) 1.2 µm AZ1512 is spin-coated at 4000 rpm for 45 seconds and soft-baked at 100˚C for 1 minute. The bilayer is then exposed with 135 $mJcm^{-2}$ i-line UV and developed in AZ MIF 300. Graphene contact pads were patterned with oxygen plasma etching (Figure S3.1g). Finally, the whole sample was encapsulated with 8 µm thick SU-8 2005 except openings at the designed regions (Figure S3.1h). Gently peeled

off from the PDMS/silicon wafer holder, the arrays (Figure S3.1i) were ready for electrochemical characterizations.

3.5.3 Electrochemical characterization:

All electrochemical characterizations were performed with Gamry 600 Plus in 0.01 M phosphate buffered saline (Sigma-Aldrich P3813 dry powder dissolved in deionized water). Both EIS and CV were measured with a three-electrode configuration, where Ag/AgCl (gauge 25) and Pt (gauge 25) were used as reference electrode and counter electrode respectively. EIS were measured from 100 KHz to 1 Hz at open circuit potential unless otherwise stated. The AC voltage was 20 mV. CV was measured from -0.9 to 1 V vs Ag/AgCl for PtNP/graphene electrodes. 10 cycles of CV were measured to stabilize the electrode/electrolyte interface, and the 10^{th} cycle was presented. To avoid electromagnetic noise, especially the 60 Hz one, the entire setup was placed inside of a Faraday cage.

3.5.4 Surgery

Adult mice (cross between CaMKIIa-tTA (JAX 003010) [43] and tetO-GCaMP6s (JAX 024742) [44], 2 months old) were anesthetized with isoflurane (3% for induction and 1% for maintenance) and a circular piece of scalp was removed. After cleaning the underlying bone using a razor blade, a custom-built head-post was implanted to the exposed skull (~1 mm posterior to lambda) with cyanoacrylate glue and cemented with dental acrylic (Lang Dental). A stainless-steel screw (F000CE156, J.I. Morris) was implanted over cerebellum (~0.5 mm posterior to lambda) as reference. A square craniotomy was made over the right hemisphere and the craniotomized area was 0-4.5 mm posterior and 0.3–4.0 mm lateral to bregma. The transparent PtNPs/graphene electrode array centered at 2.2 mm posterior and 2.1 mm lateral relative to bregma was placed on

cortex. Cortical areas covered by the electrode array included primary somatosensory cortex (S1), posterior parietal cortex (PPC), primary visual cortex (V1) and secondary visual cortex (V2). An imaging window consisting of a glass plug glued on to a larger glass base was placed on top of the electrode array. 3% agarose was applied to fill the gap between the skull and the window, and the window was further secured with vetbond (3M) and dental acrylic. A cocktail of dexamethasone (2 mg/kg body weight), buprenorphine (0.1 mg/kg body weight) and baytril (10 mg/kg body weight) was given at the end of surgery. The animal was returned to the home cage and fully recovered from anesthesia before recording.

3.5.5 In vivo calcium imaging

Two-photon imaging was conducted for a head-fixed awake mouse through a 16 × 0.8 NA objective (Nikon) mounted on a commercial two-photon microscope (B-scope, Thorlabs) and using a 925-nm laser (Ti:sapphire laser, Newport). Images were acquired at ~29 Hz and a resolution of 512 × 512 pixels, covering either 944 × 1016 μm (Fig 5b) or 189 × 203 μm (Fig 5c). Acquired images were motion corrected offline. For quantification of Ca^{2+} signals from cell bodies, fluorescence time course of each cellular ROI and its surrounding neuropil ROI was extracted using Suite2P package. Then fluorescence signal of a cell body was estimated with $F_{cellbody} = F_{cellROI} - 0.7 * F_{neuropilROI}$ as described previously [52,53]. $\Delta F/F$ was computed as $(F_{cellbody} - F_0)/F_0$, where F_0 is the 8th percentile of the intensity distribution during 5 min recording session. For quantification of Ca^{2+} signals at the depth of 50 μm and 250 μm, we drew ROIs along the edges of each electrode.

3.6 Acknowledgments

We would like to acknowledge Office of Naval Research Young Investigator Award (N00014161253), National Science Foundation (ECCS-1752241, ECCS-1734940), San Diego Frontiers of Innovation Scholars Program, Kavli Institute for Brain and Mind Innovative Research, and NIH (R01 NS091010A, R01 EY025349, R01 DC014690, U01 NS094342, P30EY022589) for funding this research. This work was performed in part at the San Diego Nanotechnology Infrastructure (SDNI) of UCSD, a member of the National Nanotechnology Coordinated Infrastructure, which is supported by the National Science Foundation (Grant ECCS-1542148).

Chapter 3 is a reprint of Y. Lu, X. Liu, R. Hattori, C. Ren, X. Zhang, T. Komiyama, D. Kuzum, Ultralow Impedance Graphene Microelectrodes with High Optical Transparency for Simultaneous Deep Two-Photon Imaging in Transgenic Mice, Advanced Functional Materials 28, 1800002 (2018). The dissertation author was the first author of this article.

3.7 Figures

Figure 3. 1 Transparent Graphene Microelectrode Array.

(a) A photo of the array in comparison with a dime. The inset is a microscopic image of the 4-by-4 array of the SU-8 openings. (b) Schematic shows three layers of the array. The top layer is SU-8 encapsulation, the bottom layer is PET substrate with metal wires and contact pads, and the layer in between is monolayer graphene. (c) The electrochemical impedance at 1 KHz of 16 channels in an array, and the average impedance is 872.9 KΩ. (d) The equivalent circuit model of graphene electrodes. CPE stands for constant phase element simulating the Helmholtz double layer capacitance, CQ is the quantum capacitance, Rct is the charge transfer resistance, and WB is the bounded Warburg element simulating diffusion at the interface. (e) EIS measurements and the equivalent circuit model fitting of a representative graphene electrode channel are plotted. (f) The quantum capacitance, the Helmholtz double capacitance, and the total capacitance with respect to voltage are plotted. The quantum capacitance dominates the capacitive branch from -100 mV to 100 mV, which is the range of the open circuit potential of graphene.

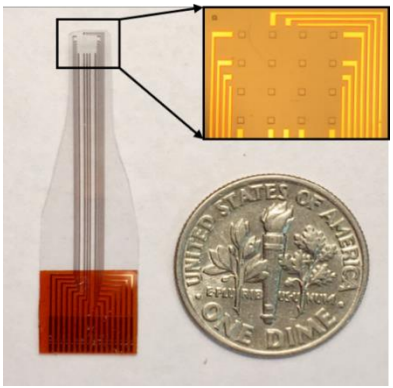

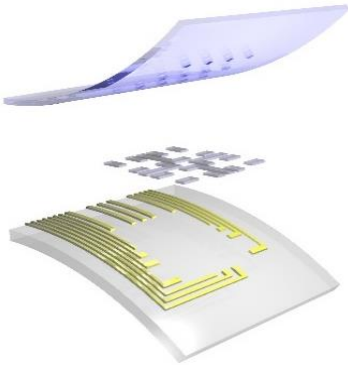

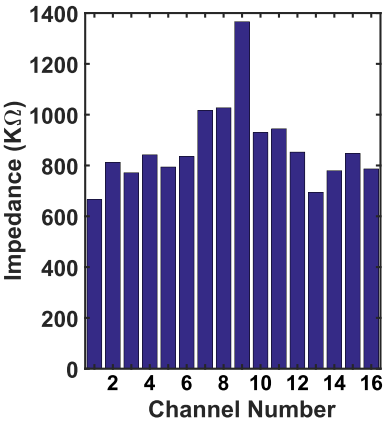
Impedance (KΩ)
Channel Number

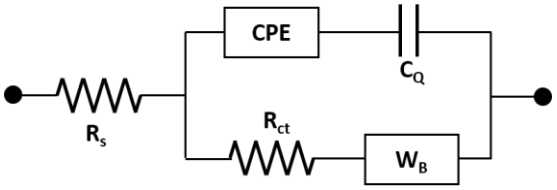
CPE
C_Q
R_s
R_{ct}
W_B

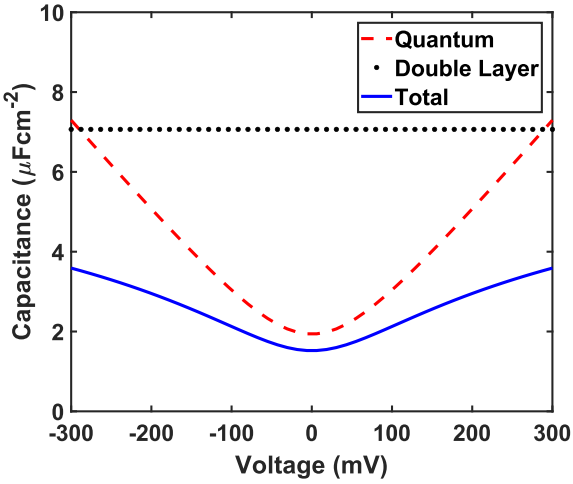
Quantum
Double Layer
Total
Capacitance (μFcm^{-2})
Voltage (mV)

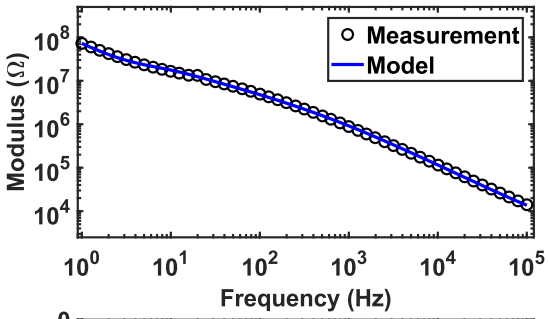
Measurement
Model
Modulus (Ω)
Frequency (Hz)

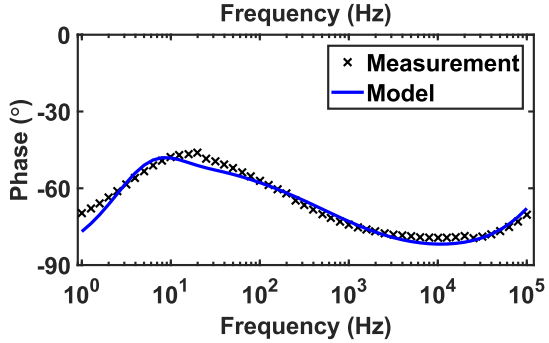
Measurement
Model
Phase (°)
Frequency (Hz)

Table 3. 1 Means and standard deviations (SD) of parameters in the equivalent circuit model.

	R_s [KΩ]	C_{dl} [μFcm^{-2}]	A	W [MΩ·s$^{-1/2}$]	B [s$^{1/2}$]	R_{ct} [MΩ]	C_Q [μFcm^{-2}]
Mean	4.32	7.07	0.924	158	0.333	1.62	2.45
SD	0.29	0.21	3.4×10^{-3}	2.0	3.7×10^{-4}	0.16	4.5×10^{-2}

Figure 3. 2 Scanning Electron Microscope Images of PtNPs on Graphene.

(a)-(c) show SEM images of PtNPs electrodeposited on graphene, the scale bar for these three panels is 1 μm. PtNPs cover 14.65%, 67.27%, and 88.22% of the graphene surface for 5, 20, 50 seconds depositions respectively. (d)-(e) show SEM images at a higher magnification to point out the size and shape of the PtNPs. The size of PtNP is less than 100 nm for 5 seconds deposition, 100-200 nm for 20 seconds, and above 250 nm for 50 seconds. Further, the surface roughness of the PtNPs also increases with deposition time.

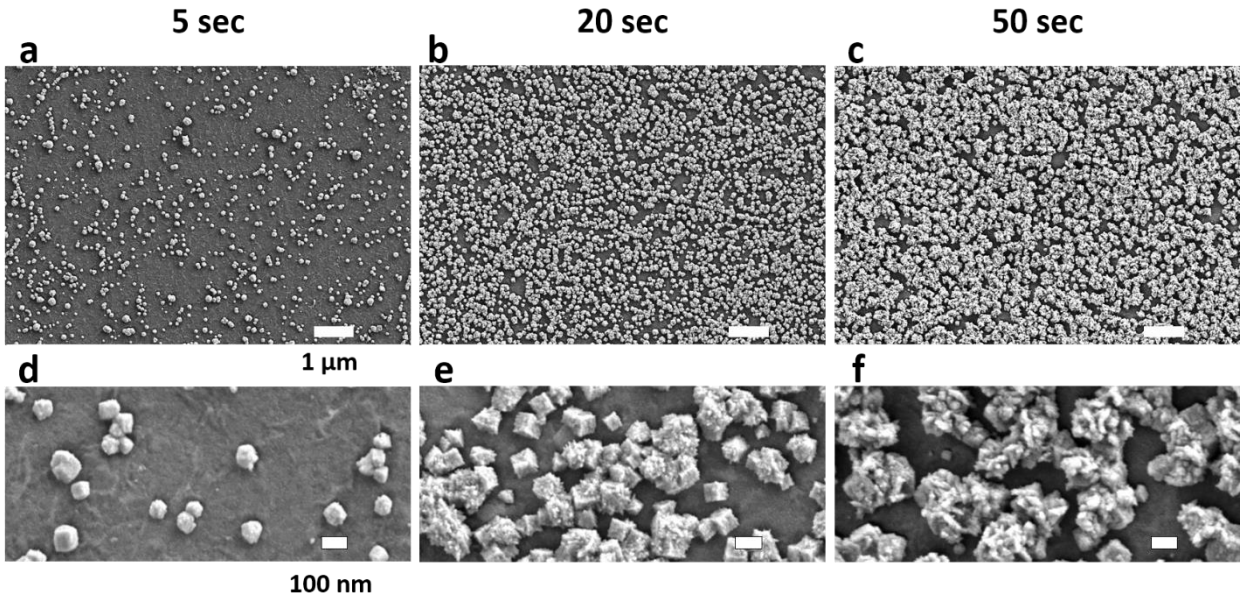
5 sec
20 sec
50 sec
a
b
c
1 µm
d
e
f
100 nm

Figure 3. 3 Characterization of PtNP/Graphene Electrodes.

(a) Electrochemical impedance spectroscopy of PtNP/Graphene electrodes from 1 Hz to 100 KHz. The black dots are the impedance of the original graphene electrode (without PtNPs), the impedance of a gold electrode (magenta) is also plot for comparison. (b) The Impedance at 1 KHz has a clear trend to decrease with deposition time. (c) Cyclic voltammetry of PtNP/Graphene electrodes with a sweep rate of 200 mV/s. Bare graphene electrode without PtNPs (black) has no faradaic peaks, and the current is very small, and hence the curve looks like a straight line. As the deposition time increase, Faradaic peaks become more obvious, and the current gets higher. (d) Transmittance spectra of PtNP/Graphene electrodes at wavelength from 450 to 850 nm.

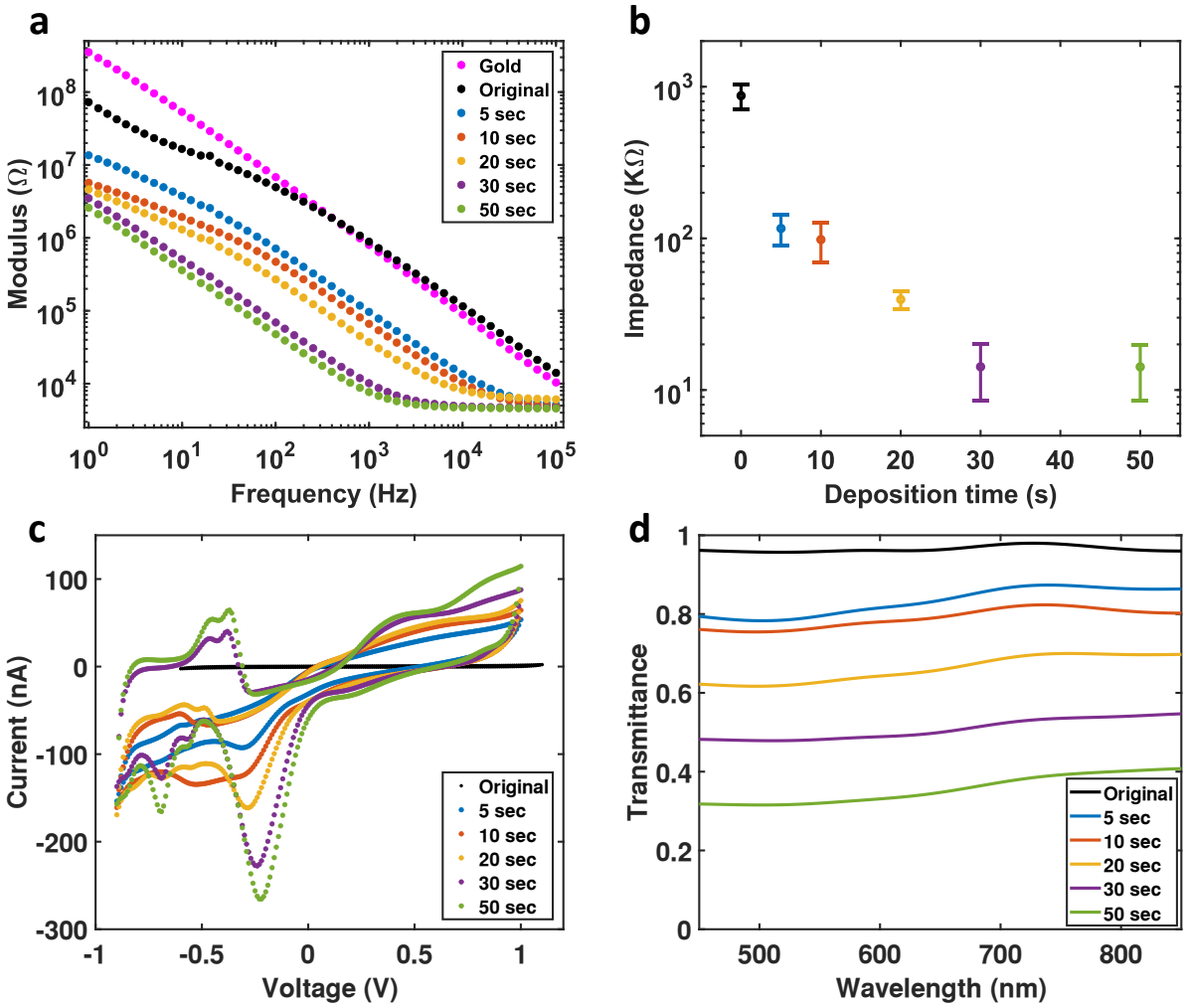
a
Modulus (Ω)
Frequency (Hz)
Gold
Original
5 sec
10 sec
20 sec
30 sec
50 sec
b
Impedance (KΩ)
Deposition time (s)
c
Current (nA)
Voltage (V)
Original
5 sec
10 sec
20 sec
30 sec
50 sec
d
Transmittance
Wavelength (nm)
Original
5 sec
10 sec
20 sec
30 sec
50 sec

Figure 3. 4 Circuit model fitting.

(a) Equivalent circuit model contains two blocks for graphene and PtNPs respectively. The parameters for the graphene block are fixed according to Table 1 and the coverage percentage according to SEM images. The PtNPs block and solution resistance (R_s) is obtained by fitting the measurement data to the circuit model. W_I, C_p, and CPE_{Pt} are the infinite Warburg element, pseudo-capacitance, and constant phase element for Pt double layer capacitor respectively. (b) Impedance of the graphene block (red dashed curve), Pt block (blue dashed curve) with respect to the total impedance of measurement (pink hollow circles) and fitting (black curve). The PtNPs block dominates the impedance over the graphene block at all frequencies. (c) This effect is more obvious for 50 seconds deposition, except at frequencies above 40 KHz, where solution resistance starts to dominate. (d) The fitted pseudo-capacitance of 50 seconds deposition with respect to the voltage bias shows at the pseudo-capacitance increases as the bias approaches hydrogen absorption region.

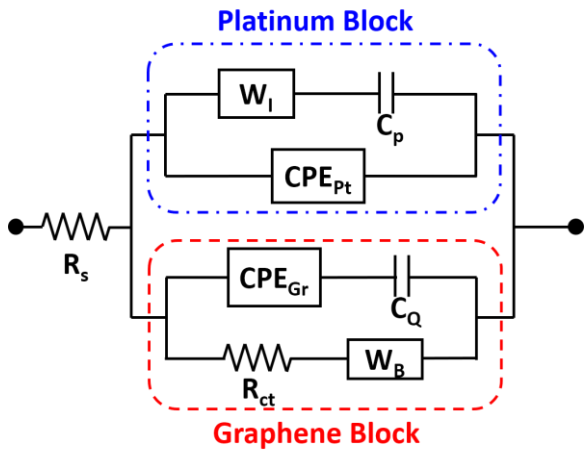
Platinum Block
W_I
C_p
CPE_Pt
R_s
CPE_Gr
C_Q
W_B
R_ct
Graphene Block

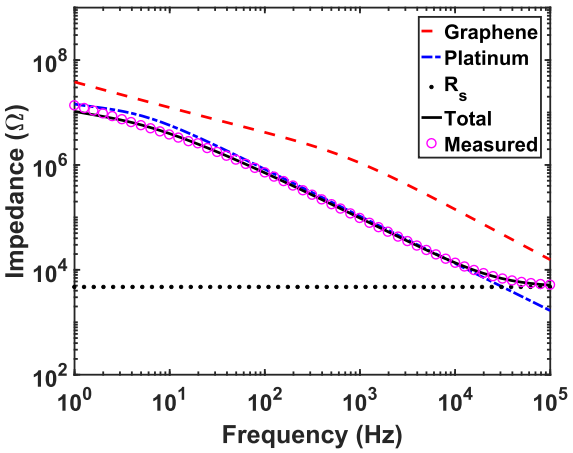
Graphene
Platinum
R_s
Total
Measured
Impedance (Ω)
Frequency (Hz)

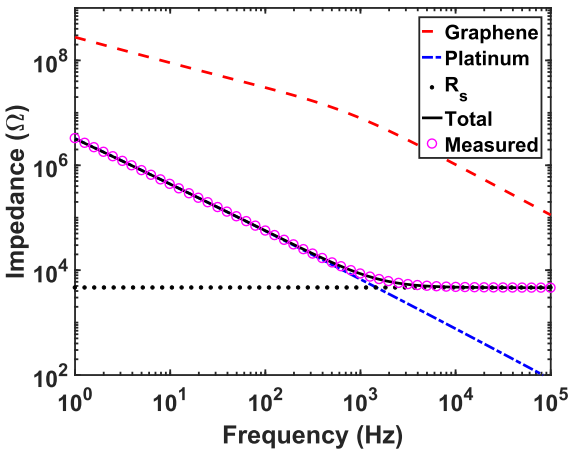
Graphene
Platinum
R_s
Total
Measured
Impedance (Ω)
Frequency (Hz)

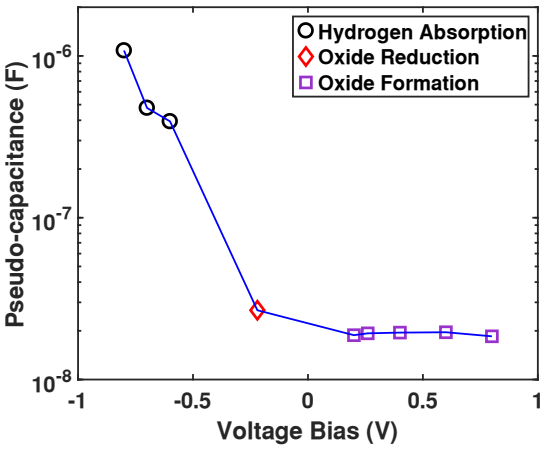
Hydrogen Absorption
Oxide Reduction
Oxide Formation
Pseudo-capacitance (F)
Voltage Bias (V)

Figure 3. 5 Simultaneous *in vivo* Calcium Imaging and ECoG Recording.

(a) The PtNP/graphene electrode array was placed on the cortex centered at 2.2 mm posterior and 2.1 mm lateral relative to bregma. (b) Two-photon microscope was focused at the depth of 250 μm from cortical surface to detect cell bodies, at the exact same location with 16x magnification. The deposition time for Electrode A, B, C, and D is 10, 50, 5, and 5 seconds respectively. (c) Multiple cells can be clearly imaged, Cell 1 and 2 are directly under the PtNP/graphene electrode, and Cell 3 and 4 outsides. The mean fluorescence change has a Region of Interest (ROI) the same as the electrode (white dashed box in Panel c). Fluorescence changes (d), ECoG trace and the spectrogram (e) were recorded and analyzed in a synchronized time frame. (f) The power ratio of ECoG oscillations at 50 μm calcium peak time is larger in lower frequency range (delta band) and smaller in higher frequency range (gamma and high gamma bands) than at 250um. (Kruskal-Wallis test, *** $p < 0.001$, * $p < 0.05$). (g) The power of the ECoG oscillations at each calcium peak time was calculated at delta band (δ, 1–4 Hz), theta band (θ, 4–8 Hz), alpha band (α, 9–12 Hz), beta band (β, 13–30 Hz), gamma band (γ, 30–100 Hz), and high gamma band (H-γ, >100 Hz).

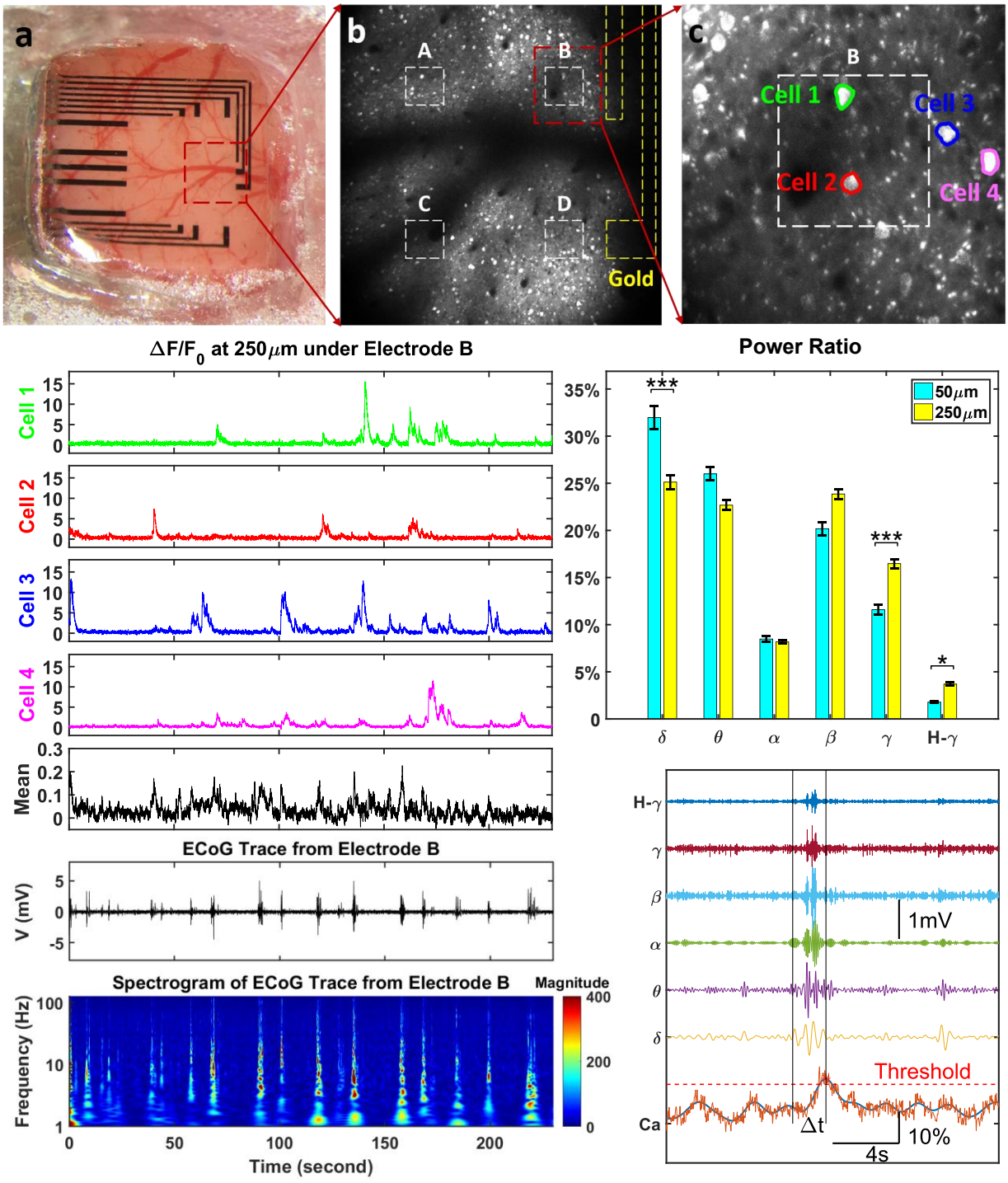
a
b
c
A
B
C
D
Gold
B
Cell 1
Cell 2
Cell 3
Cell 4
ΔF/F0 at 250μm under Electrode B
Cell 1
Cell 2
Cell 3
Cell 4
Mean
ECoG Trace from Electrode B
V (mV)
Spectrogram of ECoG Trace from Electrode B
Magnitude
Frequency (Hz)
Time (second)
Power Ratio
50μm
250μm
δ
θ
α
β
γ
H-γ
1mV
Threshold
Ca
Δt
10%
4s

3.8 Supplementary Information

Figure 3. S1 Fabrication flow.

(a) Fabrication starts with a 4-inch silicon wafer, fully cleansed and dehydrated. (b) Polydimethylsiloxane (PDMS) is spin-coated at 3000 rpm as the adhesive layer. (c) 50 μm thick polyethylene terephthalate (PET) substrate is placed on top to PDMS layer. (d) 10 nm chromium and 100 nm gold are sputtered on to PET substrate. (e) Metal wires are patterned with photolithography and wet-etching. (f) "Bubbling" method is adopted for graphene transfer. (g) Graphene pads are patterned with AZ1512/PMGI SF3 bilayer photolithography and oxygen plasma etching. (h) 8 μm thick SU-8 2005 encapsulated the array with square openings of 100 μm side length. (i) Peeled the off from the PDMS/Si wafer, the array is ready for electrochemical characterization.

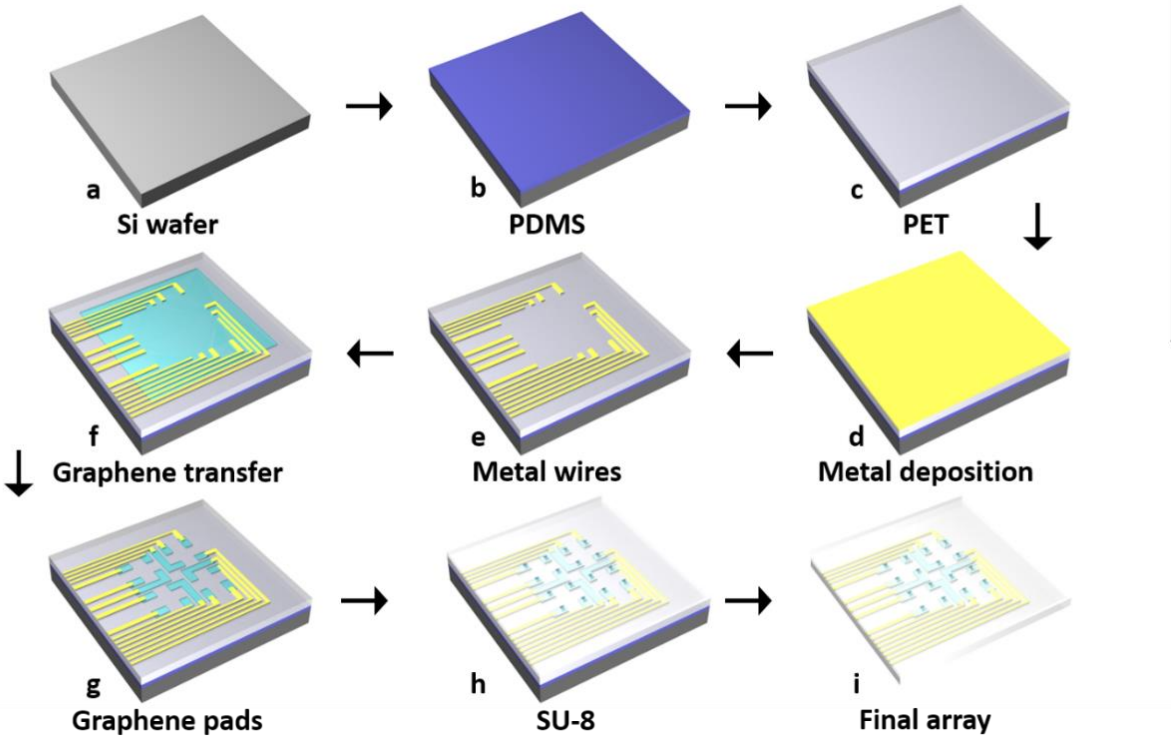
a
Si wafer
b
PDMS
c
PET
d
Metal deposition
e
Metal wires
f
Graphene transfer
g
Graphene pads
h
SU-8
i
Final array

Figure 3. S2 Scanning Electron Microscopy Images.

(a) The center-to-center spacing between two adjacent openings is 400 μm and the side length of the opening is 100 μm. (b) SU-8 encapsulation is well-defined by the photolithography process, there is no cracks in the SU-8 layer and no obvious polymer residual on the graphene surface.

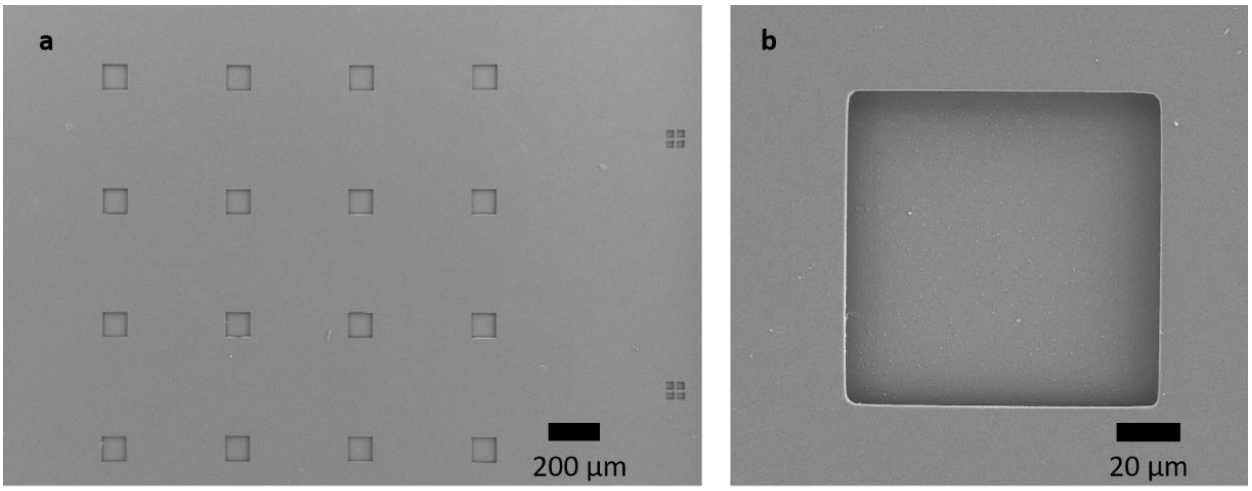
a
200 µm
b
20 µm

Figure 3. S3 Electrochemical Characterizations of Original Graphene Electrodes.

(a) Electrochemical impedance shows all 16 channels are working, with an average impedance of 872.9 KΩ at 1 KHz. The moduli and phases are shown in the top and bottom panel respectively. (b) Cyclic voltammetry of a representative channel shows no redox peaks, which is typical for graphene/solution interface. In comparison, CV of a gold channel has one peak at 0.7 V indicating redox reaction.

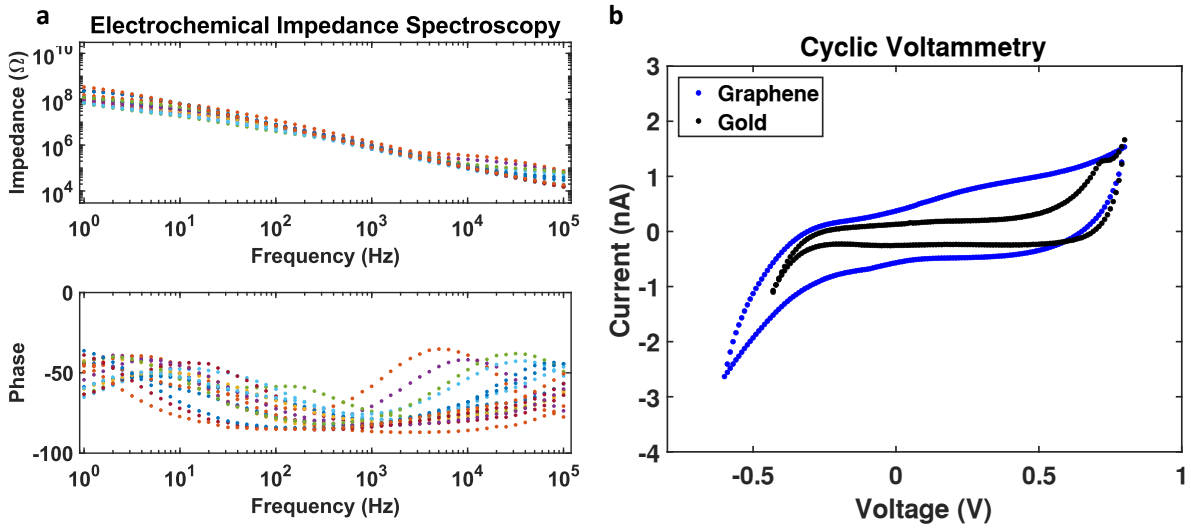
a
Electrochemical Impedance Spectroscopy
Impedance (Ω)
Frequency (Hz)
Phase
Frequency (Hz)
b
Cyclic Voltammetry
Graphene
Gold
Current (nA)
Voltage (V)

Figure 3. S4 Setup for PtNPs Electrodeposition.

The solution concentration is 1 mM H_2PtCl_6 and 10 mM K_2HPO_4, deionized water (R~18MΩ) is used as solvent so that no additional electrolyte is included. A two electrodes cell is constructed with Gamry 600 plus, where the graphene electrode is connected to the working/working sense and a platinum wire (0.5 mm diameter) to the counter/reference.

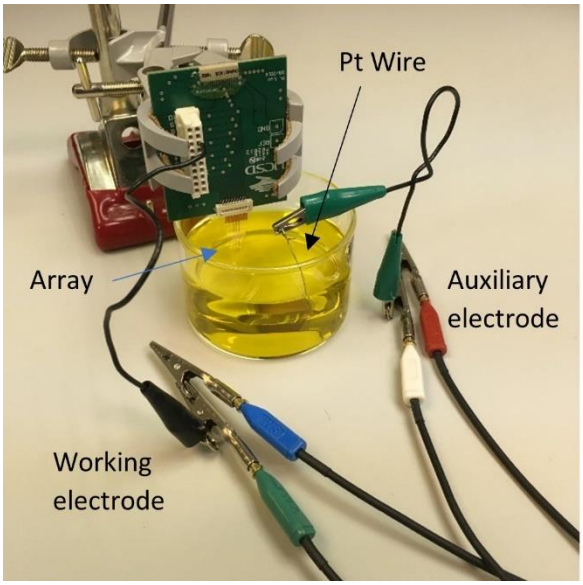
Pt Wire
Array
Auxiliary
electrode
Working
electrode

Figure 3. S5 PtNPs Coverage.

To estimate the PtNPs coverage, SEM images were loaded into MATLAB and converted to gray scale. A threshold mask was applied to all the pixel points so that most of the background graphene pixels were labeled correctly. Later, the morphological closing was performed to correctly label the “shadow” pixels on large PtNPs. The coverage is obtained by calculating the ratio of the PtNP pixel number and the total pixel number.

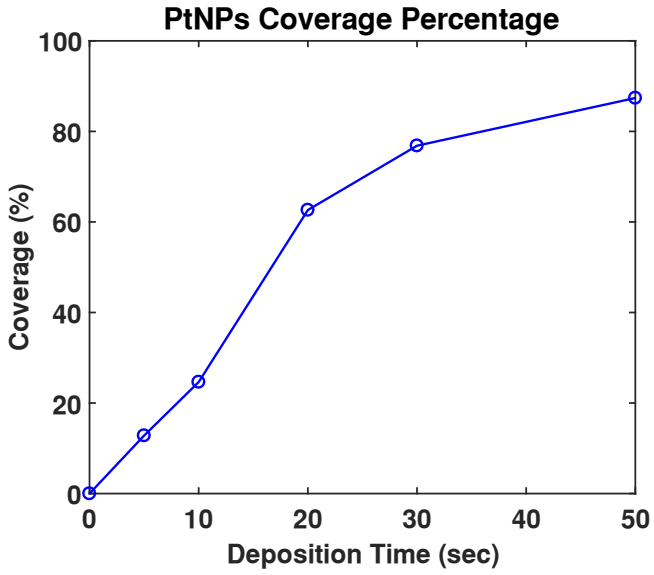
PtNPs Coverage Percentage
Coverage (%)
Deposition Time (sec)
0
20
40
60
80
100
0
10
20
30
40
50

Figure 3. S6 Nitric Acid Doping Effect.

16 pristine graphene channels have an average impedance of 1.43 MΩ. 16 channels doped with 35% nitric acid have average impedances of 872.9 KΩ. 70% nitric acid may decrease the impedance further, however, high concentrated nitric acid attacks polymers including PET and PMMA and hence makes transfer extremely difficult.

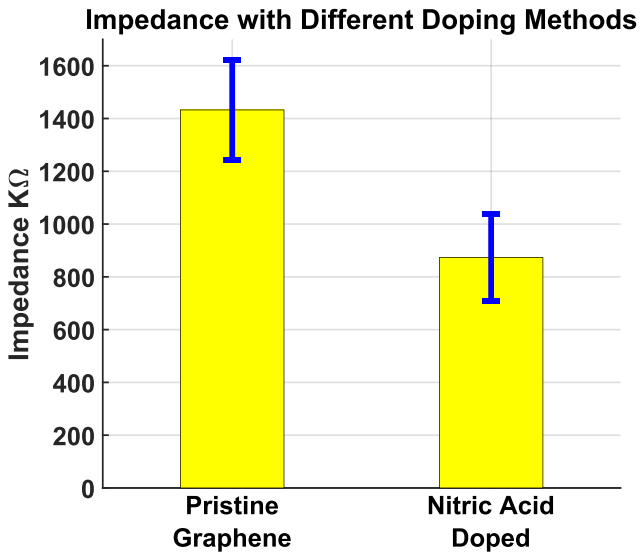
Impedance with Different Doping Methods
Impedance KΩ
1600
1400
1200
1000
800
600
400
200
0
Pristine Graphene
Nitric Acid Doped

Figure 3. S7 Two-photon *In Vivo* Calcium Imaging.

The top row is images focused at 250 μm deep, the bottom row at 50 μm. Two images in the same column have the exact same position, where SU-8 openings and gold wires are marked with white and golden dash lines respectively. The number under each electrode channel indicates the deposition time of PtNPs. At 250 μm, neuron activities can be clearly seen (light dots) unless blocked by blood vessels or gold wires.

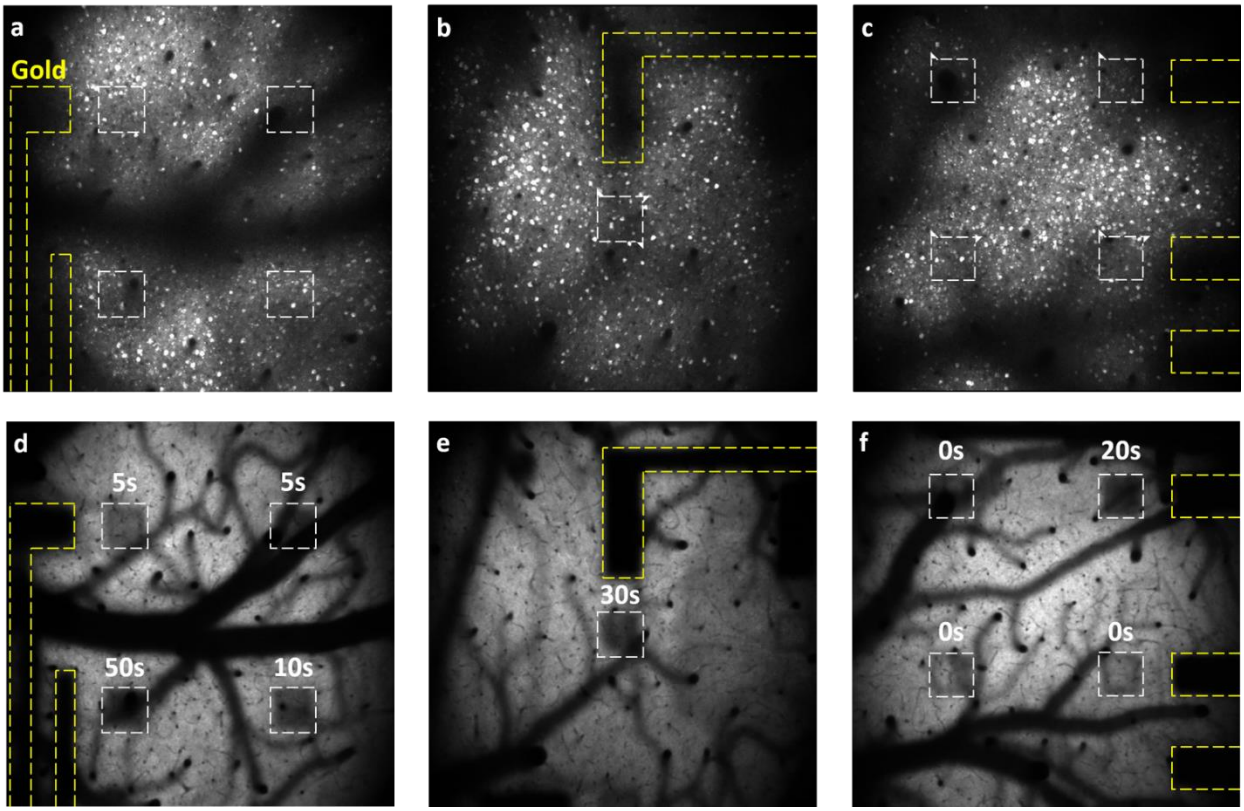
a
Gold
b
c
d
5s
5s
50s
10s
e
30s
f
0s
20s
0s
0s

Figure 3. S8 Electrical recordings from Electrode A, B, C, and D.

Electrical recordings from Electrode A, B, C, and D with deposition time of 10, 50, 5, and 5 seconds, respectively. The noise levels for these four electrode channels are similar to each other.

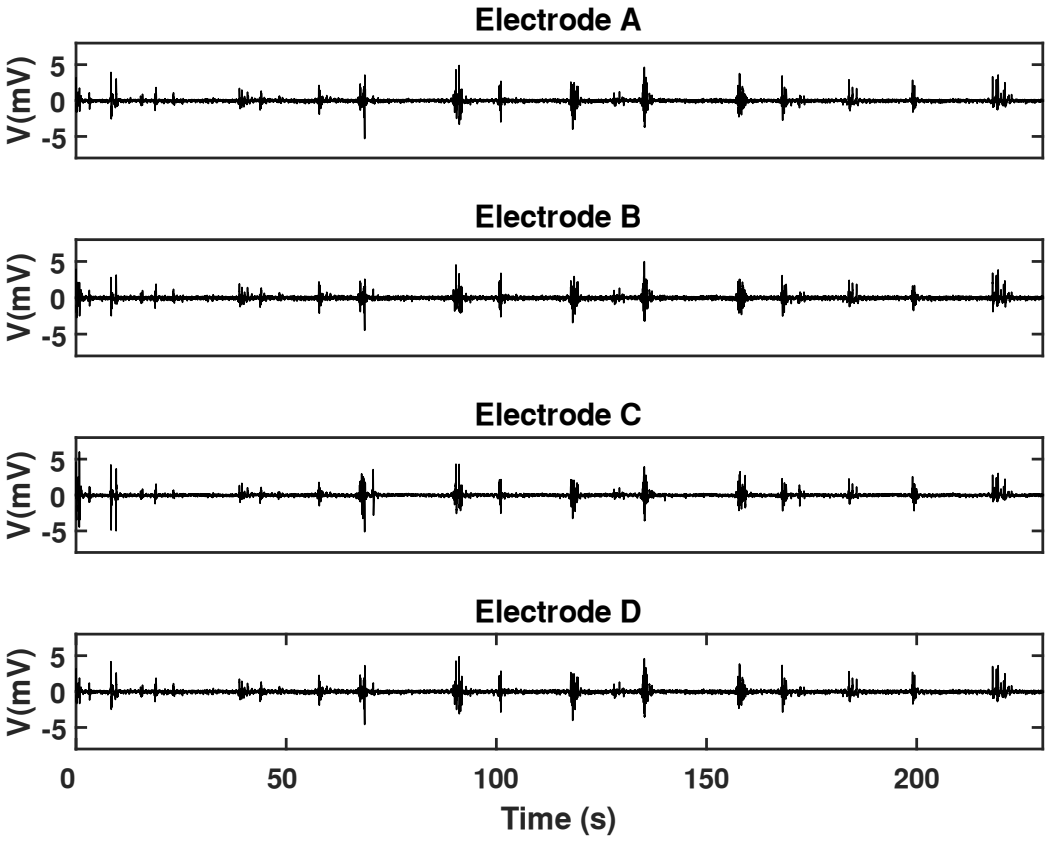
Electrode A
Electrode B
Electrode C
Electrode D
V(mV)
5
0
-5
0
50
100
150
200
Time (s)

Supplementary Note 3.S1 Equations for equivalent circuit models

Constant phase element:

$$Z_{CPE} = \frac{1}{(j\omega)^{A} C_{dl}}$$

Bounded Warburg element:

$$Z_{W_B} = \frac{W_B}{\sqrt{j\omega}} \tanh\left(\frac{\sqrt{j\omega}}{B}\right)$$

Infinite Warburg element:

$$Z_{W_I} = \frac{W_I(1-j)}{\sqrt{\omega}}$$

3.9 References

1 Buzsáki, G. Large-scale recording of neuronal ensembles. *Nature neuroscience* **7**, 446-451 (2004).

2 Buzsáki, G., Anastassiou, C. A. & Koch, C. The origin of extracellular fields and currents—EEG, ECoG, LFP and spikes. *Nature reviews neuroscience* **13**, 407-420 (2012).

3 Komiyama, T., Sato, T. R., O'Connor, D. H., Zhang, Y.-X., Huber, D., Hooks, B. M., Gabitto, M. & Svoboda, K. Learning-related fine-scale specificity imaged in motor cortex circuits of behaving mice. *Nature* **464**, 1182-1186 (2010).

4 Peters, A. J., Chen, S. X. & Komiyama, T. Emergence of reproducible spatiotemporal activity during motor learning. *Nature* **510**, 263-267 (2014).

5 Allalou, A., Wu, Y., Ghannad-Rezaie, M., Eimon, P. M. & Yanik, M. F. Automated deep-phenotyping of the vertebrate brain. *Elife* **6**, e23379 (2017).

6 Vallentin, D., Kosche, G., Lipkind, D. & Long, M. A. Inhibition protects acquired song segments during vocal learning in zebra finches. *Science* **351**, 267-271 (2016).

7 Badura, A., Sun, X. R., Giovannucci, A., Lynch, L. A. & Wang, S. S.-H. Fast calcium sensor proteins for monitoring neural activity. *Neurophotonics* **1**, 025008-025008 (2014).

8 Stosiek, C., Garaschuk, O., Holthoff, K. & Konnerth, A. In vivo two-photon calcium imaging of neuronal networks. *Proceedings of the National Academy of Sciences* **100**, 7319-7324 (2003).

9 Kuzum, D., Takano, H., Shim, E., Reed, J. C., Juul, H., Richardson, A. G., De Vries, J., Bink, H., Dichter, M. A. & Lucas, T. H. Transparent and flexible low noise graphene electrodes for simultaneous electrophysiology and neuroimaging. *Nature communications* **5**, 5259 (2014).

10 Park, D.-W., Schendel, A. A., Mikael, S., Brodnick, S. K., Richner, T. J., Ness, J. P., Hayat, M. R., Atry, F., Frye, S. T. & Pashaie, R. Graphene-based carbon-layered electrode array technology for neural imaging and optogenetic applications. *Nature communications* **5**, 1-11 (2014).

11 Kostarelos, K., Vincent, M., Hebert, C. & Garrido, J. A. Graphene in the Design and Engineering of Next - Generation Neural Interfaces. *Advanced Materials* **29**, 1700909 (2017).

12 Bae, M.-H., Li, Z., Aksamija, Z., Martin, P. N., Xiong, F., Ong, Z.-Y., Knezevic, I. & Pop, E. Ballistic to diffusive crossover of heat flow in graphene ribbons. *Nature communications* **4**, 1-7 (2013).

13 Wong, H.-S. P. & Akinwande, D. *Carbon nanotube and graphene device physics*. (Cambridge University Press, 2011).

14 Akinwande, D., Petrone, N. & Hone, J. Two-dimensional flexible nanoelectronics. *Nature communications* **5**, 1-12 (2014).

15 Tao, L., Lee, J., Chou, H., Holt, M., Ruoff, R. S. & Akinwande, D. Synthesis of high quality monolayer graphene at reduced temperature on hydrogen-enriched evaporated copper (111) films. *ACS nano* **6**, 2319-2325 (2012).

16 Lee, S., Sohn, J., Jiang, Z., Chen, H.-Y. & Wong, H.-S. P. Metal oxide-resistive memory using graphene-edge electrodes. *Nature communications* **6**, 1-7 (2015).

17 Grosse, K. L., Bae, M.-H., Lian, F., Pop, E. & King, W. P. Nanoscale Joule heating, Peltier cooling and current crowding at graphene–metal contacts. *Nature nanotechnology* **6**, 287-290 (2011).

18 Park, H. Y., Jung, W. S., Kang, D. H., Jeon, J., Yoo, G., Park, Y., Lee, J., Jang, Y. H., Lee, J. & Park, S. Extremely low contact resistance on graphene through n-Type doping and edge contact design. *Advanced Materials* **28**, 864-870 (2016).

19 Venkatesan, B. M., Estrada, D., Banerjee, S., Jin, X., Dorgan, V. E., Bae, M.-H., Aluru, N. R., Pop, E. & Bashir, R. Stacked graphene-Al2O3 nanopore sensors for sensitive detection of DNA and DNA–protein complexes. *ACS nano* **6**, 441-450 (2012).

20 Schedin, F., Geim, A. K., Morozov, S. V., Hill, E., Blake, P., Katsnelson, M. & Novoselov, K. S. Detection of individual gas molecules adsorbed on graphene. *Nature materials* **6**, 652-655 (2007).

21 D'Arsié, L., Esconjauregui, S., Weatherup, R. S., Wu, X., Arter, W. E., Sugime, H., Cepek, C. & Robertson, J. Stable, efficient p-type doping of graphene by nitric acid. *RSC Advances* **6**, 113185-113192 (2016).

22 Kasry, A., Kuroda, M. A., Martyna, G. J., Tulevski, G. S. & Bol, A. A. Chemical doping of large-area stacked graphene films for use as transparent, conducting electrodes. *ACS nano* **4**, 3839-3844 (2010).

23 Ledochowitsch, P., Olivero, E., Blanche, T. & Maharbiz, M. M. in *2011 Annual International Conference of the IEEE Engineering in Medicine and Biology Society.* 2937-2940 (IEEE).

24 Kwon, K. Y., Sirowatka, B., Weber, A. & Li, W. Opto-μECoG array: A hybrid neural interface with transparent μECoG electrode array and integrated LEDs for optogenetics. *IEEE transactions on biomedical circuits and systems* **7**, 593-600 (2013).

25 Fang, T., Konar, A., Xing, H. & Jena, D. Carrier statistics and quantum capacitance of graphene sheets and ribbons. *Applied Physics Letters* **91**, 092109 (2007).

26 Wang, Y., Zheng, Y., Xu, X., Dubuisson, E., Bao, Q., Lu, J. & Loh, K. P. Electrochemical delamination of CVD-grown graphene film: toward the recyclable use of copper catalyst. *ACS nano* **5**, 9927-9933 (2011).

27 Franks, W., Schenker, I., Schmutz, P. & Hierlemann, A. Impedance characterization and modeling of electrodes for biomedical applications. *IEEE Transactions on Biomedical Engineering* **52**, 1295-1302 (2005).

28 Hassibi, A., Navid, R., Dutton, R. W. & Lee, T. H. Comprehensive study of noise processes in electrode electrolyte interfaces. *Journal of applied physics* **96**, 1074-1082 (2004).

29 Uesugi, E., Goto, H., Eguchi, R., Fujiwara, A. & Kubozono, Y. Electric double-layer capacitance between an ionic liquid and few-layer graphene. *Scientific reports* **3**, 1595 (2013).

30 Ji, H., Zhao, X., Qiao, Z., Jung, J., Zhu, Y., Lu, Y., Zhang, L. L., MacDonald, A. H. & Ruoff, R. S. Capacitance of carbon-based electrical double-layer capacitors. *Nature communications* **5**, 3317 (2014).

31 Xia, J., Chen, F., Li, J. & Tao, N. Measurement of the quantum capacitance of graphene. *Nature nanotechnology* **4**, 505-509 (2009).

32 Zhan, C., Neal, J., Wu, J. & Jiang, D.-e. Quantum effects on the capacitance of graphene-based electrodes. *The Journal of Physical Chemistry C* **119**, 22297-22303 (2015).

33 Zhou, Y.-G., Chen, J.-J., Wang, F.-b., Sheng, Z.-H. & Xia, X.-H. A facile approach to the synthesis of highly electroactive Pt nanoparticles on graphene as an anode catalyst for direct methanol fuel cells. *Chemical Communications* **46**, 5951-5953 (2010).

34 Hu, Y., Zhang, H., Wu, P., Zhang, H., Zhou, B. & Cai, C. Bimetallic Pt–Au nanocatalysts electrochemically deposited on graphene and their electrocatalytic characteristics towards oxygen reduction and methanol oxidation. *Physical Chemistry Chemical Physics* **13**, 4083-4094 (2011).

35 Li, Y., Gao, W., Ci, L., Wang, C. & Ajayan, P. M. Catalytic performance of Pt nanoparticles on reduced graphene oxide for methanol electro-oxidation. *Carbon* **48**, 1124-1130 (2010).

36 Wu, H., Wang, J., Kang, X., Wang, C., Wang, D., Liu, J., Aksay, I. A. & Lin, Y. Glucose biosensor based on immobilization of glucose oxidase in platinum nanoparticles/graphene/chitosan nanocomposite film. *Talanta* **80**, 403-406 (2009).

37 Zhang, D., Chang, W. C., Okajima, T. & Ohsaka, T. Electrodeposition of platinum nanoparticles in a room-temperature ionic liquid. *Langmuir* **27**, 14662-14668 (2011).

38 Singal, S., Biradar, A. & Mulchandani, A. Ultrasensitive electrochemical immunosensor based on Pt nanoparticle–graphene composite. *Applied biochemistry and biotechnology* **174**, 971-983 (2014).

39 Hudak, E. M., Kumsa, D. W., Martin, H. B. & Mortimer, J. T. Electron transfer processes occurring on platinum neural stimulating electrodes: calculated charge-storage capacities are inaccessible during applied stimulation. *Journal of neural engineering* **14**, 046012 (2017).

40 Daubinger, P., Kieninger, J., Unmüssig, T. & Urban, G. A. Electrochemical characteristics of nanostructured platinum electrodes–a cyclic voltammetry study. *Physical Chemistry Chemical Physics* **16**, 8392-8399 (2014).

41 Yoo, H. D., Jang, J. H., Ka, B. H., Rhee, C. K. & Oh, S. M. Impedance analysis for hydrogen adsorption pseudocapacitance and electrochemically active surface area of Pt electrode. *Langmuir* **25**, 11947-11954 (2009).

42 Merrill, D. R., Bikson, M. & Jefferys, J. G. Electrical stimulation of excitable tissue: design of efficacious and safe protocols. *Journal of neuroscience methods* **141**, 171-198 (2005).

43 Mayford, M., Bach, M. E., Huang, Y.-Y., Wang, L., Hawkins, R. D. & Kandel, E. R. Control of memory formation through regulated expression of a CaMKII transgene. *Science* **274**, 1678-1683 (1996).

44 Wekselblatt, J. B., Flister, E. D., Piscopo, D. M. & Niell, C. M. Large-scale imaging of cortical dynamics during sensory perception and behavior. *Journal of neurophysiology* (2016).

45 Makino, H., Ren, C., Liu, H., Kim, A. N., Kondapaneni, N., Liu, X., Kuzum, D. & Komiyama, T. Transformation of Cortex-wide Emergent Properties during Motor Learning. *Neuron* **94**, 880-890. e888 (2017).

46 Makino, H. & Komiyama, T. Learning enhances the relative impact of top-down processing in the visual cortex. *Nature neuroscience* **18**, 1116-1122 (2015).

47 Her, M., Beams, R. & Novotny, L. Graphene transfer with reduced residue. *Physics Letters A* **377**, 1455-1458 (2013).

48 Wood, J. D., Doidge, G. P., Carrion, E. A., Koepke, J. C., Kaitz, J. A., Datye, I., Behnam, A., Hewaparakrama, J., Aruin, B. & Chen, Y. Annealing free, clean graphene transfer using alternative polymer scaffolds. *Nanotechnology* **26**, 055302 (2015).

49 Matsumae, T., Koehler, A. D., Suga, T. & Hobart, K. D. A Scalable Clean Graphene Transfer Process Using Polymethylglutarimide as a Support Scaffold. *Journal of The Electrochemical Society* **163**, E159 (2016).

50 Lin, Y.-C., Lu, C.-C., Yeh, C.-H., Jin, C., Suenaga, K. & Chiu, P.-W. Graphene annealing: how clean can it be? *Nano letters* **12**, 414-419 (2012).

51 Pirkle, A., Chan, J., Venugopal, A., Hinojos, D., Magnuson, C., McDonnell, S., Colombo, L., Vogel, E., Ruoff, R. & Wallace, R. The effect of chemical residues on the physical and electrical properties of chemical vapor deposited graphene transferred to SiO2. *Applied Physics Letters* **99**, 122108 (2011).

52 Chen, T.-W., Wardill, T. J., Sun, Y., Pulver, S. R., Renninger, S. L., Baohan, A., Schreiter, E. R., Kerr, R. A., Orger, M. B. & Jayaraman, V. Ultrasensitive fluorescent proteins for imaging neuronal activity. *Nature* **499**, 295-300 (2013).

53 Pachitariu, M., Stringer, C., Dipoppa, M., Schröder, S., Rossi, L. F., Dalgleish, H., Carandini, M. & Harris, K. D. Suite2p: beyond 10,000 neurons with standard two-photon microscopy. *Biorxiv* (2017).

Chapter 4. Multimodal neural recordings with Neuro-FITM uncover diverse patterns of cortical-hippocampal interactions

4.1 Abstract

Many cognitive processes require communication between neocortex and hippocampus. However, coordinations between large-scale cortical dynamics and hippocampal activity are not well-understood, partially due to the difficulty to simultaneously record from those regions. Here we developed a Flexible, Insertable, and Transparent Microelectrode array ('Neuro-FITM') that enables investigation of cortical-hippocampal coordinations during hippocampal sharp-wave ripples (SWRs). Flexibility and transparency of Neuro-FITM allow simultaneous recordings of local field potentials and neural spiking from hippocampus during wide-field calcium imaging. These experiments revealed that diverse cortical activity patterns accompanied SWRs, and in most cases, cortical activation preceded hippocampal SWRs. We demonstrated that, during SWRs, different hippocampal neural population activity was associated with distinct cortical activity patterns. These results suggest that hippocampus and large-scale cortical activity interact in a selective and diverse manner during SWRs underlying various cognitive functions. Our technology can be broadly applied to comprehensive investigations of interactions between cortex and other subcortical structures.

4.2 Introduction

Brain computations often require interactions between different cortical and subcortical structures. Understanding these long-range interactions in the brain requires monitoring of simultaneous activity patterns across these areas. That could be achieved by simultaneous multimodal recordings combining electrophysiological recordings and large-scale functional

optical imaging. However, seamless integration of optical imaging with electrophysiology is difficult with conventional microelectrodes since large probe shanks made of rigid and opaque materials can prevent lowering the microscope objective and block the field of view of imaging. To address this issue, we developed 'Neuro-FITM', a Flexible, Insertable, and Transparent Microelectrode array which can be implanted into deep cortical layers and subcortical structures. The flexible probe shank of Neuro-FITM can be bent to the side to allow lowering the microscope objective. Optical transparency of the shank provides a clear field of view and prevents optical shadows or additional noise in optical signals. Low impedance of Neuro-FITM provides reliable recordings of local field potentials (LFPs), high frequency oscillations and single units with high signal-to-noise ratio (SNR).

Here we performed multimodal experiments with Neuro-FITM to investigate the coupling between the hippocampus and the cortex during sharp wave-ripples (SWRs). Hippocampal SWRs have been suggested to coordinate activity between the hippocampus and cortex [1-4]. Experiments with closed-loop manipulations have shown the indispensable role of SWRs in learning and memory [5-7]. However, most studies only focused on a single or a few cortical regions [8-12] and thus little is known about the simultaneous interaction between multiple cortical regions and hippocampus during SWRs. Furthermore, it is unclear whether the cortex is passively activated by hippocampal SWRs or whether certain cortical activity patterns can precede SWRs. Importantly, simultaneous variations across SWRs in hippocampal population activity and cortical activity patterns have not been studied. These questions could be addressed by simultaneous multimodal recordings that include electrophysiological recordings of the hippocampus and functional imaging of the cortex across large areas. We implanted Neuro-FITM to the hippocampus and performed simultaneous electrophysiological recordings of SWRs and single

units during wide-field calcium imaging of most of the dorsal cortex in awake, head-fixed mice. Empowered by the multimodal recording capability, we investigated the large-scale cortical activity patterns associated with SWRs on single-event basis using tensor component analysis (TCA) [13] and found a rich spatiotemporal diversity. Furthermore, by performing decoding analysis with support vector machine (SVM) [14], we found that different cortical activity patterns relate to distinct activity of hippocampal neurons. Our results reveal that SWRs accompany diverse and specific interactions between the activity of hippocampus and cortex and support the model that SWRs mediate diverse cortical-hippocampal interactions depending on the behavioral context and demand.

4.3 Results

4.3.1 Neuro-FITM Fabrication and Characterization

Neuro-FITM arrays developed in this study combine three key advantages: flexibility, transparency and shuttle-free implantation in a single probe. They were fabricated on transparent and flexible Parylene-C substrate (Figure 4.1a-c). Briefly; PMGI sacrificial layer was spin-coated on a silicon wafer. A 14 μm-thick Parylene-C layer was deposited with the chemical-vapor-deposition (CVD) method. 5 nm Cr and 100 nm Au were deposited with sputtering and patterned with photo-lithography and wet-etching. 2 μm-thick Parylene-C was deposited as the encapsulation layer (Figure 4.1c). Electrode openings were patterned with photo-lithography and oxygen plasma etching. The profile of the probe was defined with photo-lithography and oxygen reactive ion etching (Figure 4.1d-f). Neuro-FITM arrays can be fabricated in various configurations depending on specific needs of the experiments. Neuro-FITM probe shown in Figure 4.1 is designed to record hippocampal LFPs and units during optical imaging. The width of the array is 50 μm at the tip, whereas the shank is tapered up to a maximum width of 170 μm at

the top. The array consists of 32 circular recording electrodes, each with 10 μm diameter connected to 2 μm-wide wires. The scanning electron microscope (SEM) images show the profile of the probe and well-defined electrode openings (Figure 4.1d-f). We fabricated several different configurations of Neuro-FITM including probes with smaller electrode spacing (20 μm) for potential use in tetrode configuration (Figure 4.S1a), probes with higher channel count (64 channels per shank) (Figure 4.S1b), and probes with longer shanks to allow recording from deeper structures of the brain or to use in rats (Figure 4.S1c) and primates (Figure 4.S1d).

Reducing the electrode impedance is important to minimize the electrical noise, particularly for single unit recordings [15-17]. To achieve low impedance, platinum nanoparticles (PtNPs) were deposited onto 10 μm Au electrodes of Neuro-FITM probes (Figure 4.1g-i) [17]. The electrode impedance can be controlled as a function of PtNP deposition time (Figure 4.1j) and the size of the PtNP increases as the deposition time increases [17]. The largest grains of PtNPs are about 500 nm in diameter for 180 s deposition time. Electrochemical impedance spectroscopy (EIS) results show that the impedance of the Neuro-FITM electrodes was reduced by ~16x (Figure 4.1k) as a result of PtNP deposition. Cyclic voltammetry (CV) measurements confirm that the PtNPs are actively engaged in the redox processes at the electrochemical interface (Figure 4.1l). The impedance of our 10 μm diameter electrodes is ~150 kΩ at 1 kHz, similar to those of the Neuropixel probes (~150 kΩ) [18] even though the surface area (78.5 μm^2) is half the size (Neuropixel = 144 μm^2). Considering the impedance is inversely proportional to the electrode area, the impedance of Neuro-FITM electrodes is effectively 2 times smaller than the Neuropixel probes. We investigated the effect of impedance reduction on recording noise. Figure 4.1m shows recorded electrical noise as a function of electrode impedance, varied by controlling PtNP deposition time.

Neuro-FITM electrodes exhibit sufficiently low noise (10 μV) for reliable detection and sorting of single units.

Optical transparency is important for seamless integration of electrophysiological recordings and optical imaging in multimodal experiments [16,19]. We characterized the optical transparency of Neuro-FITM. The transmittance of the bent shank is ~95.7% and the recording tip with dense Au electrodes and interconnects shows a transmittance of ~50% (Figure 4.1n). It is important to point out that although the Au electrodes and Au wires are not transparent, the functional imaging would not be affected since 1) Neuro-FITM is vertically implanted so that the penetrating tip of the probe does not directly block the light pathway, and 2) the bent shank in the light pathway has thin Au wires resulting in a high transmittance of ~95.7%. In order to better clarify the advantages of Neuro-FITM in multimodal configurations involving two-photon microscopy or wide-field imaging, we compared Neuro-FITM to commercially available Neuronexus and Neuropixel probes (Figure 4.S2). The high flexibility of Neuro-FITM allows bending the probe shank away to lower the microscope objective for two-photon imaging (Figure 4.S2b), while rigid shanks of the Neuropixel and Neuronexus probes prevent lowering the microscope objective to its working distance. Wide-field microscope images (Figure 4.S2c) show that Neuronexus and Neuropixel probes block the field of view and generate shadows. In addition, large probe shanks can also result in out-of-focus images (Figure 4.S2c, Neuropixel probe). Transparency of Neuro-FITM prevents blocking the field of view and the formation of optical shadows which can obscure imaging. In addition to multiphoton imaging and wide-field imaging, Neuro-FITM array is also compatible with other optical imaging techniques commonly used in neuroscience, including near-infrared spectroscopy, and diffuse optical tomography.

4.3.2 In vivo Multimodal Recordings with Neuro-FITM

Vertical implantation of Neuro-FITM arrays is critical for not blocking the light pathway during optical imaging and minimizing implantation damage. In order to implant Neuro-FITM arrays vertically without using a rigid shuttle or adding a bioresorbable stiffening layer, we carefully engineered the geometry and the length of the microelectrode array by performing mechanical analysis to prevent buckling during insertion. Furthermore, the probe was designed to include additional micromanipulator pads to maximize insertion force against buckling (Figure 4.2a, see Methods). Note that, implantation of Neuro-FITM arrays with very long probe lengths designed for primate use (Figure 4.1d) will require the aid of shuttles during the insertion step. After the insertion and successful targeting of hippocampus (Figure 4.2b), the shank of the array was bent away to the side to allow lowering the microscope objective to its working distance and to clear the field of view of the microscope (Figure 4.2a, and Figure 4.S3a). 2 μm-wide wires are confined to a narrow width to increase transparency of the shank and to minimize formation of shadows during imaging (Figure 4.2c). In order to investigate the use of Neuro-FITM in *in vivo* multimodal experiments, we implanted it into the CA1 layer of hippocampus (Figure 4.2b, Figure 4.S3b) of transgenic mice expressing GCaMP6s in most cortical excitatory neurons [20] (CaMK2-tTA::tetO-GCaMP6s, methods). We performed simultaneous electrophysiological recordings of CA1 and wide-field calcium imaging of the dorsal cortex [21]. Hippocampal SWRs were detected in multiple channels located near the CA1 pyramidal layer (Figure 4.2d) with concurrent large-scale cortical dynamics monitored using wide-field calcium imaging. Figure 4.2e shows representative examples of various spatial patterns of cortical activation during individual SWRs. In addition to recordings of high frequency SWR events, Neuro-FITM electrodes also detected spikes from multiple hippocampal neurons (12 ± 2 (mean ± s.e.m.) neurons in each animal). Most neurons could be detected in multiple adjacent channels, each exhibiting different spike amplitudes

(Figure 4.S3c). Figure 4.3a shows spike waveforms of 21 neurons recorded across different channels in three recording sessions from one animal. Figure 4.3b shows the spike waveforms of all 21 neurons from the channel with largest amplitude. Recorded neurons show stable spike waveforms across the sessions. Signal-to-noise ratio of the electrical recordings is critical for spike detection and sorting as well as reliable detection of SWRs across different sessions. Therefore, we investigated SNR for both unit (Figure 4.4a) and LFP recordings adopting the method used for measuring spike SNR of Neuropixel probes [18]. The SNR is computed as A/(0.6457×B), where A is the maximum signal amplitude and B is the baseline taken as the median absolute deviation (MAD). The mean SNR of detected spikes is between 6 and 15 (Figure 4.4b), similar to the SNR recorded by Neuropixel and other Si probes [18,22]. To quantify the SNR of the LFP recordings, we measured the SNR for ripples and sharp-wave events using the same method [18]. The LFP signals recorded from the channels located in the pyramidal layer were band-pass filtered at the ripple frequency range (120 Hz – 250 Hz) and sharp-wave frequency range (5 Hz – 50 Hz) respectively. The baseline was then chosen as MAD of the filtered signal from each channel. For each ripple event, the maximum signal amplitude is taken. The distribution of the detected amplitude and the SNR for ripples and sharp-waves are shown in Figure 4.4c, d and Figure 4.4e, f, respectively. These results confirm that Neuro-FITM achieves high SNR for both single-unit and LFP recordings in all animals. Another important question is how SNR of fluorescence response in wide-field imaging would be affected by the presence of Neuro-FITM electrodes. We characterized the SNR of the ΔF/F to quantify whether the implanted array affects imaging quality following the procedure in a previous study [23]. Briefly, we first identified the onset and offset time points of each cortical activation events. The SNR of each event is computed as the ratio between the maximum ΔF/F amplitude during activation and the standard deviation of the ΔF/F

fluctuation during [-1s, 0s] before onset. We found similar SNR for the fluorescence activity from the area covered by Neuro-FITM shank and the corresponding area in the contralateral hemisphere (Figure 4.4g), showing that Neuro-FITM does not significantly change the SNR of fluorescence signals during wide-field calcium imaging.

4.3.3 Cortical activation onset tends to precede hippocampal SWRs

Our multimodal recording setup with Neuro-FITM provides an ideal platform to investigate the spatiotemporal properties of cortical-hippocampal interactions during SWRs. We first examined the large-scale cortical activity patterns averaged across all SWRs. To analyze the onsets of cortical activity and SWR accurately without contamination from prior SWR events, we focused on SWRs that did not have other SWRs for at least the preceding 3 s (4290 'well-separated SWRs' out of 8643 SWRs). We found that the onset of cortical activation averaged across SWRs preceded SWR onset by 1.33 ± 0.15 s (mean ± s.d., Figure 4.5a, Figure 4.4a) while the peak of cortical activation occurred 0.67 ± 0.18 s (mean ± s.d.) after the SWR onset. To investigate whether different cortical regions have different activation timing relative to SWR onset, we parcellated the dorsal cortex into 16 individual regions based on Allen Brain Atlas (Figure 4.5b) and examined the activity of each cortical region around SWR onset. On average all the cortical regions increased their activity around SWRs (Figure 4.5c, Figure 4.S4b). Furthermore, the activation onset timing of cortical regions relative to the SWR onset exhibited an anterior-posterior gradient, with the earlier activation of posterior cortical regions such as visual cortex, retrosplenial cortex, and posterior parietal cortex (Figure 4.5d, Figure 4.S5). Similarly, the fraction of SWR events with the activation of the cortical region leading SWR onset increased from anterior to posterior cortical regions (Figure 4.5e). 93.78 % of SWRs had at least one cortical region whose activity onset

preceded the SWR onset. Taken together, in a majority of SWR events, the cortical activation started before hippocampal SWRs, especially in posterior cortical regions.

4.3.4 Distinct patterns of cortical activity around SWRs

Given that multimodal recordings with Neuro-FITM showed spatiotemporal variations in cortical activity from SWR events to SWR events (Figure 4.2e), we next asked whether there were distinct cortical activation patterns that were reproducibly observed across subsets of the SWRs. Simultaneous wide-field imaging of the dorsal cortex and SWR recordings from hippocampus with Neuro-FITM across many sessions generated large-scale neural datasets that can be analyzed to answer this question. To that end, we performed a two-stage tensor component analysis (TCA) [13] on the activity from all the recorded cortical regions during all SWR events, including well-separated and non-well-separated SWRs. TCA is an unsupervised dimensionality reduction method that extracts recurring patterns in high-dimensional data (Figure 4.S6) by decomposing the data into 3 factors (Figure 4.6a). The region factors and time factors describe the spatial and temporal dynamics of cortical patterns respectively, and the event factors measure the weighting of a given SWR event on the established set of patterns. By multiplying the region factors and time factors, we identified 8 distinct cortical activity pattern templates that were common across all animals (Figure 4.6b, Figure 4.S7a). The patterns exhibited distinct activated regions focusing on either the anterior or the posterior cortices, with patterns 1, 2, and 3 dominated by anterior regions (‘anterior patterns’) and patterns 4, 5, and 6 dominated by posterior regions (‘posterior patterns’) with different time courses relative to the SWR onset. Besides patterns 1-6 showing transient and spatially-discrete activity patterns, pattern 7 was dominated by an extended activation in visual cortex and pattern 8 showed periodic and oscillatory activation in all cortical regions. The cortical

activity pattern in each SWR event could be well reconstructed as a linear sum of the 8 templates weighted by the event factors (Figure 4.S6b).

To explore the diversity of SWR-associated cortical activity, we first measured the 2D correlation between the cortical activity during individual well-separated SWR events and each of the cortical pattern templates. The correlations for SWR events followed a continuous distribution instead of aggregating into isolated clusters (Figure 4.6c), indicating that broadly distributed diverse cortical activity patterns were associated with SWRs. To examine the SWR events with divergent associated cortical activity, we next focused our analysis on groups of SWR events whose cortical activity was mainly dominated by one of the cortical pattern templates (Figure 4.6c, colored dots, 2D correlation > 0.45). In total, ~36 % of all the well-separated SWR events were assigned to one of the cortical pattern templates. The cortical activity averaged across the SWR events assigned to each cortical pattern template highly resembled the corresponding template (Figure 4.6d, compare to 4.6b). Thus, many SWR events accompany diverse sets of reproducible cortical activity patterns. For the SWR events assigned to the two patterns with peak activity immediately after ripple onset (pattern 2 and pattern 5), we also found the activity onset of most cortical regions preceded ripple onset by 0.16-0.6 s (Figure 4.S7b). Figure 4.6e shows the fraction of SWR events assigned to each pattern for all the mice. Overall, there were more SWR events associated with the posterior cortical patterns than the anterior patterns, suggesting a more frequent coupling between the hippocampus and posterior cortical regions during SWRs.

4.3.5 Different cortical patterns associate with distinct hippocampal activity

Considering that SWR-associated cortical activity exhibited distinct patterns, we explored whether hippocampal neuronal activity during individual SWR events is differentially modulated depending on the concurrent cortical patterns. In addition to SWRs, Neuro-FITM electrodes also

detect spikes from the nearby hippocampal neurons in multimodal experiments. Figure 4.7a shows 3 representative hippocampal neurons exhibiting selective (Neurons 1 and 2) or non-selective (Neuron 3) firing rates at the onsets of SWRs associated with different cortical patterns. To study the distinct modulation of hippocampal neurons during different cortical activity patterns, we performed SVM decoding analysis to examine whether cortical patterns could be discriminated based on the hippocampal population activity. SVM is a decoding technique that looks for a hyperplane to best separate the data according to their classes while maximizing the margin between the data samples and the hyperplane. SVM has been shown to give robust decoding performance for high dimensional data, especially when the size of dataset is limited. Because of this advantage, it has been commonly used to decode stimuli and choices using neuronal activity [24-28]. In this study, we built a SVM decoder that performs pairwise discrimination of cortical patterns based on hippocampal population activity. The SWR events associated with two cortical patterns were selected, and the decoder attempted to discriminate the cortical patterns using the spiking activity of the simultaneously recorded hippocampal neurons (12 ± 2 neurons in each animal, Figure 4.7b). We used the recursive feature elimination algorithm [29], which selected the subset of neurons in each decoder whose activity was significantly informative about the cortical activity patterns ('discriminant neurons'). This process was repeated for all pairs of cortical patterns. For many cortical pattern pairs, the cortical patterns could be discriminated significantly above chance based on the activity of hippocampal neurons during SWRs. Figure 4.7c shows the decoding accuracy for each cortical pattern pair from one example mouse. In all 6 mice, a large fraction of cortical pattern pairs was distinguishable (Figure 4.7d, Figure 4.S8). By examining the decodable cortical pattern pairs, we found that different subsets of hippocampal neurons were discriminant for different cortical pattern pairs (Figure 4.S9a), and all hippocampal neurons were

discriminant in at least one of the pairs. These results suggest that all hippocampal neurons are modulated differently depending on cortical activity patterns during SWRs. We also repeated the decoding analysis using hippocampal pyramidal cells and interneurons separately. We found that both hippocampal pyramidal cells and interneurons can decode the cortical activity pattern, indicating that both neuron types were modulated specifically during SWRs (Figure 4.S9b).

Given that many cortical pattern pairs could be decoded, we further investigated whether hippocampal neuron activity exhibited consistent modulations based on the different features of cortical activity patterns. To address this issue, we analyzed two groups of pattern pairs. One included pattern pairs with the same activation time course but different activated regions (anterior vs. posterior, pattern 1 vs. 4, 2 vs. 5, and 3 vs. 6), whereas the other included pattern pairs with the same activated regions but different time courses (early vs. late, e.g. pattern 1 vs. 2, or 4 vs. 5). To compare the activation levels of discriminant neurons determined by the recursive feature elimination algorithm for cortical pattern pairs (Figure 4.S9a), we defined the 'preference index' for each neuron as the difference in the spike counts during one pattern vs. the other, divided by the sum of the two (see Methods). When comparing posterior with anterior patterns activated at similar timing, we found that posterior patterns were associated with higher firing in a majority of discriminant neurons than the anterior patterns, which was evident in a significantly positive preference index (Figure 4.7e). In contrast, when comparing cortical activation of similar areas but with different timing, the general activity level of discriminant neurons did not show a significant preference for earlier vs. later activation (Figure 4.7e). Despite the lack of consistent difference in the general hippocampal activation level for early-late pattern pairs, their decoding accuracy was similar to that for anterior-posterior pattern pairs (Figure 4.7e). We also repeated the same decoding analysis and preference index analysis for all the ripple events, including the non-well-

separated SWRs (Figure 4.S10). The results are qualitatively similar compared to Figure 4.7, indicating that the conclusions are generalizable across heterogeneous ripples. Taken together, these results reveal diverse associations between cortical activity patterns and hippocampal neuronal activity during SWRs. The posterior cortical activation is associated with stronger hippocampal activation in most of the hippocampal neurons. The relative timing between cortex and SWRs is associated with heterogeneous modulation of individual hippocampal neurons.

4.4 Discussion

We developed a mostly-transparent, bendable microelectrode array (Neuro-FITM) to enable cortex-wide simultaneous optical imaging during electrophysiological recordings. To achieve the same goal, conventional silicon probes will have to be inserted contralaterally or horizontally, which would inevitably lead to long insertion trajectories causing additional implantation damage to the brain tissue. Furthermore, horizontal implantation will cause increased mechanical stress applied onto the thin silicon shank at the clamping point which can lead to premature fracture of the probe. Instead, our flexible array could be inserted vertically to the hippocampus with the shortest trajectory, minimizing brain tissue damage. In addition, our Neuro-FITM has up to 64 recording electrodes per shank, providing a higher spatial resolution for electrophysiology compared to other polymer-based microelectrodes used for hippocampal recordings [30,31]. Given the high flexibility and small dimensions of the insertable shank of the array, we anticipate that our flexible microelectrode array will improve the stability of unit recordings in chronic studies.

Our Neuro-FITM array could potentially be combined with other neural technologies that further expands its applications into various neuroscience studies. For example, Neuro-FITM array could be integrated with wireless electrophysiological recording platforms for wireless data

transmission [32-34], which are ideal for recordings in freely moving animals. Neuro-FITM array could also be augmented to allow simultaneous electrophysiological recordings and manipulations of neural activity. This could be achieved by optimizing the charge injection capacity of the electrodes for electrical stimulation [35], or by incorporating the μLEDs [36] or waveguides [37] into the device to form optoelectronic neural interfaces.

The simultaneous multimodal recordings of the hippocampal and cortical activity allowed us to characterize the cortical-hippocampal interactions during individual SWRs. In contrast to the conventional notion that cortical activity is mainly triggered by hippocampal SWRs [11,12,38-41] (but see [8-10,42]), our findings suggest that the hippocampus and cortex exhibit bidirectional communications with the cortical activation frequently preceding SWR onset. Furthermore, the relative timing between cortical activation and SWRs is area-specific. The cortical activation could start before or after SWRs in both anterior and posterior cortical regions, while the activation of posterior cortical regions precedes SWRs more frequently than that of anterior regions. A previous study in non-human primates performed simultaneous fMRI recordings of the whole brain and electrophysiological recordings of the hippocampus and showed that the activation of several cortical regions can on average precede hippocampal SWRs. However, the signal-to-noise ratio of fMRI limited their analysis to the average activity across SWRs and prevented the analysis of the diversity of cortical activity during individual SWRs [4]. The approach adopted in the current study achieved a sufficient signal-to-noise ratio to perform single-event analyses across large recording areas to uncover the remarkable and coordinated diversity of cortical and hippocampal activity during SWRs. The activation of different cortical regions with different timing relative to SWR onset forms distinct cortical activity patterns from SWR to SWR. Importantly, these cortical activity patterns differentially associate with the hippocampal neuronal activity which indicated

that these patterns are not merely random fluctuation but that there is rather a predictable relation of cortical activity patterns with hippocampal neuron populations, indicative of large-scale neuron assemblies that span the hippocampus and cortex.

The interaction between hippocampus and single brain regions under different behavioral states has been extensively studied. For example, it has been reported that awake SWRs were accompanied by the reactivation of neurons in the prefrontal cortex, suggesting that the awake SWRs played important roles in memory retrieval [11,43]. On the other hand, the existence of a bidirectional loop between the hippocampus and auditory cortex, which could play a role in memory consolidation, was also demonstrated [9]. A recent study showed that at a larger scale, the coupling between hippocampal ripples and ripples in association cortices becomes stronger after spatial learning, suggesting a closer communication between the hippocampus and association cortices during memory transfer [44]. Hippocampus encodes a variety of information including spatial, sensory, and reward [45-49]. The broad and diverse activation of cortical regions we observed during hippocampal SWRs may reflect a specific binding of distinct types of information encoded in hippocampus and the relevant cortical regions through different anatomical connections. The diversity of cortical-hippocampal interactions around SWRs suggests that the hippocampus and cortex can communicate through multiple information streams based on contexts and cognitive processes. Future studies should uncover how such cortical-hippocampal interaction is dynamically shaped when the animals are experiencing different task contexts or under different behavioral states.

4.5 Methods

4.5.1 Array design and measurement

The Neuro-FITM array has 32 or 64 electrodes with a flexible shank (Figure 4.1a-b, Figure 4.S1). The electrodes are aligned in two rows that are 20 μm apart from either edge of the probe. The diameter of each electrode is 10 μm and the spacing between adjacent electrodes is 50 or 20 μm. For the electrode designed to record in mouse hippocampus, the distance between the top and bottom electrodes is 750 μm, which is long enough to record from multiple depths of CA1 region in the dorsal-ventral axis. The microelectrode array consists of a 1.55 mm probe and a 1.9 cm transparent flexible shank, connecting the electrodes to the ZIF connector. To determine the optimal length of the shank for shuttle-free insertion, we performed mechanical analysis as shown in Equation 4.1, where $w = 170\ \mu m$, $t = 16\ \mu m$, L, and $E = 3.2\ GPa$ are the width, thickness, length, and the Young's modulus of the shank. The maximum force a probe can uphold without buckling is inversely proportional to the square of its length. Since the insertion force F required to penetrate brain tissue was commonly accepted to be 1 mN [50], we estimated the length of the probe must be shorter than 1.9 mm. Therefore, we chose the length of the probe to be 1.8 mm, which was long enough to target the CA1 region of the mouse hippocampus, yet short enough to prevent buckling during insertion.

$$F_{BF} = \frac{\pi^2 E w t^3}{5.88 L^2} \tag{4.1}$$

All electrochemical characterizations were performed with Gamry 600 Plus in 0.01 M phosphate-buffered saline (Sigma-Aldrich P3813 dry powder dissolved in deionized water). To measure the EIS and CV, we adopted a three-electrode configuration, where the Ag/AgCl (gauge 25) served as the reference electrode, and Pt (gauge 25) served as the counter electrode. During EIS, the applied AC voltage was 20 mV with frequency ranging from 100 kHz to 1 Hz at open circuit potential. We performed EIS of one representative array and the mean and s.d. were shown

in Figure 4.1k. During CV, the applied voltage between the PtNP/Au electrodes and the Ag/AgCl ranged from −0.9 V to 1 V (Figure 4.1l). To stabilize the electrode/electrolyte interface, we performed CV of a representative channel. During the measurement of CV and EIS, we used a custom-made Faraday cage to shield from the 60 Hz powerline contamination and other electromagnetic noises.

4.5.2 Animals

All procedures were performed in accordance with protocols approved by the UCSD Institutional Animal Care and Use Committee and guidelines of the National Institute of Health. Mice (cross between CaMKIIa-tTA:B6;CBA-Tg(Camk2a-tTA)1Mmay/J [JAX 003010] and tetO-GCaMP6s: B6;DBA-Tg(tetO-GCaMP6s)2Niell/J [JAX 024742], Jackson laboratories) were group-housed in disposable plastic cages with standard bedding in a room with a reversed light cycle (12 h-12 h). Temperatures and humidity ranged from 18-23 °C and 40-60%, respectively. Experiments were performed during the dark period. Both male and female healthy adult mice (6 weeks or older) were used. Mice had no prior history of experimental procedures that could affect the results.

4.5.3 Surgery, multimodal experiments, and data acquisition

Adult mice (6 weeks or older) were anesthetized with 1–2% isoflurane and injected with baytril (10 mg/kg) and buprenorphine (0.1 mg/kg) subcutaneously. A circular piece of scalp was removed to expose the skull. After cleaning the underlying bone using a surgical blade, a custom-built head-bar was implanted onto the exposed skull over the cerebellum (~1 mm posterior to lambda) with cyanoacrylate glue and cemented with dental acrylic (Lang Dental). Two stainless-steel wires (791900, A-M Systems) were implanted into the cerebellum as ground/reference. The

exposed skull was covered with cyanoacrylate glue applied several times. After cyanoacrylate glue formed a solid layer, a craniotomy (~0.5 mm in diameter, ~1.5-1.7 mm lateral, and ~2.1-2.3 mm posterior to bregma) was made at the right hemisphere for microelectrode array insertion and the dura over the exposed brain surface was carefully removed. The microelectrode array was connected to the amplifier board first and held by a custom-made electrode holder attached to a micromanipulator (MP-285, Sutter Instrument). The array was inserted at ~45 μm/s. Once inserted, the array was secured to the skull with Vetbond (3M). After the Vetbond became solid, the array was carefully released from the electrode holder and the exposed part of the array shank was bent to the right side of the animal. The amplifier board was fixed onto the right head-bar clamp arm on the stage (Figure 4.2a, Figure 4.S3a). Animals were fully awake before recordings. In 6 out of 8 animals, we successfully recorded SWRs and spikes in multiple recording channels. To quantify the accuracy of array implantation, we measured the distance between the target location and the actual location of the tip of the array based on the staining results (Figure 4.S3b). We find that the distance is 100 ± 33 μm in medial-lateral direction, 113 ± 18 μm in anterior-posterior direction, and 87± 24 μm in vertical direction.

The wide-field calcium imaging was performed using a commercial fluorescence microscope (Axio Zoom.V16, Zeiss, objective lens (1x, 0.25 NA)) and a CMOS camera (ORCA-Flash4.0 V2, Hamamatsu) through the intact skull as previously described[21]. Images were acquired using HCImage Live (Hamamatsu) at 29.98 Hz, 512×512 pixels (field of view: 11 mm x 11 mm, binning: 4, 16 bit).

The microelectrode array was attached to a custom-made connector board that routed the electrical signals to the Intan RHD2132 amplifier boards (Intan Technologies, USA). Electrophysiological recordings were performed using Intan RHD 2000 system. The sampling rate

was 30 kHz. For each animal, all recording sessions are on the same day with 5-10 min interval between sessions. In total, 6 mice were recorded, each having 2-3 sessions. The length of each session was 1 h.

4.5.4 Immunohistochemistry

The microelectrode array was left in the brain for 4-5 weeks before perfusion to allow glial scar formation, which is a good indication of the array location. The mice were anesthetized (ketamine/xylazine, 150 mg/kg, 12 mg/kg body weight) and perfused transcardially with 4% paraformaldehyde. Brains were then cryoprotected in a 30% sucrose solution overnight. 50 mm coronal sections were cut with a microtome (Microm HM 430, Thermo Scientific) and blocked in a solution consisting of 4% normal donkey serum, 1% BSA and 0.3% Triton X-100 in PBS for 1 h at room temperature. They were then incubated overnight at 4ºC with primary antibodies (1:1000 chicken anti-GFP, Aves Labs; 1:400 goat anti-GFAP, Santa Cruz) diluted in the blocking solution. After washing, sections were then incubated in Alexa Fluor–conjugated secondary antibodies (1:1000 anti-chicken 488; 1:1000 anti-goat 594, Jackson Immuno Research) for 2 h at room temperature. Slices were then mounted with a mounting medium for DAPI staining (Vector Laboratories) and imaged using a fluorescence microscope (ApoTome.2, Zeiss, Figure 4.2b, and Figure 4.S3b).

4.5.5 SWR detection, spike sorting, ΔF/F processing

The detection of SWRs was performed by the following procedures. The raw LFP signals from the channels near CA1 pyramidal layers were band-pass filtered at 100-200 Hz (8th order Butterworth filter) in both forward and reverse directions to prevent phase distortion. The Hilbert transform was then used to obtain the envelope of the ripple-band signals. To detect the potential

SWR events, we set a threshold to 2-3 standard deviations above the mean. Once the ripple-band envelope crossed the threshold, one candidate SWR event was labeled. The start and end time of this candidate SWR event was then defined as the time when the envelope just passed or returned back to the mean level. Between the start and end time, if the peak amplitude of the signal envelope further exceeded 4-6 standard deviations above the mean, then a SWR event was finally identified. Note that similar to other studies [51,52], we only considered SWR events with a duration longer than 20 ms.

The spike sorting was performed with Kilosort 2 [53] and the output results were followed by manual curation. The recording sessions from the same day were pooled together before the spike sorting to identify the same neurons across sessions. The LFP data were first high-pass filtered at 250 Hz (3rd order Butterworth filter) and whitened to remove the correlation between nearby channels. Then the Kilosort algorithm identified the best templates and the putative clusters of neurons along with their spike timing and amplitudes. These preliminary results were further manually refined by merging the same neurons, splitting different neurons, and labeling low amplitude inseparable spikes as multi-unit activities. Finally, the hippocampus pyramidal cells and interneurons were classified based on the firing rates and the asymmetry of the spike waveforms [54].

To obtain the ΔF/F time series from the wide-field calcium imaging data, 512 x 512 pixel images were first down-sampled to 128×128 pixels. For each pixel, time-varying baseline fluorescence (F) was estimated for a given time point as the 10th percentile value over 180 s around it. For the beginning and end of each imaging block, the following and preceding 90-s window was used to determine the baseline, respectively. The raw ΔF/F of each pixel was z-score normalized. We corrected for hemodynamic contamination following published procedures [21].

Briefly, we performed principal component analysis (PCA) followed by independent component analysis (ICA) [21] on z-score normalized ΔF/F to extract hemodynamic components from total signal. We first performed PCA and preserved the top 50 principal components, which explained ~95% variance of the data. Then the spatial ICA was performed over the top 50 PCs to generate 50 spatially independent modules. Finally, the modules containing the vasculature activities were excluded and the reconstruction of cortical activity was done with the remaining modules. We screened different numbers of components (20, 40, 50, 150, and 200) preserved in PCA/ICA analysis and using 50 components gave the best separation of hemodynamic and neural signal. To obtain the ΔF/F of each cortical region, the dorsal cortex was manually parcellated into individual regions based on Allen Brain Atlas (Figure 4.5b) and ΔF/F time series was computed as the mean of the pixel values within each cortical region.

4.5.6 The time delay between cortical activation and SWRs

For the analysis of the timing of SWR onset and the onset of dorsal cortex activity averaged across SWR events (Figure 4.5a, Figure 4.S4), we only included the 'well-separated SWRs' which did not have any preceding SWR events for at least 3 seconds. This was to prevent potential contamination from the tail of cortical activity associated with preceding SWRs. The onset timing of the event-averaged cortical activity was defined as the earliest activity onset among 16 cortical regions. For each region, using the ΔF/F at -2 s relative to SWR onset as the baseline, we performed rank-sum tests at each frame between [-2 s, 2 s] relative to SWR onset. The activity onset time for each cortical region was defined as the time when its ΔF/F was significantly higher ($P < 0.05$) than the baseline for at least 3 consecutive frames. The mean onset time was computed by first averaging across sessions within animals and later averaging across animals. The peak time of event-averaged cortical activity was defined as the time when cortical activity averaged across 16

regions reached the maximum value. The mean peak time was computed by first averaging across sessions within animals and then averaging across animals.

For the analysis of timing between SWR onset and the activity onset of each cortical region during individual SWRs (Figure 4.5d-e, Figure 4.S5), we also focused on well-separated SWR events. The activity onset of each cortical region was identified as previously described[21]. In brief, we first computed the derivative of the smoothed ΔF/F traces (loess, 1-s window) and defined the inactive segments as the periods with the derivative within 1 standard deviation of the whole derivative trace. Then we defined ΔF/F events as the periods when the derivative exceeded the 1 standard deviation of the inactive period. For each event, the onset time was first estimated as the time when the derivative exceeded the 1 standard deviation criterion, and the offset time was estimated as the time when the derivative dropped below zero for the first time after the onset. To further refine the onset time, for each event, the baseline ΔF/F was defined as the value at the first time point when the derivative was above zero before the offset time, and ΔF/F noise level was defined as the mean of the absolute difference between the raw and smoothed ΔF/F traces. The onset was further refined as the last time point before the offset time when the ΔF/F value is within the noise level from the baseline ΔF/F.

After identifying the activity onset of each cortical region, we determined the timing of each SWR onset relative to the activity onset of each region using the following procedures. For each SWR onset, we first examined the slope of the instantaneous ΔF/F traces of one region. If the ΔF/F was rising, we looped backward in time frame by frame until reaching -1 s before the SWR onset. If a cortical activity onset was detected within this time interval, we labeled this SWR event as occurring after the cortical activity onset. On the other hand, if the ΔF/F was not rising, we looped forward in time frame by frame until reaching +1 s after the SWR onset. If a cortical activity

onset was detected within this time interval, we labeled this SWR event as occurring before the cortical activity onset. The above procedure was done for every well-separated SWR and all the cortical regions.

4.5.7 Two-stage TCA algorithm

To prepare the data for the TCA algorithm, we performed below preprocessing procedures. The ΔF/F traces in each cortical region were z-score normalized within each recording session. For each SWR event, we used the 3-s ΔF/F traces (1 s before SWR onset, 2 s after) from 16 cortical regions to construct a 2D data matrix (region × time). Then we concatenated the 2D data matrices from all the SWR events to form a 3D data tensor (region × time × event). Finally, the data tensors from all the 6 mice were concatenated along the event dimension to form a big data tensor (Figure 4.6a).

The tensor component analysis (TCA) has been demonstrated to be effective in discovering the low-dimensional dynamics of neural activity [13]. However, since the original algorithm did not guarantee to achieve the global optimum, the results could vary from run to run. To achieve reliable results, we devised a two-stage TCA algorithm, which includes a pre-clustering step to alleviate the variations from individual runs. The detailed procedure is shown in Extended Data Figure 4.6a. The first stage of the algorithm consisted of fitting a TCA model with a sufficiently high rank order. The tensor toolbox v3.0 (https://www.tensortoolbox.org/) was used to perform TCA decomposition. To determine this rank order, we fitted multiple TCA models with rank 2 to 15 and examined the reconstruction error of each TCA model. The reconstruction error started to show diminishing returns towards rank 15 (Figure 4.S6b). Therefore, we chose rank 15 for the initial TCA and ran it 100 times. Each result gave a slightly different decomposition of the original high dimensional data. To capture the underlying dynamics that were common and consistent in

most TCA results, we performed clustering of the 1500 TCA spatiotemporal patterns by computing the similarity matrix using 2D correlation. Then the community detection algorithm was performed with the community detection toolbox (http://netwiki.amath.unc.edu/GenLouvain/GenLouvain) to identify the clusters. As shown in the sorted similarity matrix (Figure 4.S6c), we identified 8 different clusters of TCA patterns. The number of patterns assigned to each cluster is shown in Figure 4.S6d. Examples of randomly chosen patterns assigned to each cluster are shown in Figure 4.S6f. The second stage of the TCA algorithm used the centroids of 8 clusters identified from the first stage to initialize the region and time factors, leaving all the event factors randomly initialized. Then we ran the TCA optimization algorithm as before until it converged to obtain the final set of TCA factors (Figure 4.S7a). Compared with the original TCA algorithm, our two-stage TCA algorithm gave significantly lower reconstruction error ($p = 1.38E-11$, Figure 4.S6e).

4.5.8 Cortical pattern assignment

To assign the cortical activity pattern of each SWR event to one of the 8 spatiotemporal templates (Figure 4.6b), we computed the 2D correlation between the z-score normalized $\Delta F/F$ traces and each template. If the correlation value for one pattern was higher than a threshold (0.45, Figure 4.6c-e), we assigned the SWR event to that pattern. If one SWR event was assigned to multiple patterns, we excluded that SWR event.

4.5.9 The algorithm for pairwise discrimination of the cortical patterns

To discriminate the cortical patterns based on hippocampal activity, we used the support vector machine (SVM). The hippocampal neuron firing counts during 0-100 ms relative to SWR onset were used as input features for the SVM algorithm. Since the numbers of SWR events assigned to each cortical pattern templates were often unbalanced (Figure 4.6e), we modified the

misclassification costs to be inversely proportional to the sample frequencies of the two pattern types in each pair, N1 and N2. Therefore, misclassifying pattern type 1 as pattern type 2 had cost N2 / (N1+N2), whereas misclassifying pattern type 2 as pattern type 1 had cost N1 / (N1+N2). Also, to measure the decoding performance, we used balanced accuracy instead of the accuracy, which could be misleading in the unbalanced datasets. The balanced accuracy was defined as the average of the correct proportion for each class (i.e. cortical pattern). We performed the recursive feature elimination [29,55] to identify the discriminant neurons for each cortical pattern pair (Figure 4.S9). This was done by choosing the subset of neurons that give the highest balanced accuracy in the leave-one-out cross-validation. To evaluate whether the decoding performance for each cortical pattern pair was significantly better than chance, we randomly shuffled the cortical pattern identities 2000 times, performed SVM using the identified discriminant neurons, and computed the balanced accuracy in each shuffle to obtain a null distribution of it. Then we computed the p-value based on the balanced accuracy from the original data set and the distribution of the balanced accuracy from the shuffled data set (Figure 4.7c, Figure 4.S10b, and Figure 4.S8). The exact p values associated with Figure 4.7c are as follows: Mouse 1: *P(1-2)=0.086, P(1-3)=0.2815, P(1-4)=0.1415, P(1-5)=0.153, P(1-6)=0.0035, P(1-7)=0.094, P(1-8)=0.0965, P(2-3)=0.3365, P(2-4)=0.0315, P(2-5)=0.036, P(2-6)=0.0535, P(2-7)=0.0245, P(2-8)=0.0425, P(3-4)=0.5235, P(3-5)=0.28, P(3-6)=0.052, P(3-7)=0.037, P(3-8)=0.3795, P(4-5)=0.13, P(4-6)=0.0695, P(4-7)=0.005, P(4-8)=0.016, P(5-6)=0.153, P(5-7)=0.017, P(5-8)=0.062, P(6-7)=0.0205, P(6-8)=0.0025, P(7-8)=0.0275*; Mouse 2: P(1-2)=0.0035, P(1-3)=0.0045, P(1-4)=0.004, P(1-5)=0.0665, P(1-6)=0, P(1-7)=0, P(1-8)=0, P(2-3)=0.009, P(2-4)=0.017, P(2-5)=0.0525, P(2-6)=0.0375, P(2-7)=0.0055, P(2-8)=0.0005, P(3-4)=0.039, P(3-5)=0.007, P(3-6)=0.0545, P(3-7)=0.035, P(3-8)=0.0025, P(4-5)=0.0125, P(4-6)=0.001, P(4-7)=0.002, P(4-8)=0,

P(5-6)=0.0085, P(5-7)=0.006, P(5-8)=0.0015, P(6-7)=0, P(6-8)=0.001, P(7-8)=0; Mouse 3: P(1-2)=0.0105, P(1-3)=0.015, P(1-4)=0.024, P(1-5)=0.0275, P(1-6)=0.0035, P(1-7)=0, P(1-8)=0.0295, P(2-3)=0.008, P(2-4)=0.006, P(2-5)=0.017, P(2-6)=0.2245, P(2-7)=0.0015, P(2-8)=0.0135, P(3-4)=0.0005, P(3-5)=0.017, P(3-6)=0.1865, P(3-7)=0.001, P(3-8)=0.015, P(4-5)=0.047, P(4-6)=0.001, P(4-7)=0.0035, P(4-8)=0.041, P(5-6)=0.0035, P(5-7)=0, P(5-8)=0.0165, P(6-7)=0.0295, P(6-8)=0.034, P(7-8)=0.2295; Mouse 4: P(1-2)=0.0055, P(1-3)=0.0085, P(1-4)=0.023, P(1-5)=0.0135, P(1-6)=0.054, P(1-7)=0.0135, P(1-8)=0.167, P(2-3)=0.073, P(2-4)=0.013, P(2-5)=0.037, P(2-6)=0.0765, P(2-7)=0.3305, P(2-8)=0.1825, P(3-4)=0.25, P(3-5)=0.0675, P(3-6)=0.0175, P(3-7)=0.03, P(3-8)=0.029, P(4-5)=0.034, P(4-6)=0.0905, P(4-7)=0.0375, P(4-8)=0.0675, P(5-6)=0.0015, P(5-7)=0.0775, P(5-8)=0.0285, P(6-7)=0.046, P(6-8)=0.094, P(7-8)=0.39; Mouse 5: P(1-2)=0.0335, P(1-3)=0.0755, P(1-4)=0.009, P(1-5)=0.0075, P(1-6)=0.013, P(1-7)=0, P(1-8)=0.0055, P(2-3)=0.0295, P(2-4)=0.0145, P(2-5)=0.0495, P(2-6)=0.057, P(2-7)=0.0215, P(2-8)=0.1255, P(3-4)=0.0875, P(3-5)=0.0195, P(3-6)=0.015, P(3-7)=0.0095, P(3-8)=0.0535, P(4-5)=0.0155, P(4-6)=0.009, P(4-7)=0.0325, P(4-8)=0.0245, P(5-6)=0.0145, P(5-7)=0.0415, P(5-8)=0.026, P(6-7)=0.007, P(6-8)=0.0065, P(7-8)=0.1315; Mouse 6: P(1-2)=0.018, P(1-3)=0.0175, P(1-4)=0.017, P(1-5)=0.0065, P(1-6)=0.046, P(1-7)=0.013, P(1-8)=0.001, P(2-3)=0.007, P(2-4)=0.0105, P(2-5)=0.108, P(2-6)=0.0115, P(2-7)=0.1615, P(2-8)=0.0025, P(3-4)=0.0345, P(3-5)=0.0025, P(3-6)=0.008, P(3-7)=0.001, P(3-8)=0.0045, P(4-5)=0.0835, P(4-6)=0.0015, P(4-7)=0.062, P(4-8)=0.017, P(5-6)=0.0315, P(5-7)=0.03, P(5-8)=0.0065, P(6-7)=0.0055, P(6-8)=0.0025, P(7-8)=0.0125. The exact p-values associated with Figure 4.S10b are as follows: Mouse 1: P(1-2)=0.0645, P(1-3)=0.1735, P(1-4)=0.0315, P(1-5)=0.057, P(1-6)=0.128, P(1-7)=0.008, P(1-8)=0.027, P(2-3)=0.1735, P(2-4)=0.0375, P(2-5)=0.0025, P(2-6)=0.0205, P(2-7)=0.0135, P(2-8)=0.345, P(3-4)=0.1685, P(3-5)=0.0225, P(3-6)=0.012, P(3-7)=0.04, P(3-

8)=0.3775, P(4-5)=0.01, P(4-6)=0.3415, P(4-7)=0.0415, P(4-8)=0.289, P(5-6)=0.042, P(5-7)=0.1595, P(5-8)=0.066, P(6-7)=0.473, P(6-8)=0.01, P(7-8)=0.07; Mouse 2: P(1-2)=0.018, P(1-3)=0.034, P(1-4)=0.007, P(1-5)=0.114, P(1-6)=0.0065, P(1-7)=0.0245, P(1-8)=0, P(2-3)=0.0135, P(2-4)=0.012, P(2-5)=0.0115, P(2-6)=0.037, P(2-7)=0.0205, P(2-8)=0, P(3-4)=0.058, P(3-5)=0, P(3-6)=0.02, P(3-7)=0.0345, P(3-8)=0.0035, P(4-5)=0.0115, P(4-6)=0.0015, P(4-7)=0, P(4-8)=0, P(5-6)=0.0465, P(5-7)=0.009, P(5-8)=0, P(6-7)=0, P(6-8)=0, P(7-8)=0; Mouse 3: P(1-2)=0, P(1-3)=0.001, P(1-4)=0.0135, P(1-5)=0.035, P(1-6)=0.011, P(1-7)=0.0935, P(1-8)=0.001, P(2-3)=0.0575, P(2-4)=0.0015, P(2-5)=0.003, P(2-6)=0.0515, P(2-7)=0.0045, P(2-8)=0.0015, P(3-4)=0.0025, P(3-5)=0.0225, P(3-6)=0.2895, P(3-7)=0.0045, P(3-8)=0.0025, P(4-5)=0.002, P(4-6)=0.0295, P(4-7)=0.002, P(4-8)=0.0205, P(5-6)=0.023, P(5-7)=0.0055, P(5-8)=0.01, P(6-7)=0.088, P(6-8)=0.002, P(7-8)=0.0355; Mouse 4: P(1-2)=0.221, P(1-3)=0.177, P(1-4)=0.111, P(1-5)=0.0335, P(1-6)=0.011, P(1-7)=0.0175, P(1-8)=0.0435, P(2-3)=0.0765, P(2-4)=0.0025, P(2-5)=0.0205, P(2-6)=0.0615, P(2-7)=0.001, P(2-8)=0.143, P(3-4)=0.2925, P(3-5)=0.0335, P(3-6)=0.009, P(3-7)=0.049, P(3-8)=0.0335, P(4-5)=0.0105, P(4-6)=0.123, P(4-7)=0.022, P(4-8)=0.1275, P(5-6)=0.0195, P(5-7)=0.105, P(5-8)=0.1305, P(6-7)=0.0875, P(6-8)=0.0255, P(7-8)=0.11; Mouse 5: P(1-2)=0.085, P(1-3)=0.627, P(1-4)=0.1625, P(1-5)=0.4755, P(1-6)=0.024, P(1-7)=0.259, P(1-8)=0.009, P(2-3)=0.105, P(2-4)=0.052, P(2-5)=0.1565, P(2-6)=0, P(2-7)=0.0065, P(2-8)=0.09, P(3-4)=0.142, P(3-5)=0.0705, P(3-6)=0.176, P(3-7)=0.014, P(3-8)=0.12, P(4-5)=0.0705, P(4-6)=0.0015, P(4-7)=0.2375, P(4-8)=0.007, P(5-6)=0.001, P(5-7)=0.185, P(5-8)=0.0995, P(6-7)=0.0075, P(6-8)=0.0105, P(7-8)=0.115; Mouse 6: P(1-2)=0.063, P(1-3)=0.021, P(1-4)=0.023, P(1-5)=0.0065, P(1-6)=0.0995, P(1-7)=0.013, P(1-8)=0.1085, P(2-3)=0.01, P(2-4)=0.0105, P(2-5)=0.004, P(2-6)=0.0455, P(2-7)=0.0925, P(2-8)=0.0005, P(3-4)=0.008, P(3-5)=0.004, P(3-6)=0.044, P(3-7)=0.003, P(3-8)=0.0165, P(4-5)=0.0105, P(4-6)=0.034, P(4-

7)=0.2415, P(4-8)=0.077, P(5-6)=0.011, P(5-7)=0.0035, P(5-8)=0.045, P(6-7)=0.0035, P(6-8)=0.033, P(7-8)=0.012. Finally, to further quantify the overall decoding performance for each mouse, we computed the fraction of distinguishable cortical pattern pairs ($P < 0.05$) over the cortical pattern pairs included in the analysis within each animal (Figure 4.7d, Figure 4.S10c). To examine whether the fraction of distinguishable cortical pattern pairs in each animal is significant, we test against the null hypothesis that the fraction is obtained out of chance. Since the probability of each pattern pair being mislabeled as distinguishable is 0.05, under the null hypothesis, the number of distinguishable pairs in each mouse follows a binomial distribution where the parameter p equals 0.05 and N equals the number of pattern pairs included in analysis within each animal. Therefore, the critical number of pattern pairs N_c is determined as the smallest integer that makes the binomial cumulative density function larger than 0.95. Finally, the chance level fraction is obtained as the ratio between N_c and N.

4.5.10 Hippocampal neuron firing rates under different cortical patterns during SWRs

To obtain the instantaneous firing rates between -1 s and 2 s relative to SWR onset for each hippocampal neuron, we used 100-ms time bins without overlap for each SWR event (Figure 4.7a, Figure 4.10a). We defined the preference index (P.I.) to measure whether one neuron showed higher activity for one pattern than the other (Figure 4.7e, Figure 4.S10d). For each pattern pair (e.g. pattern X and pattern Y), the preference index of one neuron was calculated using its mean firing count between 0-100 ms relative to SWR onset under each pattern, as shown in Equation 4.2.

$$P.I.(X) = \frac{Firing\ Count(X) - Firing\ Count(Y)}{Firing\ Count(X) + Firing\ Count(Y)} \tag{4.2}$$

The early vs. late group included pattern pairs of pattern 1 vs. 2, 1 vs. 3, 2 vs. 3, 4 vs. 5, 4 vs. 6, and 5 vs. 6. The anterior vs. posterior group included pattern pairs of pattern 1 vs. 4, 2 vs. 5, and 3 vs. 6. For each cortical pattern pair, the preference index at population level was calculated by averaging across discriminant hippocampal neurons (Figure 4.7e, Figure 4.S10d).

4.5.11 Statistics and Reproducibility

For electrode arrays designed for recordings in mice, rats, and monkeys, four electrode arrays were imaged respectively and example images are shown in Figure 4.1 and Figure 4.S1. Two animals were excluded from 8 animals from recordings and analyses due to unsuccessful implantations. The 6 animals with successful implantations went through the same recording procedures and were all included in analyses. All statistical analyses were performed in MATLAB. Statistical tests were two-tailed and significance was defined by alpha pre-set to 0.05. Error bars and shaded regions surrounding line-plots indicate ± standard error of the mean (s.e.m.) unless otherwise noted. All the statistical tests are described in the figure legends and each test was selected based on data distributions using histograms. For Figure 4.1m, a two-sided Student's T-test was used to test the correlation between the electrode impedance and the recording noise level. For Figure 4.5d and 4.5e, a two-tailed bootstrap test (10000 times) was used to test the median time difference between SWR and cortical activity onset and the fraction of SWR events occurring before or after cortical activity onset. For Figure 4.7c, the decodable pattern pair was determined by a one-tailed shuffling test, which randomly permuted the labels of cortical patterns. For Figure 4.7d, the chance level number of decodable pattern pairs (nc) was computed from the inverse of binomial cumulative distribution with probability 0.95 and the chance level fraction was obtained

by dividing nc with n = 28, the number of pattern pairs on which decoding was performed. For Figure 4.7e, a two-tailed bootstrap test (10000 times) was used to determine the significance of preference index and the balanced accuracy. Multiple comparisons were corrected for by Benjamini-Hochberg corrections. Sample sizes (n) are as follows where applicable. Recording sessions per animal: 2, 3, 3, 3, 2, 2. Well-separated SWRs / all SWRs per animal: 530/1245, 896/1785, 787/1440, 826/1618, 673/1365, 578/1190. Hippocampal neurons per animal: 8, 21, 14, 11, 10, 10. No statistical methods were used to predetermine sample size but our sample sizes are similar to those reported in previous publications from our lab [21] and others using wide-field calcium imaging [56,57] and electrophysiological recordings [58]. No randomization was performed. Randomization is not necessary to our study as all animals underwent the same surgical and recording procedures. Data collection and analysis were not performed blind to the conditions of the experiments.

4.6 Acknowledgments

We thank Q. Chen, O. Arroyo, and L. Hall for technical assistance, and members of the Kuzum and Komiyama labs for discussions. This research was supported by grants from the ONR Young Investigator Award (N00014161253), NSF (ECCS-2024776, ECCS-1752241, and ECCS-1734940) and NIH (R21 EY029466, R21 EB026180, and DP2 EB030992) to DK, and grants from NIH (R01 NS091010A, R01 EY025349, R01 DC014690, R21 NS109722, and P30 EY022589), Pew Charitable Trusts, and David & Lucile Packard Foundation to T.K. Fabrication of the electrodes was performed at the San Diego Nanotechnology Infrastructure (SDNI) of UCSD, a member of the National Nanotechnology Coordinated Infrastructure, which is supported by the National Science Foundation (Grant ECCS-1542148).

Chapter 4 is a reprint of X. Liu, C. Ren, Y. Lu, Y. Liu, J. Kim, S. Leutgeb, T. Komiyama, D. Kuzum, Multimodal neural recordings with Neuro-FITM uncover diverse patterns of cortical-hippocampal interactions, Nature Neuroscience, accepted (2021). The dissertation author was the co-first author of this article.

4.7 Figures

Figure 4. 1 Characterization of Neuro-FITM

(a) Neuro-FITM connected to the custom PCB board. (b) Microscope image showing the layout of the microelectrode array. (c) Schematic showing exploded view of 3-layered structure of Neuro-FITM. (d)-(f), Scanning electron microscope (SEM) images of the array showing 10 μm-diameter microelectrode openings and 2 μm-wide wires connecting to the microelectrodes. (g)-(i), SEM images showing PtNPs deposited onto the Au microelectrodes. (j) Electrode impedance as a function of deposition time during Platinum nanoparticle (PtNP) deposition (mean ± s.d., n = 3 electrodes for 60, 90, 180, 210, and 270 s deposition time, n = 4 electrodes for 120, 150, 240 s deposition time). (k) Electrochemical impedance spectroscopy magnitude (left) and phase (right) are compared between Au and PtNP-deposited Au electrodes. PtNPs reduced the impedance of Au electrodes. The phase plot shows that PtNP electrodes are more resistive at higher frequency ranges than Au electrodes, consistent with the reduction in the impedance magnitude (mean ± s.d., n = 26 electrodes for Au and n = 21 electrodes for PtNP). (l) Cyclic voltammetry characteristics of PtNP-deposited electrodes showing redox peaks corresponding to electrochemical reactions of Pt, indicating an active engagement of PtNPs in the redox processes at the electrochemical interface. (m) Noise level for electrodes with different impedances measured in 0.1 M PBS solution. Recorded signals were first high-pass filtered at 5Hz and chunked into non-overlapping 1 s segments. The noise level for each segment was defined as its root-mean-square value. Each dot marks the mean noise level for each recording channel. The error bar marks the s.e.m. n = 87 measurements. The noise levels are higher for electrodes with higher impedance (two-sided Student's T-test, P = 6.81E-6, n = 23, degree of freedom = 21). (n) Transmittance of the substrate, the bent shank, the recording tip, and the total shank as a function of wavelength.

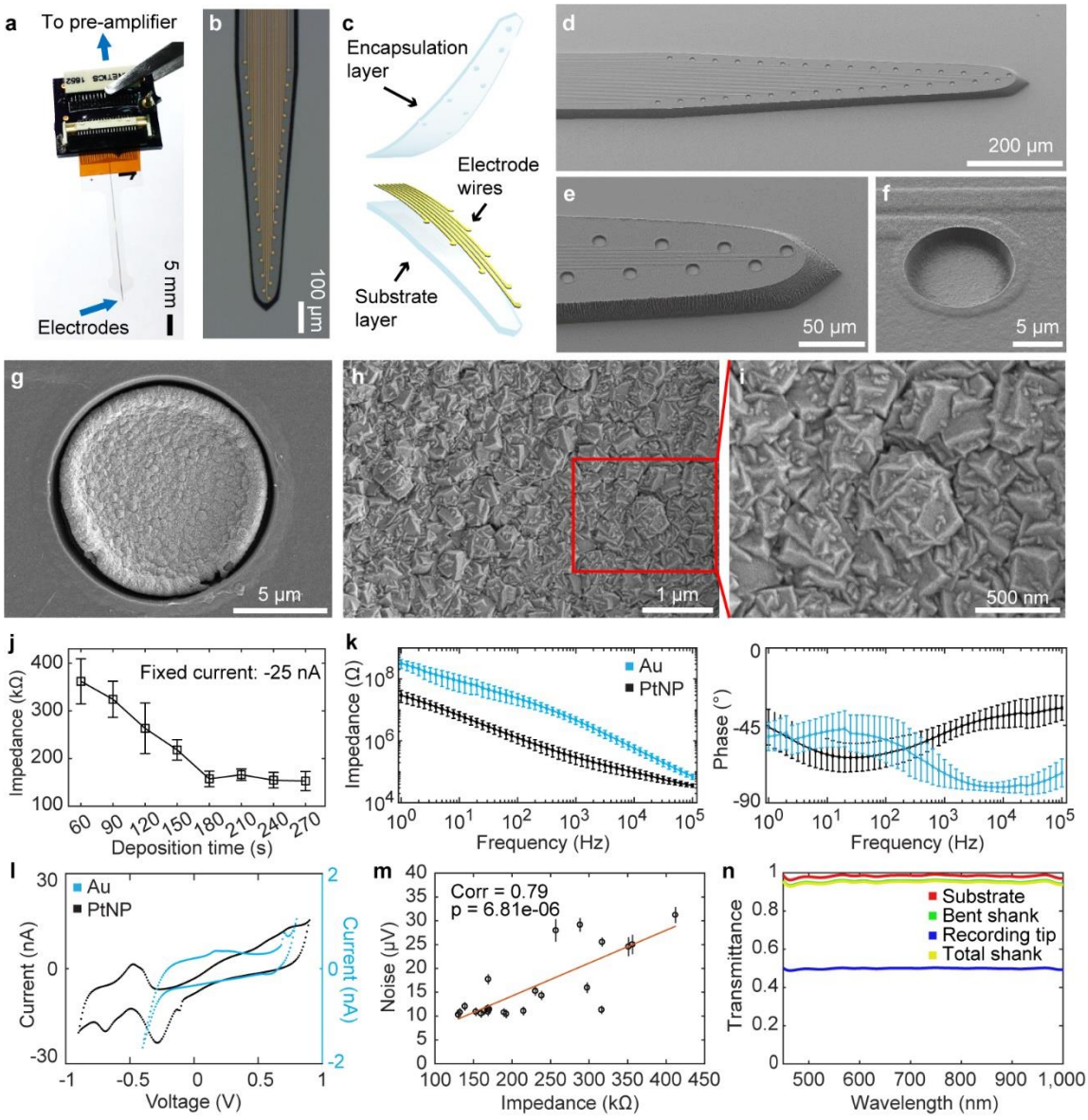
a
To pre-amplifier
5 mm
Electrodes
b
100 µm
c
Encapsulation layer
Electrode wires
Substrate layer
d
200 µm
e
50 µm
f
5 µm
g
5 µm
h
1 µm
i
500 nm
j
Fixed current: -25 nA
Impedance (kΩ)
Deposition time (s)
k
Au
PtNP
Impedance (Ω)
Frequency (Hz)
Phase (°)
Frequency (Hz)
l
Au
PtNP
Current (nA)
Voltage (V)
m
Corr = 0.79
p = 6.81e-06
Noise (µV)
Impedance (kΩ)
n
Substrate
Bent shank
Recording tip
Total shank
Transmittance
Wavelength (nm)

Figure 4. 2 Simultaneous multimodal recordings from the hippocampus and cortex.

(a) Surgical setup. Neuro-FITM was first inserted into the hippocampus (left) and then the shank was bent down to the right side to allow lowering the microscope objective and clearing the field of view for imaging (right). (b) Penetrating trajectory of Neuro-FITM in the hippocampus visualized by immunostaining against glia acidic protein (GFAP). Arrowhead: trajectory in CA1 pyramidal layer. (c) Field of view of wide-field calcium imaging during experiment. Note that the array shank was largely invisible and generated minimal shadows on the overlaying cortex. (d) Representative LFP recordings from the channels of the Neuro-FIRM probe in one recording session. Multiple channels adjacent (red) to the pyramidal layer of CA1 detected SWRs. (e) Examples of simultaneously recorded hippocampal SWRs (left column) and cortical activity (right column, single image frames at SWR onset). Cortical activity shows diverse spatial patterns during SWRs.

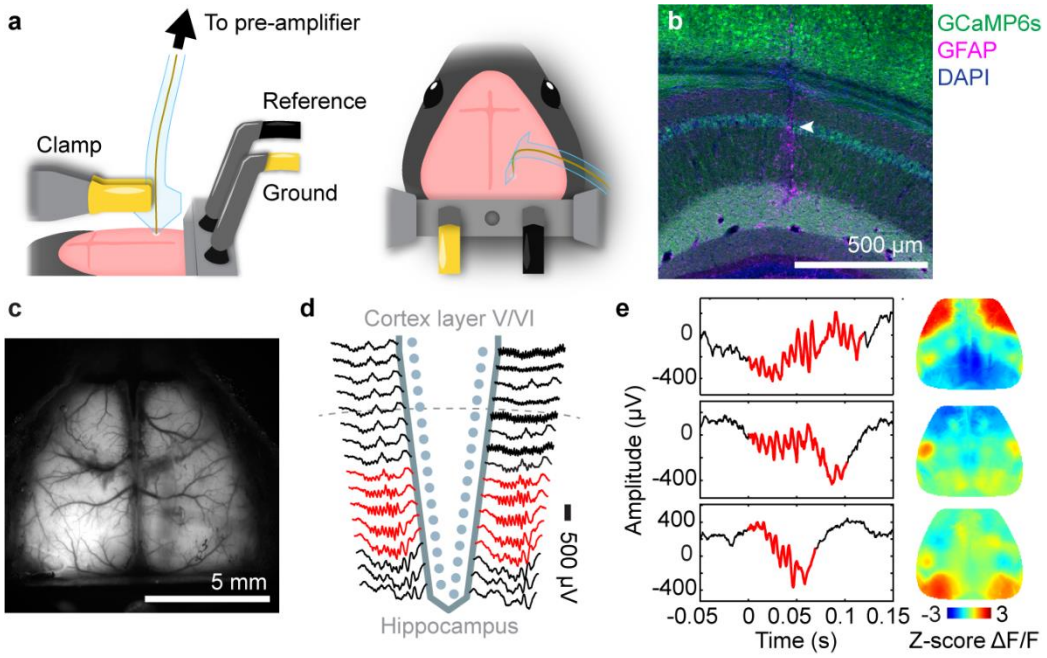
a
To pre-amplifier
Reference
Clamp
Ground
b
GCaMP6s
GFAP
DAPI
500 µm
c
5 mm
d
Cortex layer V/VI
500 µV
Hippocampus
e
0
-400
0
-400
400
0
-400
Amplitude (µV)
-0.05 0 0.05 0.1 0.15
Time (s)
-3
3
Z-score ΔF/F

Figure 4. 3 The neuron spike waveforms in different recording sessions from one mouse.

(a) Spatial profiles of spike waveforms of all 21 neurons recorded across 32 channels in three recording sessions marked by three different colors. Many neurons exhibit stable waveforms that are most prominent in adjacent channels. (b) Spike waveforms of all 21 neurons from the channel with the largest amplitude recorded in 3 sessions. Different colors indicate different recording sessions, as in a. The waveforms of the same neuron recorded at different sessions are highly similar.


a
Neuron 1
Neuron 2
Neuron 3
Neuron 4
Neuron 5
Neuron 6
Neuron 7
Neuron 8
Neuron 9
Neuron 10
Neuron 11
Neuron 12
Neuron 13
Neuron 14
Neuron 15
Neuron 16
Neuron 17
Neuron 18
Neuron 19
Neuron 20
Neuron 21
100 µV
1 ms
b
Amplitude (µV)
Time (s)

Figure 4. 4 SNR for the spikes, the LFP, and the wide-field fluorescence.

(a) Representative example of high-pass filtered data from one channel showing the detection of multiple spikes and the median absolute deviation (MAD) denoted by the width between two red dashed lines. (b) SNR of the recorded spikes in all 6 mice. Bar shows the mean SNR averaged over all the neurons and the error bar denotes the s.e.m. Each dot represents the spike SNR for one neuron. (c) Histogram of amplitude of the detected ripples. The red line shows the MAD of the ripple range LFP (120 Hz – 250 Hz). (d) Mean SNR for the ripples detected in all 6 mice. Each dot represents the mean SNR of the ripples recorded in one recording channel. (e) Histogram of amplitude of the sharp-waves during SWR. The red line shows the MAD of the sharp-wave range LFP (5 Hz – 50 Hz). (f) Mean SNR for the sharp-waves detected in all 6 mice. Each dot represents the mean SNR of the sharp-waves recorded in one recording channel. (g) Signal-to-noise ratio of the $\Delta F/F$ for the cortical regions covered by the array shank (ipsilateral) vs. the symmetric cortical regions on the contralateral side, showing similar SNR for both cases.

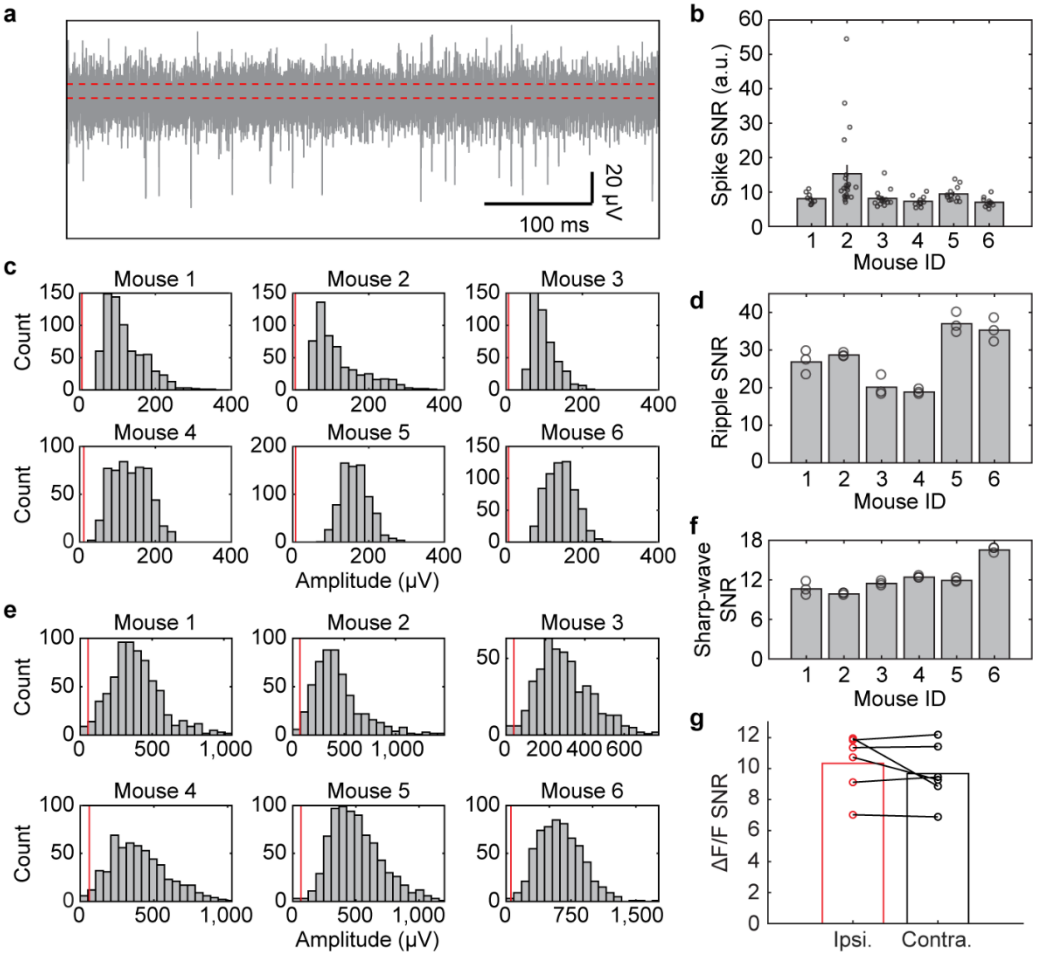
a
20 μV
100 ms
b
Spike SNR (a.u.)
Mouse ID
c
Mouse 1
Mouse 2
Mouse 3
Mouse 4
Mouse 5
Mouse 6
Count
Amplitude (μV)
d
Ripple SNR
Mouse ID
e
Mouse 1
Mouse 2
Mouse 3
Mouse 4
Mouse 5
Mouse 6
Count
Amplitude (μV)
f
Sharp-wave SNR
Mouse ID
g
ΔF/F SNR
Ipsi.
Contra.

Figure 4. 5 Cortical activity onset tends to precede SWRs

(a) Average cortical activity aligned to SWR onset from one example mouse. The cortex exhibited broad activation around SWRs with the cortical activity rising before SWR onset. Red dashed box: SWR onset. (b) Identified cortical regions based on Allen Brain Atlas. M2: secondary motor cortex; M1: primary motor cortex; S1: primary somatosensory cortex; S2: secondary somatosensory cortex; Aud: auditory cortex; PPC: posterior parietal cortex; RSC: retrosplenial cortex; Vis: visual cortex. (c) Average activity in 16 cortical regions aligned to SWR onset (mean ± s.e.m., across 6 animals). All cortical regions increased activity around SWRs. Red dashed lines: SWR onset. (d) Time difference of SWR onset relative to cortical activity onset (two-tailed bootstrap test, 10000 times, Benjamini–Hochberg adjusted for FDR = 0.05, $*P < 0.05$, $**P < 0.01$,$***P < 0.001$). Gray circles: median time difference for each mouse. The time difference exhibited an anterior-posterior gradient with earlier activity onset in posterior regions. All error bars are s.e.m., n = 6 mice. The adjusted p-values are 0.123, 0.050, 1.656, 1.493, 0.420, 0.050, 0, 0, 0, 0, 0.005, 0, 0, 0.001, 0, 0. (e) Fraction of SWR events with cortical activity onset before or after SWR onset (two-tailed bootstrap test, 10000 times, Benjamini–Hochberg adjusted for FDR = 0.05, $*P < 0.05$, $**P < 0.01$,$***P < 0.001$). Gray dots: fraction of SWR events before or after cortical activity onset for each mouse. From anterior to posterior regions, the fraction of SWR events with cortical activity onset leading SWRs increased. All error bars are s.e.m., n = 6 mice. The adjusted p-values are 0.016, 0.047, 1.601, 1.317, 0.319, 0.007, 0, 0, 0, 0, 0, 0, 0.003, 0.002, 0, 0.

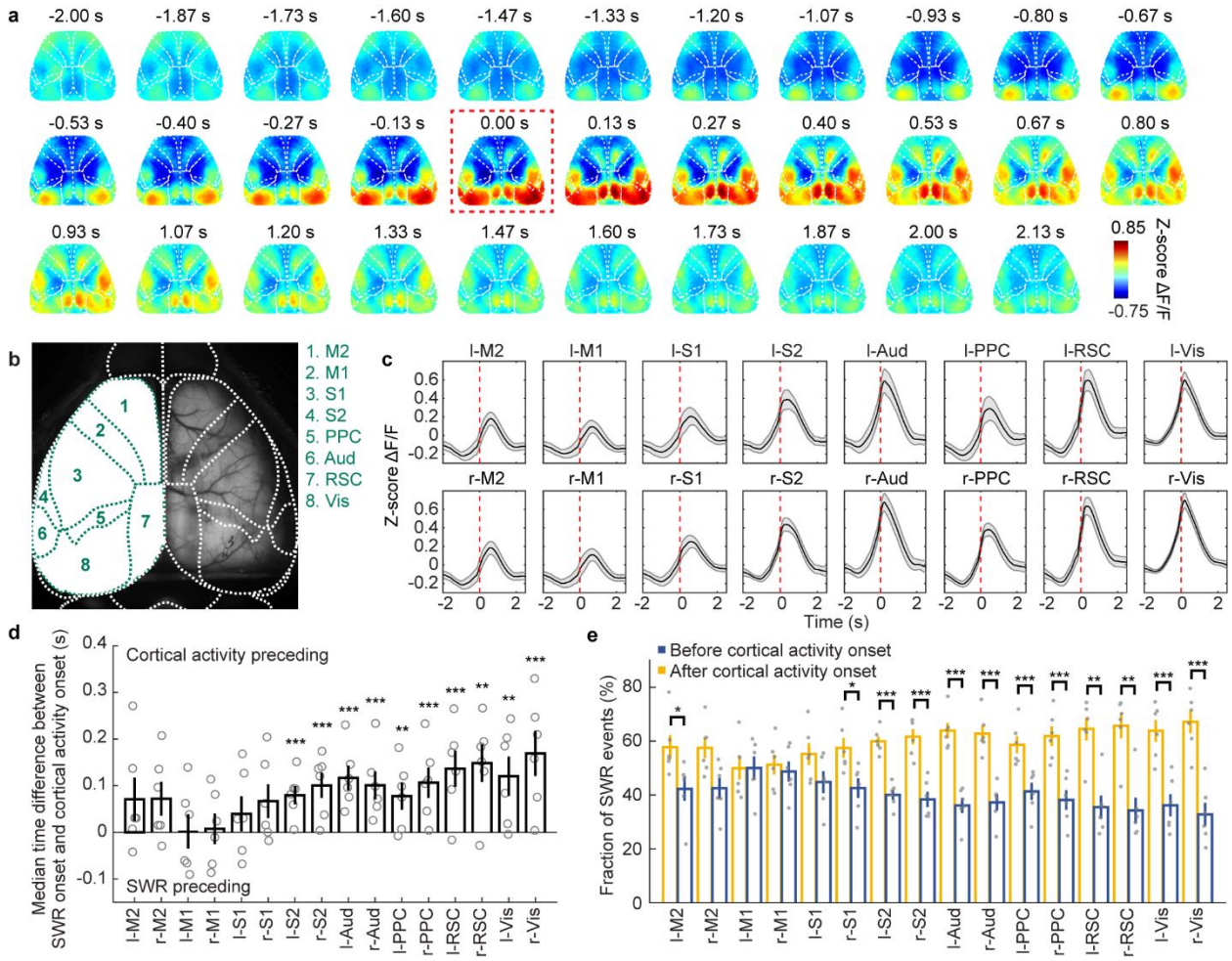
a
-2.00 s
-1.87 s
-1.73 s
-1.60 s
-1.47 s
-1.33 s
-1.20 s
-1.07 s
-0.93 s
-0.80 s
-0.67 s
-0.53 s
-0.40 s
-0.27 s
-0.13 s
0.00 s
0.13 s
0.27 s
0.40 s
0.53 s
0.67 s
0.80 s
0.93 s
1.07 s
1.20 s
1.33 s
1.47 s
1.60 s
1.73 s
1.87 s
2.00 s
2.13 s
0.85
-0.75
Z-score ΔF/F
b
1. M2
2. M1
3. S1
4. S2
5. PPC
6. Aud
7. RSC
8. Vis
c
l-M2
l-M1
l-S1
l-S2
l-Aud
l-PPC
l-RSC
l-Vis
r-M2
r-M1
r-S1
r-S2
r-Aud
r-PPC
r-RSC
r-Vis
Z-score ΔF/F
Time (s)
d
Cortical activity preceding
SWR preceding
Median time difference between SWR onset and cortical activity onset (s)
e
Before cortical activity onset
After cortical activity onset
Fraction of SWR events (%)

Figure 4. 6 Diverse SWR-associated cortical activity patterns

(a) Schematic of the TCA algorithm. The activity of 16 cortical regions during SWR events formed 3D tensors that were concatenated across mice. Using the two-stage TCA algorithm, the original data were decomposed into region, time, and event factors to capture the spatiotemporal dynamics of single SWR events. (b) Common SWR-associated cortical activity pattern templates identified across animals by the TCA algorithm. Note that patterns 1-6 exhibited activation of anterior or posterior cortical regions with 3 different time courses around SWR onsets. We defined patterns 1-3 as 'anterior patterns' and patterns 4-6 as 'posterior patterns' based on the activated cortical regions. Pattern 7 was dominated by an extended activation in visual cortex, and pattern 8 showed periodic activation in all cortical regions. (c) Correlations (corr.) of cortical activity from single SWR events with 3 of the cortical activity templates. Cortical activity during single SWR events showed a continuous distribution. (d) SWR events whose cortical activity was dominated by single cortical pattern templates were grouped separately (see text). The figure shows the average cortical activity during SWR events assigned to each template, which closely resembled the identified cortical activity templates shown in b. (e) Fraction of SWR events assigned to each cortical pattern template for all 6 animals. More SWR events were assigned to posterior patterns (patterns 4-6) than anterior patterns (patterns 1-3), suggesting the posterior regions associate with SWRs more frequently than anterior regions.

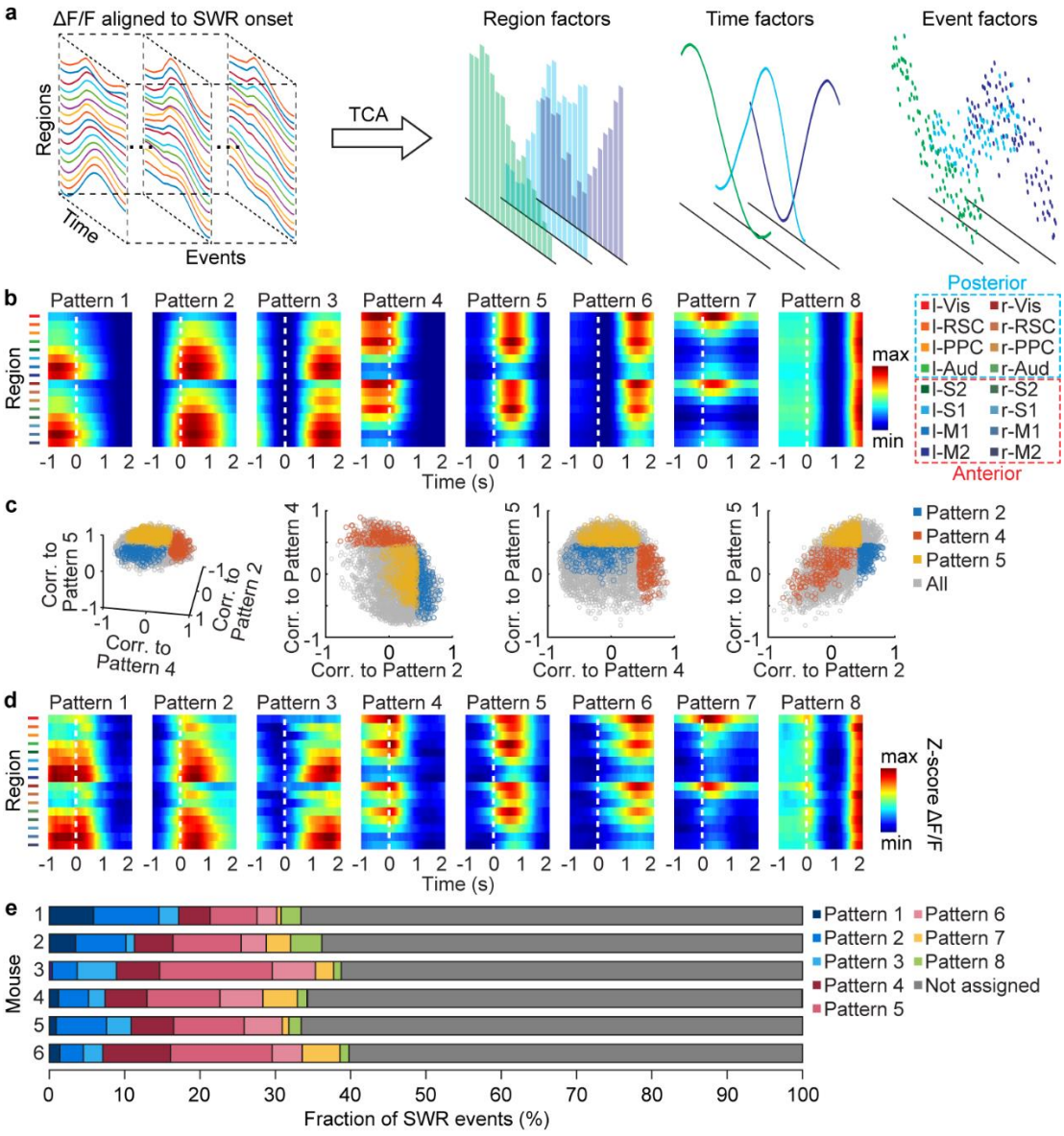
a
ΔF/F aligned to SWR onset
Regions
Time
Events
TCA
Region factors
Time factors
Event factors
b
Pattern 1
Pattern 2
Pattern 3
Pattern 4
Pattern 5
Pattern 6
Pattern 7
Pattern 8
Region
max
min
Time (s)
Posterior
l-Vis
r-Vis
l-RSC
r-RSC
l-PPC
r-PPC
l-Aud
r-Aud
l-S2
r-S2
l-S1
r-S1
l-M1
r-M1
l-M2
r-M2
Anterior
c
Corr. to Pattern 5
Corr. to Pattern 4
Corr. to Pattern 2
Pattern 2
Pattern 4
Pattern 5
All
d
Z-score ΔF/F
e
Mouse
Fraction of SWR events (%)
Pattern 1
Pattern 2
Pattern 3
Pattern 4
Pattern 5
Pattern 6
Pattern 7
Pattern 8
Not assigned

Figure 4. 7 Different cortical activity patterns associated with distinct hippocampal neuronal activity patterns during SWRs

(a) Raster plots (spikes) and the peri-event time histograms of example hippocampal neurons, showing different (Neurons 1 and 2) and similar (Neuron 3) firing rates at SWR onset under different cortical activity patterns. F.r.: firing rate. (b) Schematic of the decoding model. The firing counts of each hippocampal neuron during 0-100 ms relative to SWR onset were used as input features for the linear SVM to decode the cortical patterns. (c) Decoding accuracy of all cortical pattern pairs from one example animal (Mouse 2). Cortical pattern pairs that are significantly distinguishable based on hippocampal activity are marked by asterisks (shuffled 2000 times, one-tailed, $*P < 0.05$, $**P < 0.01$, $***P < 0.001$, see Methods for exact p values). B. acc.: balanced accuracy. (d) Fraction of distinguishable cortical pattern pairs in each animal. Across 6 animals, many cortical pattern pairs were distinguishable based on the hippocampal neuron activity. Gray lines: the chance level fraction with $P < 0.05$ (one-sided binomial test, n = 28 pattern pairs). The p-values for mouse 1-6 are 2.24E-10, 5.10E-32, 5.10E-32, 2.60E-14, 9.17E-26, 8.42E-30. (e) Preference index and decoding accuracy between anterior(A)-posterior(P) and early(E)-late(L) pattern pairs. Left: preference index of discriminant hippocampal neurons between A-P pairs (pattern 1 vs. 4, 2 vs. 5, and 3 vs. 6) or between E-L patterns (pattern 1 vs. 2, 1 vs. 3, 2 vs. 3, 4 vs. 5, 4 vs. 6, and 5 vs. 6). Posterior patterns were associated with higher firing counts of discriminant neurons than the anterior patterns (two-tailed bootstrap test, 10000 times, $**P(A\text{-}P) = 0.0017$, n = 15 pattern pairs) while no significant differences were detected between early and late patterns ($P(E\text{-}L) = 0.4646$, n = 33 pattern pairs). Gray circles: preference index averaged over all neurons for each pair within each animal. Middle: same as Left but for individual discriminant neurons (two-tailed bootstrap test, 10000 times, $***P(A\text{-}P) = 0.0001$, n = 56 neurons, $P(E\text{-}L) = 0.3802$, n = 160 neurons). Gray dots: preference index of individual discriminant neurons. Right: Decoding accuracy between A-P and E-L pairs was similar (two-tailed bootstrap test, 10000 times, $P = 0.0656$, n = 15 pattern pairs for A-P, n = 33 pattern pairs for E-L). All error bars are s.e.m. Gray circles: decoding accuracy for each pair.

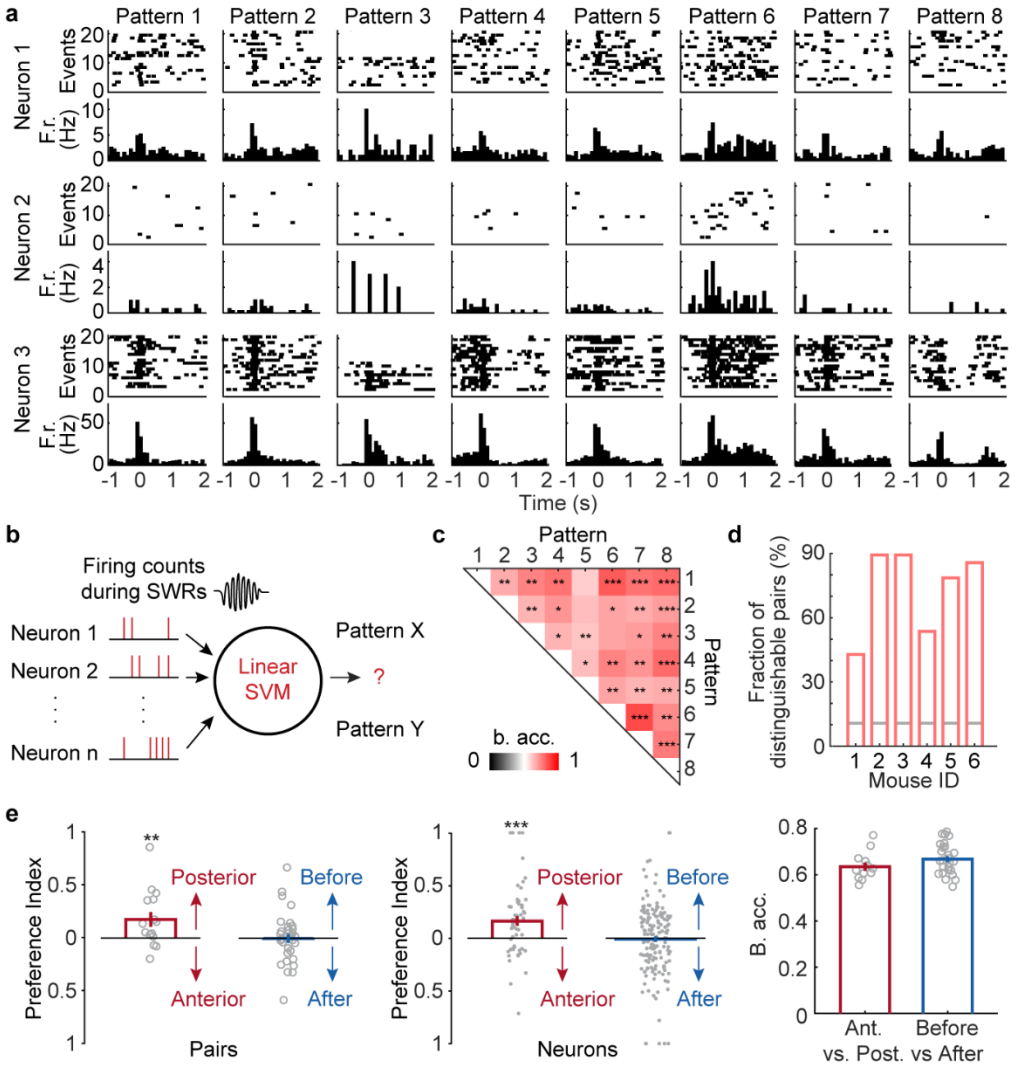
a
Pattern 1
Pattern 2
Pattern 3
Pattern 4
Pattern 5
Pattern 6
Pattern 7
Pattern 8
Neuron 1
Neuron 2
Neuron 3
Events
F.r. (Hz)
Time (s)
b
Firing counts during SWRs
Neuron 1
Neuron 2
Neuron n
Linear SVM
Pattern X
Pattern Y
?
c
Pattern
b. acc.
d
Fraction of distinguishable pairs (%)
Mouse ID
e
Preference Index
Posterior
Anterior
Before
After
Pairs
Neurons
B. acc.
Ant. vs. Post.
Before vs After

4.8 Supplementary Information

Figure 4. S 1 Microscope pictures of different Neuro-FITM probe designs.

(a) Microscope image of the recording tip of 32 channel Neuro-FITM array with 20 μm spacing. (b) Same as (a), but for 64 channel Neuro-FITM array with 20 μm spacing. (c) Picture of the whole probe (left), the microscope pictures of the recording tip of 32 channel Neuro-FITM array with 100 μm spacing (middle) and 20 μm spacing (right) for recording in rats. (d) Same as c, but for 32 channel Neuro-FITM array with 100 μm spacing and 50 μm spacing for recording in primates.

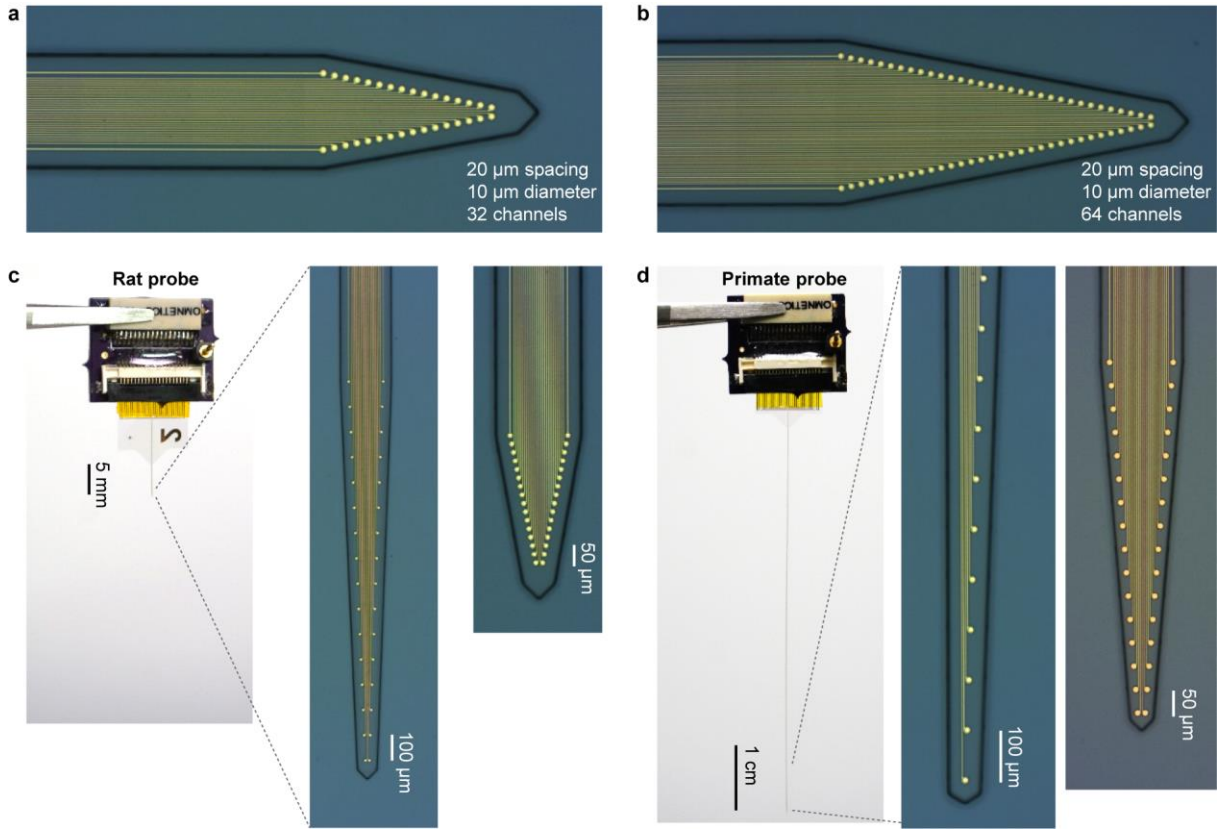
a
20 µm spacing
10 µm diameter
32 channels
b
20 µm spacing
10 µm diameter
64 channels
c
Rat probe
5 mm
100 µm
50 µm
d
Primate probe
1 cm
100 µm
50 µm

Figure 4. S 2 Testing the multimodal recording setup using Neuro-FITM and standard silicon probes under both the wide-field and 2-photon imaging systems.

(a) A picture of the probes tested in the multimodal recording setup. (b) Pictures of the side view under the 2-photon imaging system. Neuro-FITM can be completely bent to the side as shown with the blue dashed line. Both the Neuronexus probes and the Neuropixel probe prevent the lowering of microscope objective (total rigid part indicated by red double arrow). The right column are the 2-photon images of the array surface, showing the thin Au wires, the boundary of the array substrate, and the penetration point. (c) Pictures of the experimental setup (top), the zoom-in side view (middle), and the field of view (bottom) under wide-field imaging system, showing the blocking of field of view (Neuronexus probes) and preventing the lowering of microscope objective (Neuropixel probe). Wide-field image shows that mostly transparent Neuro-FITM does not block the field of view or generate shadows.

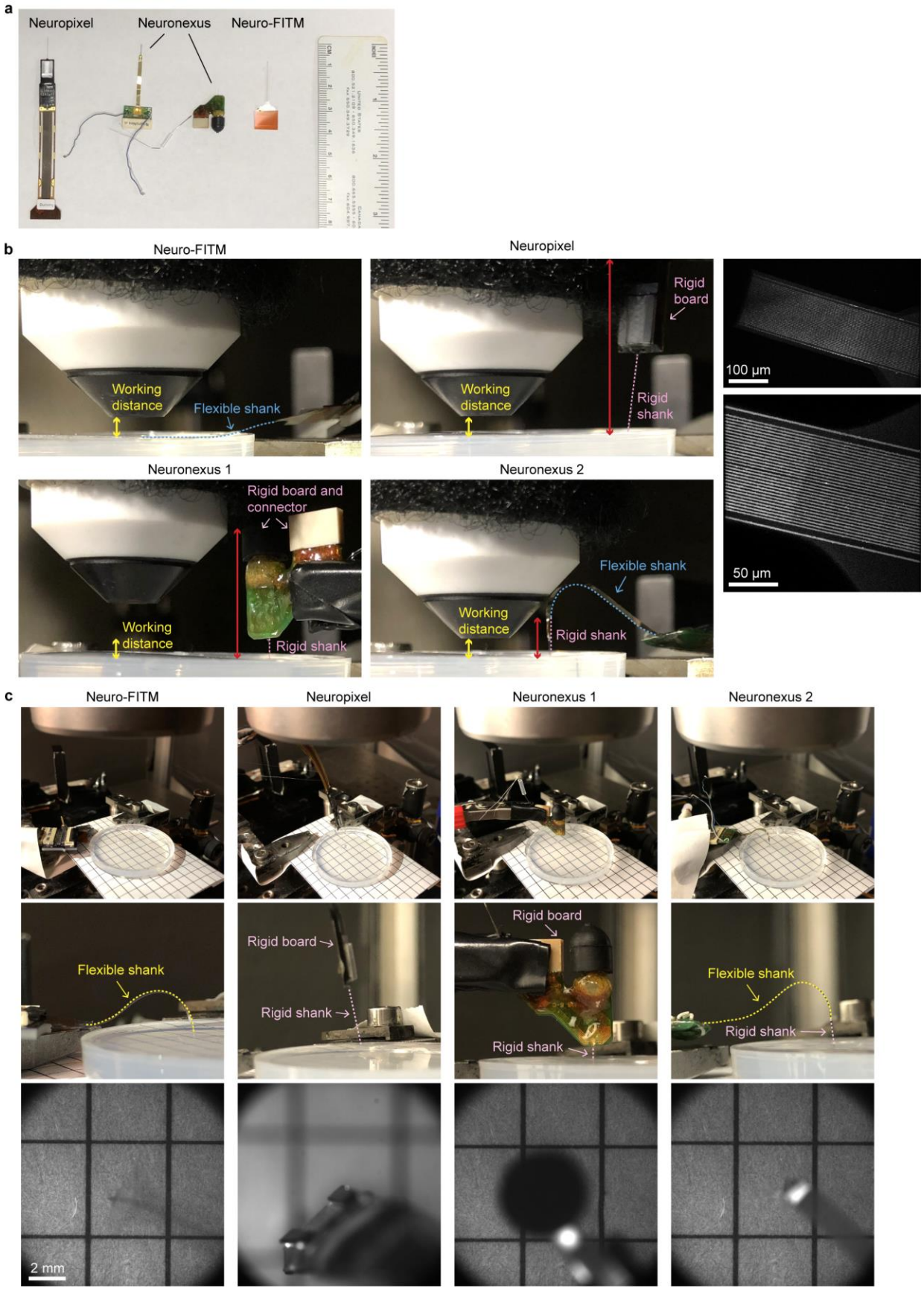
a
Neuropixel
Neuronexus
Neuro-FITM
b
Neuro-FITM
Neuropixel
Working distance
Flexible shank
Rigid board
Rigid shank
100 µm
50 µm
Neuronexus 1
Neuronexus 2
Rigid board and connector
Working distance
Rigid shank
Flexible shank
Working distance
Rigid shank
c
Neuro-FITM
Neuropixel
Neuronexus 1
Neuronexus 2
Flexible shank
Rigid board
Rigid shank
Rigid board
Rigid shank
Flexible shank
Rigid shank
2 mm

Figure 4. S 3 Implantation of Neuro-FITM array to HPC in in vivo experiments and the spike waveforms of example neurons.

(a) Surgical setup of array implantation in actual experiments. Note that the array shank is largely invisible. The edge of the shank is marked by yellow dashed lines. (b) The staining results of 6 mice, showing the successful penetration to the CA1 pyramidal layer. Arrowheads: trajectory in CA1 pyramidal layer. (c) The spike waveforms of a few example neurons recorded from different animals. Single neurons can be detected in multiple adjacent channels, each exhibiting different waveform amplitudes.

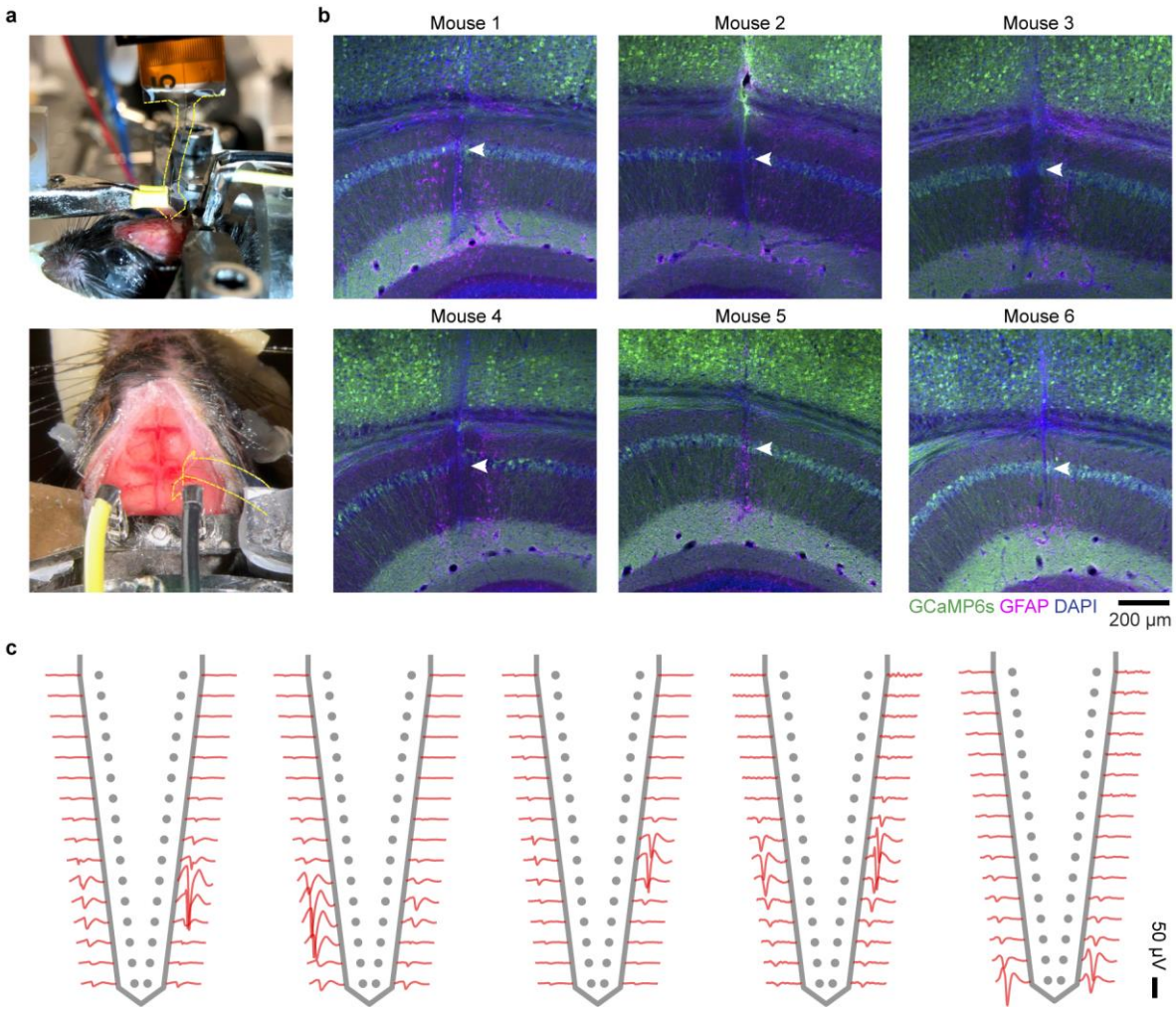
a
b
Mouse 1
Mouse 2
Mouse 3
Mouse 4
Mouse 5
Mouse 6
GCaMP6s GFAP DAPI
200 µm
c
50 µV

Figure 4. S 4 SWR-associated large-scale cortical activity.

(a) Averaged cortical activity aligned to SWR onset in each animal. In all animals, the cortex exhibited broad activation around SWRs with the cortical activity rising before SWR onset. (b) Mean activity in each cortical region aligned to SWR onset (mean ± s.e.m., across SWR events). Black dashed lines: SWR onset.

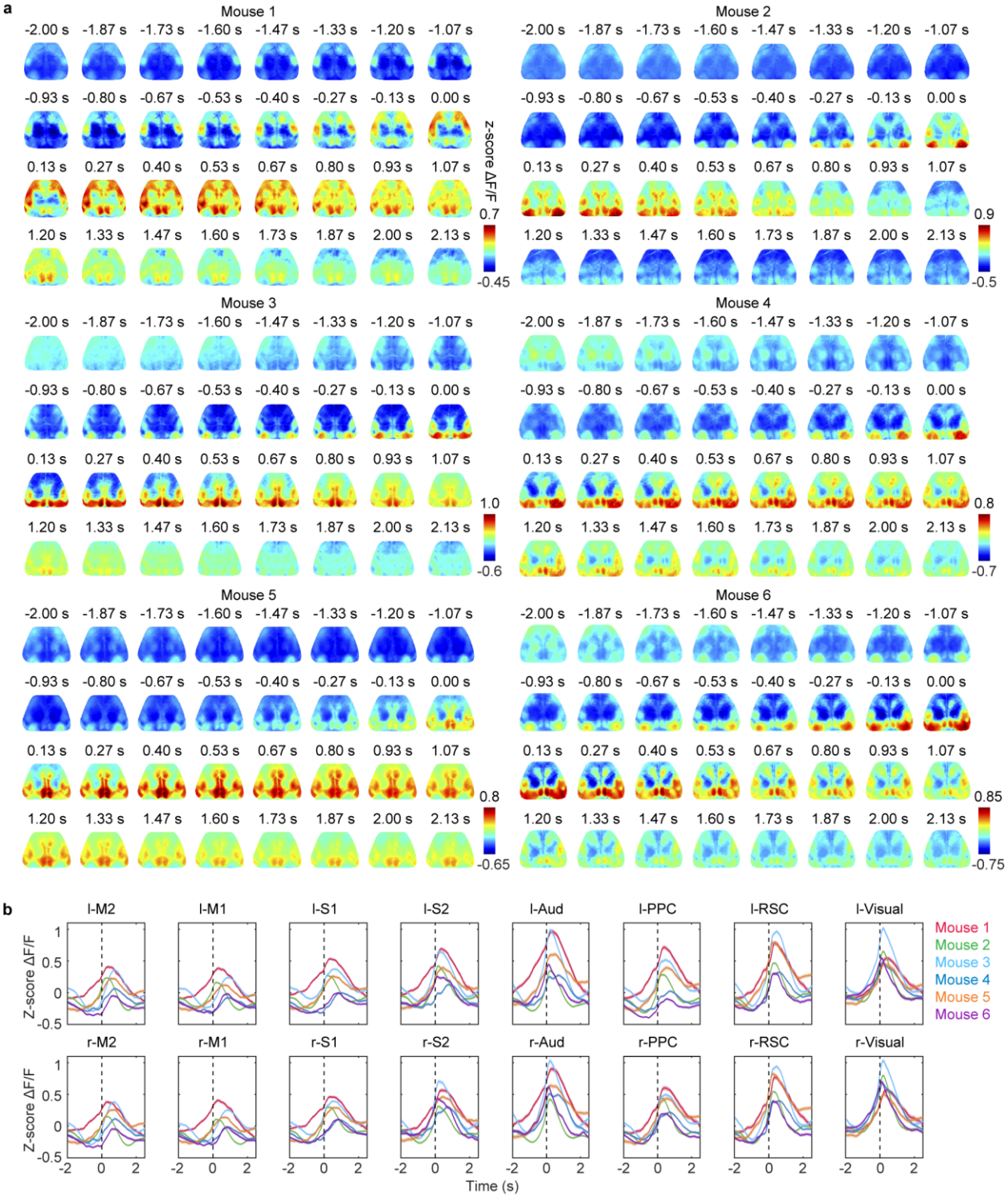
a
Mouse 1
Mouse 2
Mouse 3
Mouse 4
Mouse 5
Mouse 6
-2.00 s
-1.87 s
-1.73 s
-1.60 s
-1.47 s
-1.33 s
-1.20 s
-1.07 s
-0.93 s
-0.80 s
-0.67 s
-0.53 s
-0.40 s
-0.27 s
-0.13 s
0.00 s
0.13 s
0.27 s
0.40 s
0.53 s
0.67 s
0.80 s
0.93 s
1.07 s
1.20 s
1.33 s
1.47 s
1.60 s
1.73 s
1.87 s
2.00 s
2.13 s
z-score ΔF/F
0.7
-0.45
0.9
-0.5
1.0
-0.6
0.8
-0.7
0.8
-0.65
0.85
-0.75
b
l-M2
l-M1
l-S1
l-S2
l-Aud
l-PPC
l-RSC
l-Visual
r-M2
r-M1
r-S1
r-S2
r-Aud
r-PPC
r-RSC
r-Visual
Z-score ΔF/F
1
0.5
0
-0.5
-2
0
2
Time (s)
Mouse 1
Mouse 2
Mouse 3
Mouse 4
Mouse 5
Mouse 6

Figure 4. S 5 The distribution of time differences between SWR onset and activity onset in each cortical region.

The time differences (SWR onset-cortical activity onset: positive = cortex precedes SWR) formed a continuum around cortical activity onset. Note that the distribution was skewed to positive side in posterior cortical regions, suggesting cortical activity onset in posterior regions preceded SWR onset in a larger fraction of SWR events. Black lines: cortical activity onset.


Mouse 1
Mouse 2
Mouse 3
Mouse 4
Mouse 5
Mouse 6
l-M2
r-M2
l-S1
r-S1
l-S2
r-S2
l-Aud
r-Aud
l-PPC
r-PPC
l-RSC
r-RSC
l-Vis
r-Vis
Fraction of SWR events (%)
Time differences between SWR onset and cortical activity onset (s)

Figure 4. S 6 Two-stage TCA algorithm.

(a) Schematic of algorithm flow. (b) Reconstruction error (rec. error) under different ranks of TCA model. (c) The adjacency matrix before and after clustering. The 1500 TCA patterns were obtained by the 100 runs of 15th order TCA with random initialization. Corr.: correlation. (d) Number of assigned patterns in each cluster. Note that only the first 8 clusters had number of assigned patterns > 1. (e) Reconstruction error (rec. error) of the original TCA algorithm with random initialization and the two-stage TCA algorithm with refined initialization (rank = 8). The reconstruction error given by the two-stage TCA model is smaller than that of the original TCA algorithm with random initialization (two-tailed rank-sum test, P=1.38E-11, n = 100 repetitions for each algorithm), indicating that our two-stage TCA better captured the dynamics of cortical activity. (f) Randomly selected 20 TCA patterns in each cluster for clusters 1-8. Patterns within each cluster exhibited similar spatiotemporal properties.

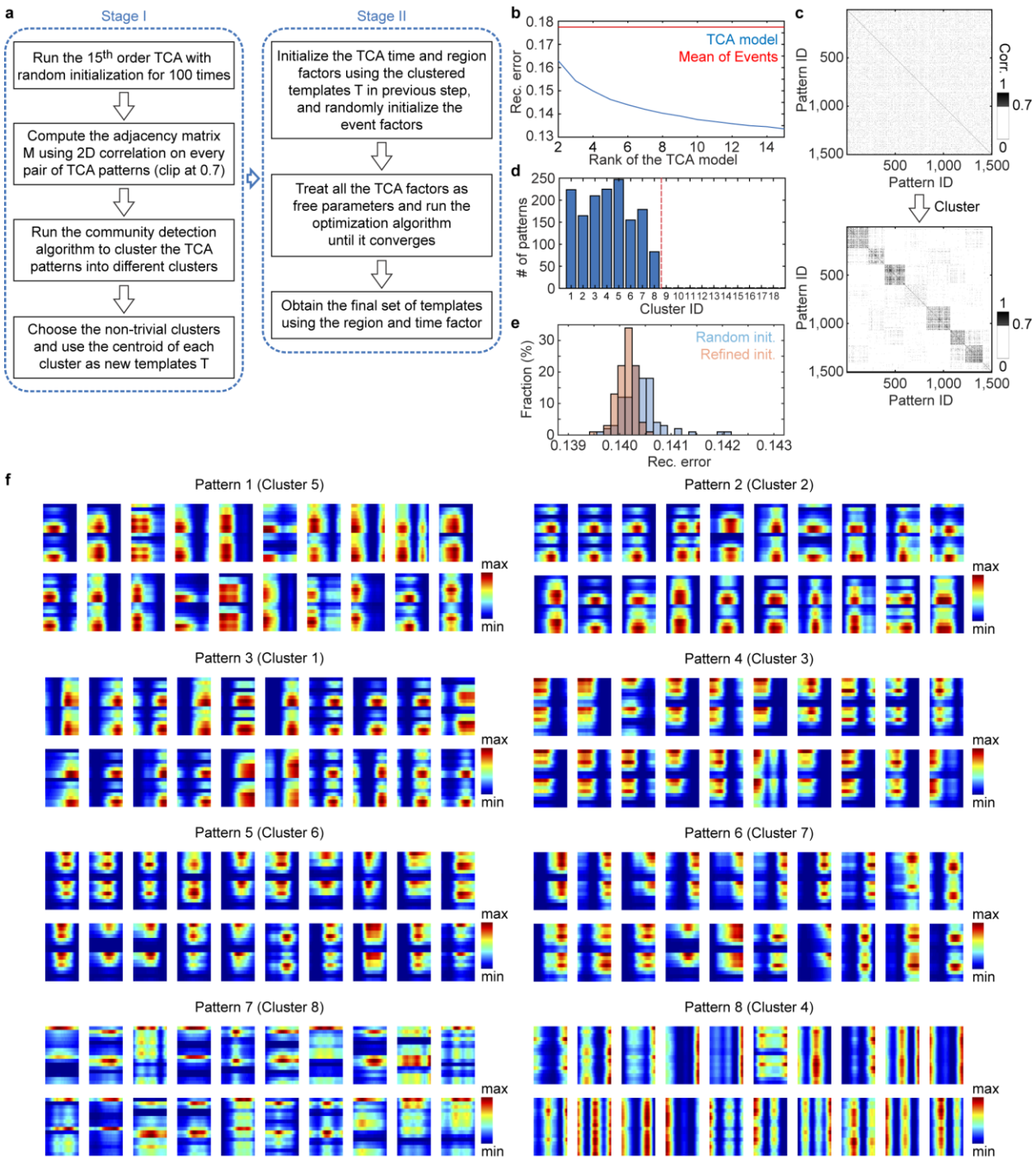
a
Stage I
Run the 15th order TCA with random initialization for 100 times
Compute the adjacency matrix M using 2D correlation on every pair of TCA patterns (clip at 0.7)
Run the community detection algorithm to cluster the TCA patterns into different clusters
Choose the non-trivial clusters and use the centroid of each cluster as new templates T
Stage II
Initialize the TCA time and region factors using the clustered templates T in previous step, and randomly initialize the event factors
Treat all the TCA factors as free parameters and run the optimization algorithm until it converges
Obtain the final set of templates using the region and time factor
b
Rec. error
TCA model
Mean of Events
Rank of the TCA model
c
Pattern ID
Corr.
Cluster
d
# of patterns
Cluster ID
e
Fraction (%)
Random init.
Refined init.
Rec. error
f
Pattern 1 (Cluster 5)
Pattern 2 (Cluster 2)
Pattern 3 (Cluster 1)
Pattern 4 (Cluster 3)
Pattern 5 (Cluster 6)
Pattern 6 (Cluster 7)
Pattern 7 (Cluster 8)
Pattern 8 (Cluster 4)
max
min

Figure 4. S 7 The two-stage TCA result and the cortical activation timing analysis for two patterns.

(a) Factors generated by two-stage TCA algorithm. The high-dimensional data of SWR-associated activity from 16 cortical regions was decomposed into 3 factors. The region factors and time factors describe the spatial and temporal dynamics of cortical patterns respectively and the event factors measure the weighting of a given SWR event on the established set of patterns. (b) Cortical activation timing for pattern 2 and pattern 5. Shown in each row are the pattern template (left), the average cortical activity for the events assigned to the pattern (middle), and the P-value maps (right) for all the cortical regions at [-1 s, 2 s] time interval aligned to SWR onset, showing significantly higher activity than baseline (-1 s) for most cortical regions.

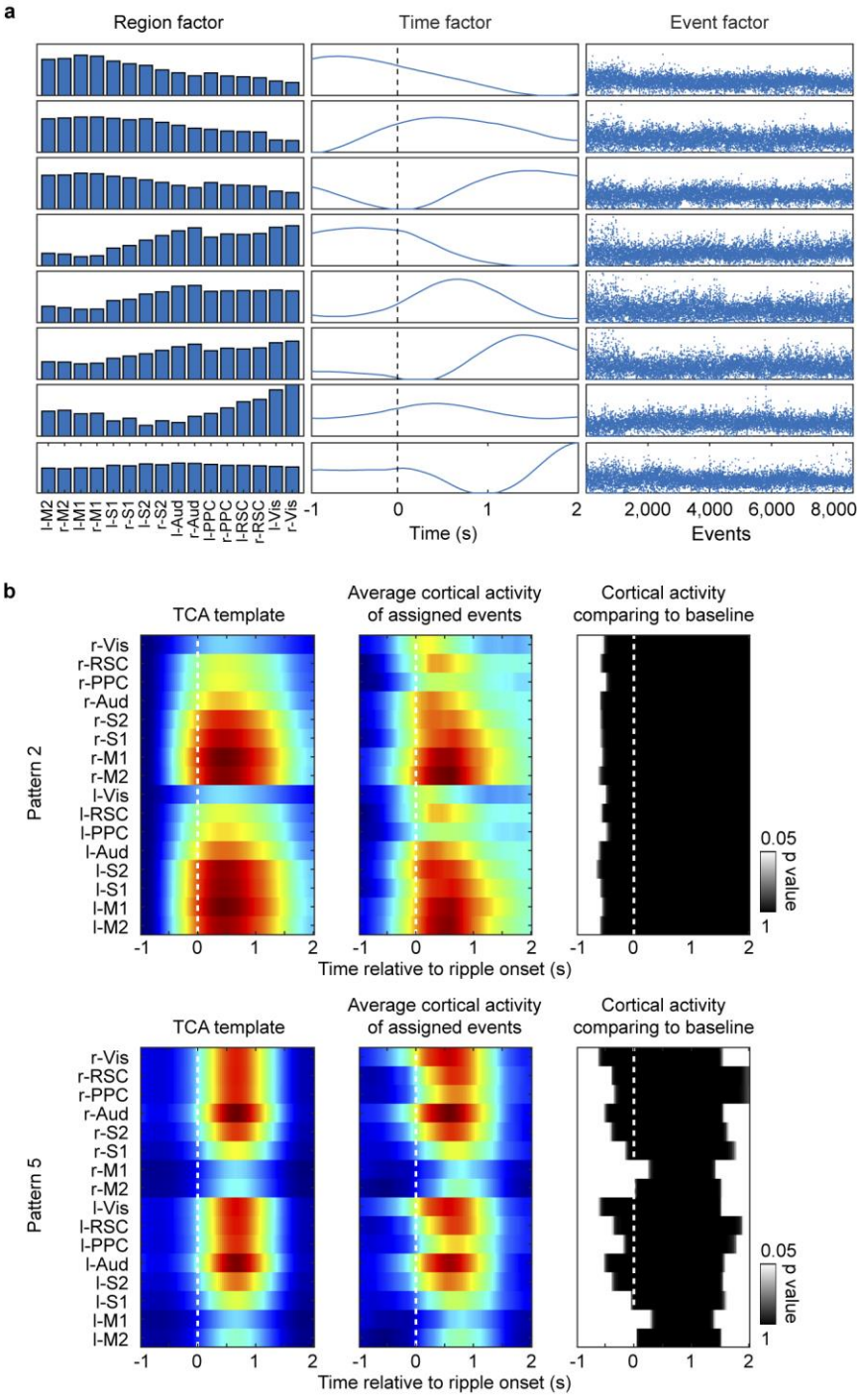
a
Region factor
Time factor
Event factor
l-M2
r-M2
l-M1
r-M1
l-S1
r-S1
l-S2
r-S2
l-Aud
r-Aud
l-PPC
r-PPC
l-RSC
r-RSC
l-Vis
r-Vis
-1
0
1
2
Time (s)
2,000
4,000
6,000
8,000
Events
b
TCA template
Average cortical activity of assigned events
Cortical activity comparing to baseline
Pattern 2
r-Vis
r-RSC
r-PPC
r-Aud
r-S2
r-S1
r-M1
r-M2
l-Vis
l-RSC
l-PPC
l-Aud
l-S2
l-S1
l-M1
l-M2
0.05
p value
1
Time relative to ripple onset (s)
Pattern 5

Figure 4. S 8 The decoding accuracy of all cortical pattern pairs in each animal.

Many cortical pattern pairs can be distinguished from each other in each animal. The distinguishable pattern pairs are marked by asterisks (shuffling 2000 times, one-tailed, $*P < 0.05$, $**P < 0.01$, $***P < 0.001$, see Methods for exact p values). B. acc.: balanced accuracy.

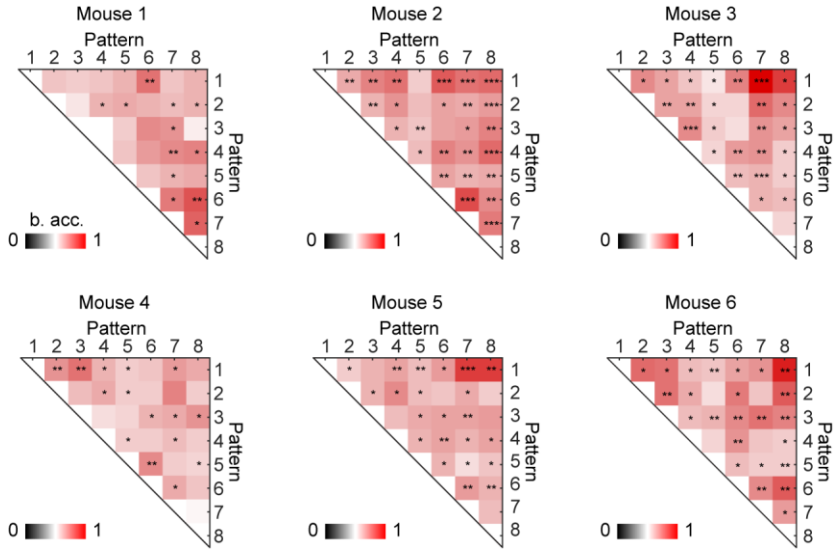
Mouse 1
Mouse 2
Mouse 3
Mouse 4
Mouse 5
Mouse 6
Pattern
1 2 3 4 5 6 7 8
b. acc.
0
1

Figure 4. S 9 Discriminant neurons in decoding cortical pattern identity and the fraction of distinguishable pairs using different neuron populations.

(a) Discriminant neurons selected by feature elimination algorithm in decoding for each pattern pair. Note that the decoding often requires information from multiple HPC neurons, and all HPC neurons contributed to the decoding of some pattern pairs. (b) The decoding results of cortical patterns using both the PYR and INT, the PYR only, and the INT only. Gray lines: the chance level fraction with $P < 0.05$. The chance level number of decodable pattern pairs (nc) was computed from the inverse of binomial cumulative distribution with probability 0.95 (one-sided binomial test, n = 28 pattern pairs). The chance level fraction was obtained by dividing nc with n = 28, the number of pattern pairs on which decoding was performed. PYR: pyramidal neurons, INT: interneurons. For PYR + INT, the p-values for mouse 1-6 are 2.24E-10, 5.10E-32, 5.10E-32, 2.60E-14, 9.17E-26, 8.42E-30. For PYR only, the p-values for mouse 1-6 are 1.26E-11, 8.42E-30, 9.63E-16, 0.16, 5.56E-7, 2.60E-14. For INT only, the p-values for mouse 1-6 are 0.76, 0.0023, 2.60E-14, 5.56E-7, 4.92E-5, 4.92E-5.

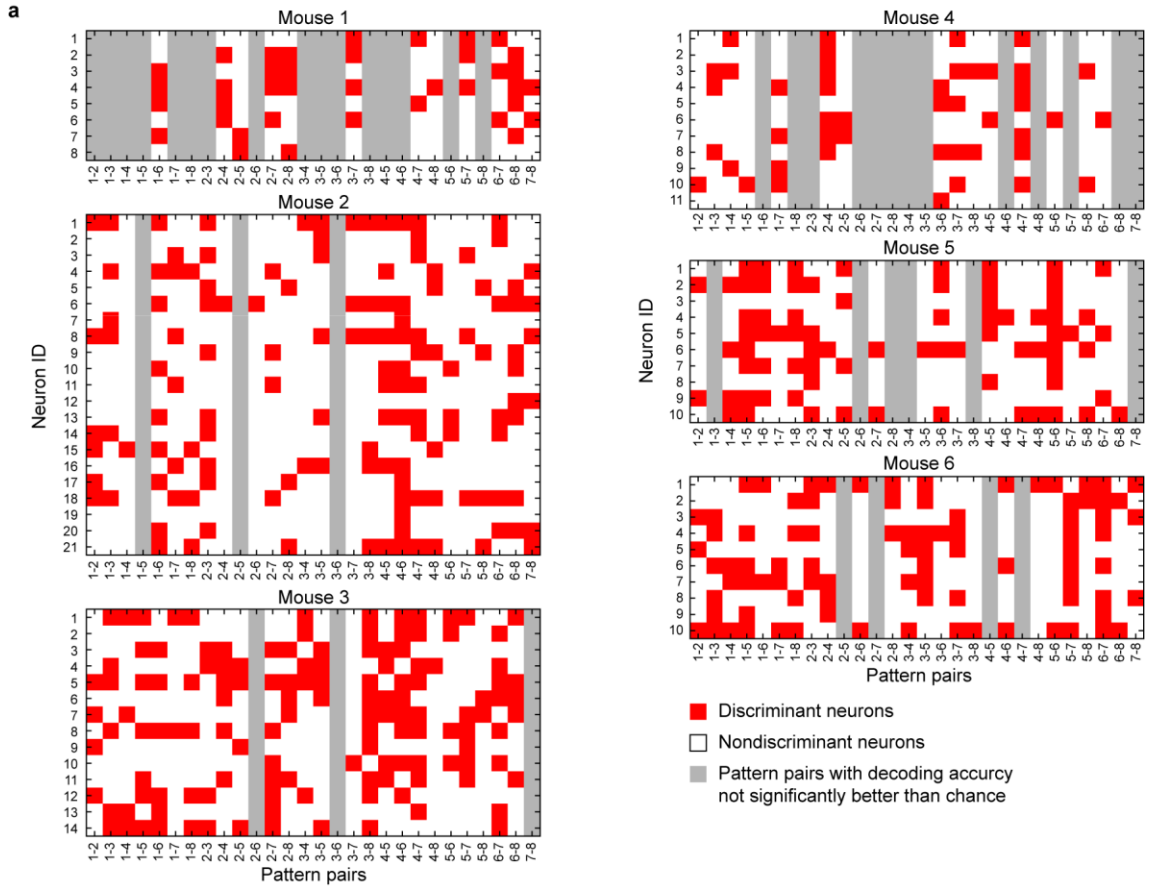
a
Mouse 1
Mouse 2
Mouse 3
Mouse 4
Mouse 5
Mouse 6
Neuron ID
Pattern pairs
Discriminant neurons
Nondiscriminant neurons
Pattern pairs with decoding accurcy not significantly better than chance

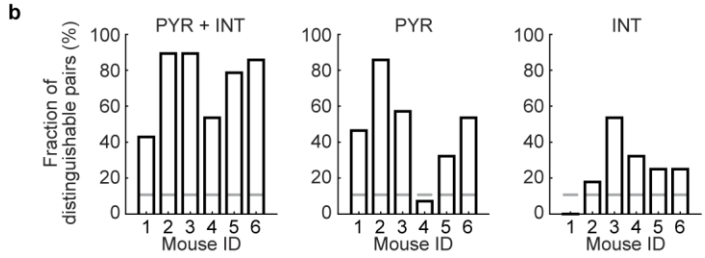
b
PYR + INT
PYR
INT
Fraction of distinguishable pairs (%)
Mouse ID

Figure 4. S 10 Different cortical activity patterns associated with distinct HPC neuronal activity patterns during all SWRs.

(a) Raster plots (spikes) and the peri-event time histograms of example HPC neurons. (b) Decoding accuracy of all cortical pattern pairs from all 6 animals. Cortical pattern pairs that are significantly distinguishable based on hippocampus activity are marked by asterisks (shuffled 2000 times, one-tailed, $*P < 0.05$, $**P < 0.01$, $***P < 0.001$, see Methods for exact p values). B. acc.: balanced accuracy. (c) Fraction of distinguishable cortical pattern pairs in each animal. Gray lines: the chance level fraction with $P < 0.05$. The p-values for mouse 1-6 are 6.13E-13, 1.99E-34, 1.00E-27, 2.60E-14, 4.73E-8, 9.17E-26, n = 28 pattern pairs. (d) Preference index and decoding accuracy between anterior (A)-posterior (P) and early (E) - late (L) pattern pairs. Left: preference index of discriminant hippocampus neurons between A-P pairs (pattern 1 vs. 4, 2 vs. 5, and 3 vs. 6) or between E-L patterns (pattern 1 vs. 2, 1 vs. 3, 2 vs. 3, 4 vs. 5, 4 vs. 6, and 5 vs. 6). Posterior patterns were associated with higher firing counts of discriminant neurons than the anterior patterns (two-tailed bootstrap test, 10000 times, *** $P(A\text{-}P)$= 0.0005, n = 16 pattern pairs) while no significant differences were detected between early and late patterns ($P(E\text{-}L)$ = 0.4380, n = 27 pattern pairs). Gray circles: preference index averaged over all neurons for each pair within each animal. Middle: same as Left but for individual discriminant neurons (two-tailed bootstrap test, 10000 times, *** $P(A\text{-}P)$ = 0, n = 71 neurons, $P(E\text{-}L)$ = 0.3591, n = 129 neurons). Gray dots: preference index of individual discriminant neurons. Right: Decoding accuracy between A-P and E-L pairs was similar (two-tailed bootstrap test, 10000 times, P = 0.4745, n = 16 pattern pairs for A-P, n = 27 pattern pairs for E-L). All error bars are s.e.m. Gray circles: decoding accuracy for each pair.

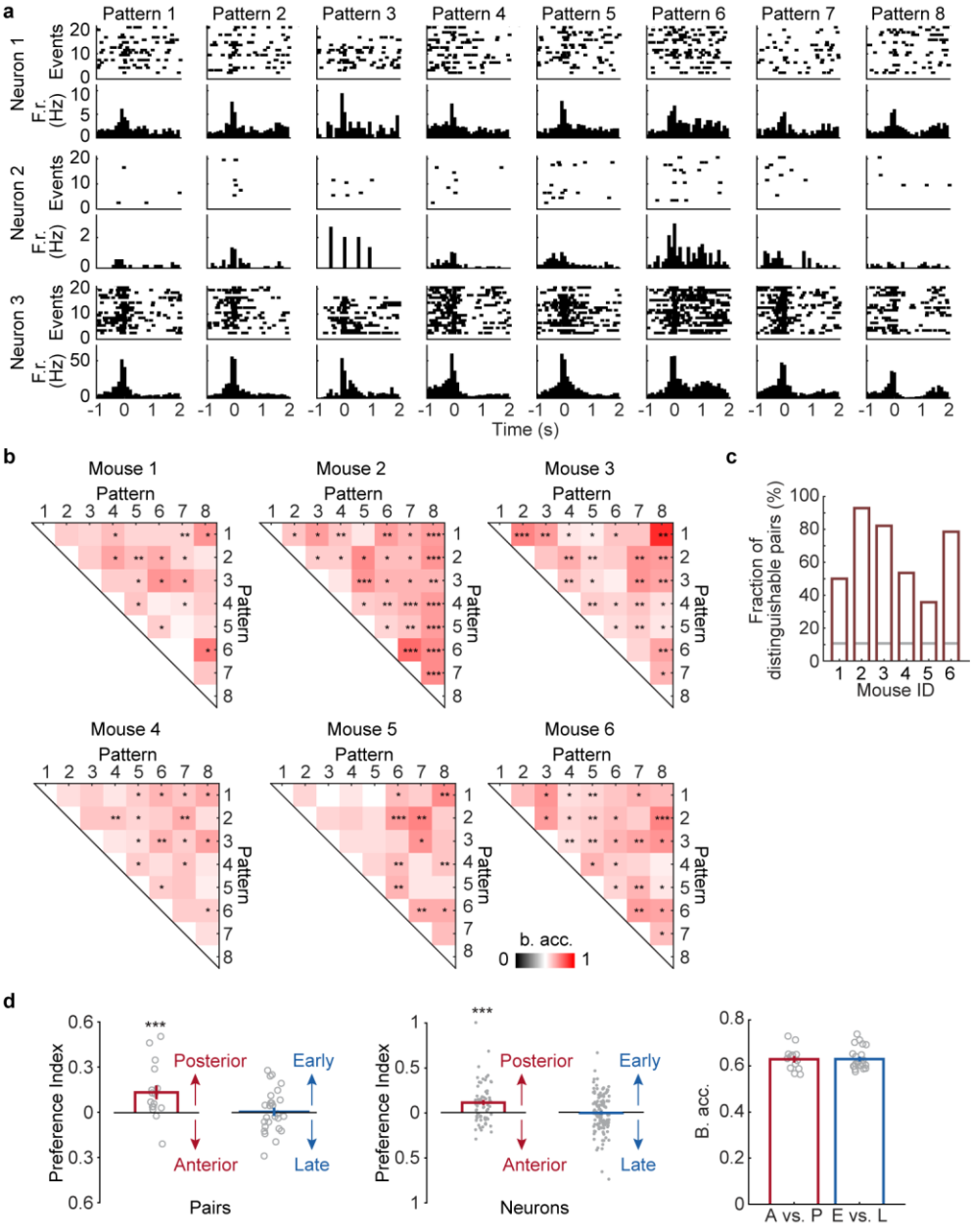
a
Pattern 1
Pattern 2
Pattern 3
Pattern 4
Pattern 5
Pattern 6
Pattern 7
Pattern 8
Neuron 1
Neuron 2
Neuron 3
Events
F.r. (Hz)
Time (s)
b
Mouse 1
Mouse 2
Mouse 3
Mouse 4
Mouse 5
Mouse 6
Pattern
b. acc.
c
Fraction of distinguishable pairs (%)
Mouse ID
d
Preference Index
Posterior
Anterior
Early
Late
Pairs
Neurons
B. acc.
A vs. P
E vs. L

4.9 References

1 Skelin, I., Kilianski, S. & McNaughton, B. L. Hippocampal coupling with cortical and subcortical structures in the context of memory consolidation. *Neurobiology of learning and memory* **160**, 21-31 (2019).

2 Buzsáki, G. Hippocampal sharp wave-ripple: A cognitive biomarker for episodic memory and planning. *Hippocampus* **25**, 1073-1188 (2015).

3 Todorova, R. & Zugaro, M. Hippocampal ripples as a mode of communication with cortical and subcortical areas. *Hippocampus* **30**, 39-49 (2020).

4 Logothetis, N. K., Eschenko, O., Murayama, Y., Augath, M., Steudel, T., Evrard, H., Besserve, M. & Oeltermann, A. Hippocampal–cortical interaction during periods of subcortical silence. *Nature* **491**, 547-553 (2012).

5 Jadhav, S. P., Kemere, C., German, P. W. & Frank, L. M. Awake hippocampal sharp-wave ripples support spatial memory. *Science* **336**, 1454-1458 (2012).

6 Maingret, N., Girardeau, G., Todorova, R., Goutierre, M. & Zugaro, M. Hippocampo-cortical coupling mediates memory consolidation during sleep. *Nature neuroscience* **19**, 959-964 (2016).

7 Girardeau, G., Benchenane, K., Wiener, S. I., Buzsáki, G. & Zugaro, M. B. Selective suppression of hippocampal ripples impairs spatial memory. *Nature neuroscience* **12**, 1222 (2009).

8 Sirota, A., Csicsvari, J., Buhl, D. & Buzsáki, G. Communication between neocortex and hippocampus during sleep in rodents. *Proceedings of the National Academy of Sciences* **100**, 2065-2069 (2003).

9 Rothschild, G., Eban, E. & Frank, L. M. A cortical–hippocampal–cortical loop of information processing during memory consolidation. *Nature neuroscience* **20**, 251-259 (2017).

10 Ji, D. & Wilson, M. A. Coordinated memory replay in the visual cortex and hippocampus during sleep. *Nature neuroscience* **10**, 100-107 (2007).

11 Jadhav, S. P., Rothschild, G., Roumis, D. K. & Frank, L. M. Coordinated excitation and inhibition of prefrontal ensembles during awake hippocampal sharp-wave ripple events. *Neuron* **90**, 113-127 (2016).

12 Chrobak, J. & Buzsáki, G. Selective activation of deep layer (V-VI) retrohippocampal cortical neurons during hippocampal sharp waves in the behaving rat. *Journal of Neuroscience* **14**, 6160-6170 (1994).

13 Williams, A. H., Kim, T. H., Wang, F., Vyas, S., Ryu, S. I., Shenoy, K. V., Schnitzer, M., Kolda, T. G. & Ganguli, S. Unsupervised discovery of demixed, low-dimensional neural dynamics across multiple timescales through tensor component analysis. *Neuron* **98**, 1099-1115. e1098 (2018).

14 Cortes, C. & Vapnik, V. Support-vector networks. *Machine learning* **20**, 273-297 (1995).

15 Won, S. M., Song, E., Zhao, J., Li, J., Rivnay, J. & Rogers, J. A. Recent advances in materials, devices, and systems for neural interfaces. *Advanced Materials* **30**, 1800534 (2018).

16 Thunemann, M., Lu, Y., Liu, X., Kılıç, K., Desjardins, M., Vandenberghe, M., Sadegh, S., Saisan, P. A., Cheng, Q., Weldy, K. L., Lyu, H., Djurovic, S., Andreassen, O. A., Dale, A. M., Devor, A. & Kuzum, D. Deep 2-photon imaging and artifact-free optogenetics through transparent graphene microelectrode arrays. *Nature Communications* **9**, 2035 (2018).

17 Lu, Y., Liu, X., Hattori, R., Ren, C., Zhang, X., Komiyama, T. & Kuzum, D. Ultralow impedance graphene microelectrodes with high optical transparency for simultaneous deep two-photon imaging in transgenic mice. *Advanced Functional Materials* **28**, 1800002 (2018).

18 Jun, J. J., Steinmetz, N. A., Siegle, J. H., Denman, D. J., Bauza, M., Barbarits, B., Lee, A. K., Anastassiou, C. A., Andrei, A. & Aydın, Ç. Fully integrated silicon probes for high-density recording of neural activity. *Nature* **551**, 232-236 (2017).

19 Kuzum, D., Takano, H., Shim, E., Reed, J. C., Juul, H., Richardson, A. G., De Vries, J., Bink, H., Dichter, M. A. & Lucas, T. H. Transparent and flexible low noise graphene electrodes for simultaneous electrophysiology and neuroimaging. *Nature communications* **5**, 5259 (2014).

20 Wekselblatt, J. B., Flister, E. D., Piscopo, D. M. & Niell, C. M. Large-scale imaging of cortical dynamics during sensory perception and behavior. *Journal of neurophysiology* (2016).

21 Makino, H., Ren, C., Liu, H., Kim, A. N., Kondapaneni, N., Liu, X., Kuzum, D. & Komiyama, T. Transformation of Cortex-wide Emergent Properties during Motor Learning. *Neuron* **94**, 880-890. e888 (2017).

22 Shobe, J. L., Claar, L. D., Parhami, S., Bakhurin, K. I. & Masmanidis, S. C. Brain activity mapping at multiple scales with silicon microprobes containing 1,024 electrodes. *Journal of neurophysiology* **114**, 2043-2052 (2015).

23 Yang, Y., Liu, N., He, Y., Liu, Y., Ge, L., Zou, L., Song, S., Xiong, W. & Liu, X. Improved calcium sensor GCaMP-X overcomes the calcium channel perturbations induced by the calmodulin in GCaMP. *Nature communications* **9**, 1-18 (2018).

24 Chu, M. W., Li, W. L. & Komiyama, T. Balancing the robustness and efficiency of odor representations during learning. *Neuron* **92**, 174-186 (2016).

25 Cichy, R. M., Pantazis, D. & Oliva, A. Resolving human object recognition in space and time. *Nature neuroscience* **17**, 455 (2014).

26 Kamitani, Y. & Tong, F. Decoding the visual and subjective contents of the human brain. *Nature neuroscience* **8**, 679-685 (2005).

27 Yan, Y., Rasch, M. J., Chen, M., Xiang, X., Huang, M., Wu, S. & Li, W. Perceptual training continuously refines neuronal population codes in primary visual cortex. *Nature neuroscience* **17**, 1380-1387 (2014).

28 Morcos, A. S. & Harvey, C. D. History-dependent variability in population dynamics during evidence accumulation in cortex. *Nature neuroscience* **19**, 1672-1681 (2016).

29 Guyon, I., Weston, J., Barnhill, S. & Vapnik, V. Gene selection for cancer classification using support vector machines. *Machine learning* **46**, 389-422 (2002).

30 Xu, H., Hirschberg, A. W., Scholten, K., Berger, T. W., Song, D. & Meng, E. Acute in vivo testing of a conformal polymer microelectrode array for multi-region hippocampal recordings. *Journal of neural engineering* **15**, 016017 (2018).

31 Fiáth, R., Hofer, K. T., Csikós, V., Horváth, D., Nánási, T., Tóth, K., Pothof, F., Böhler, C., Asplund, M. & Ruther, P. Long-term recording performance and biocompatibility of chronically implanted cylindrically-shaped, polymer-based neural interfaces. *Biomedical Engineering/Biomedizinische Technik* **63**, 301-315 (2018).

32 Yin, M., Borton, D. A., Komar, J., Agha, N., Lu, Y., Li, H., Laurens, J., Lang, Y., Li, Q. & Bull, C. Wireless neurosensor for full-spectrum electrophysiology recordings during free behavior. *Neuron* **84**, 1170-1182 (2014).

33 Kim, C., Park, J., Ha, S., Akinin, A., Kubendran, R., Mercier, P. P. & Cauwenberghs, G. A 3 mm× 3 mm fully integrated wireless power receiver and neural interface system-on-chip. *IEEE transactions on biomedical circuits and systems* **13**, 1736-1746 (2019).

34 Zhou, A., Santacruz, S. R., Johnson, B. C., Alexandrov, G., Moin, A., Burghardt, F. L., Rabaey, J. M., Carmena, J. M. & Muller, R. A wireless and artefact-free 128-channel neuromodulation device for closed-loop stimulation and recording in non-human primates. *Nature biomedical engineering* **3**, 15-26 (2019).

35 Cogan, S. F. Neural stimulation and recording electrodes. *Annu. Rev. Biomed. Eng.* **10**, 275-309 (2008).

36 Kim, T.-i., McCall, J. G., Jung, Y. H., Huang, X., Siuda, E. R., Li, Y., Song, J., Song, Y. M., Pao, H. A. & Kim, R.-H. Injectable, cellular-scale optoelectronics with applications for wireless optogenetics. *Science* **340**, 211-216 (2013).

37 Anikeeva, P., Andalman, A. S., Witten, I., Warden, M., Goshen, I., Grosenick, L., Gunaydin, L. A., Frank, L. M. & Deisseroth, K. Optetrode: a multichannel readout for optogenetic control in freely moving mice. *Nature neuroscience* **15**, 163-170 (2012).

38 Ólafsdóttir, H. F., Carpenter, F. & Barry, C. Task demands predict a dynamic switch in the content of awake hippocampal replay. *Neuron* **96**, 925-935. e926 (2017).

39 Wierzynski, C. M., Lubenov, E. V., Gu, M. & Siapas, A. G. State-dependent spike-timing relationships between hippocampal and prefrontal circuits during sleep. *Neuron* **61**, 587-596 (2009).

40 Euston, D. R., Tatsuno, M. & McNaughton, B. L. Fast-forward playback of recent memory sequences in prefrontal cortex during sleep. *science* **318**, 1147-1150 (2007).

41 Wilber, A. A., Skelin, I., Wu, W. & McNaughton, B. L. Laminar organization of encoding and memory reactivation in the parietal cortex. *Neuron* **95**, 1406-1419. e1405 (2017).

42 Hahn, T. T., Sakmann, B. & Mehta, M. R. Differential responses of hippocampal subfields to cortical up–down states. *Proceedings of the National Academy of Sciences* **104**, 5169-5174 (2007).

43 Tang, W., Shin, J. D., Frank, L. M. & Jadhav, S. P. Hippocampal-prefrontal reactivation during learning is stronger in awake compared with sleep states. *Journal of Neuroscience* **37**, 11789-11805 (2017).

44 Khodagholy, D., Gelinas, J. N. & Buzsáki, G. Learning-enhanced coupling between ripple oscillations in association cortices and hippocampus. *Science* **358**, 369-372 (2017).

45 Gauthier, J. L. & Tank, D. W. A dedicated population for reward coding in the hippocampus. *Neuron* **99**, 179-193. e177 (2018).

46 Aronov, D., Nevers, R. & Tank, D. W. Mapping of a non-spatial dimension by the hippocampal–entorhinal circuit. *Nature* **543**, 719-722 (2017).

47 O'keefe, J. & Nadel, L. *The hippocampus as a cognitive map*. (Oxford: Clarendon Press, 1978).

48 Eichenbaum, H., Kuperstein, M., Fagan, A. & Nagode, J. Cue-sampling and goal-approach correlates of hippocampal unit activity in rats performing an odor-discrimination task. *Journal of Neuroscience* **7**, 716-732 (1987).

49 Trouche, S., Koren, V., Doig, N. M., Ellender, T. J., El-Gaby, M., Lopes-dos-Santos, V., Reeve, H. M., Perestenko, P. V., Garas, F. N. & Magill, P. J. A hippocampus-accumbens tripartite neuronal motif guides appetitive memory in space. *Cell* **176**, 1393-1406. e1316 (2019).

50 Weltman, A., Yoo, J. & Meng, E. Flexible, penetrating brain probes enabled by advances in polymer microfabrication. *Micromachines* **7**, 180 (2016).

51 Patel, J., Schomburg, E. W., Berényi, A., Fujisawa, S. & Buzsáki, G. Local generation and propagation of ripples along the septotemporal axis of the hippocampus. *Journal of Neuroscience* **33**, 17029-17041 (2013).

52 Roux, L., Hu, B., Eichler, R., Stark, E. & Buzsáki, G. Sharp wave ripples during learning stabilize the hippocampal spatial map. *Nature neuroscience* **20**, 845-853 (2017).

53 Pachitariu, M., Steinmetz, N., Kadir, S., Carandini, M. & Harris, K. in *NIPS Proceedings.* (Neural Information Systems Foundation, Inc.).

54 Zutshi, I., Fu, M. L., Lilascharoen, V., Leutgeb, J. K., Lim, B. K. & Leutgeb, S. Recurrent circuits within medial entorhinal cortex superficial layers support grid cell firing. *Nature communications* **9**, 1-15 (2018).

55 Diamantaki, M., Coletta, S., Nasr, K., Zeraati, R., Laturnus, S., Berens, P., Preston-Ferrer, P. & Burgalossi, A. Manipulating hippocampal place cell activity by single-cell stimulation in freely moving mice. *Cell reports* **23**, 32-38 (2018).

56 Musall, S., Kaufman, M. T., Juavinett, A. L., Gluf, S. & Churchland, A. K. Single-trial neural dynamics are dominated by richly varied movements. *Nature neuroscience* **22**, 1677-1686 (2019).

57 Pinto, L., Rajan, K., DePasquale, B., Thiberge, S. Y., Tank, D. W. & Brody, C. D. Task-dependent changes in the large-scale dynamics and necessity of cortical regions. *Neuron* **104**, 810-824. e819 (2019).

58 Clancy, K. B., Orsolic, I. & Mrsic-Flogel, T. D. Locomotion-dependent remapping of distributed cortical networks. *Nature Neuroscience* **22**, 778-786 (2019).

Chapter 5. Conclusion

5.1 Outlook and Roadmap

All the efforts outlined above have improved graphene-based neurotechnologies significantly in the past decade. Simultaneous electrophysiology and two-photon imaging enabled by transparent graphene array has been shown as a promising method for investigating neural activity with high spatiotemporal resolution. Graphene-based closed-loop devices integrating real-time optogenetic modulation and electrical recording can offer unprecedented opportunities for causal investigation of neural circuit functions. Highly precise and selective biochemical sensing can be employed for disease diagnosis and monitoring. Finally, biocompatible graphene-based scaffolds are among the best candidates to facilitate tissue engineering and regenerative medicine.

Building on all these advantages, future studies will continue to further improve graphene-based neurotechnologies and expand the potential of them in both neuroscience research and clinical practices. For instance, recording of single neuron activity remains a challenge for transparent graphene microelectrode arrays. The relatively high impedance of monolayer graphene limits the scalability of graphene microelectrodes to single neuron dimensions. How to reduce the electrochemical impedance while maintaining high optical transmittance is hence a high priority question. In addition, most of the graphene microelectrode arrays demonstrated to-date consist of a small number of electrodes (~16 electrodes) [1]. It is important to develop high-density graphene arrays with hundreds of electrodes to record neural activity with high resolution across large areas in the brain. Next, all the graphene electrode arrays demonstrated to-date are designed to record from the cortical surface and cannot be employed for electrical recording of neural activity from deeper cortical layers or deep brain structures, such as the hippocampus. Penetrating electrode

arrays based on monolayer graphene need to be developed for cross-talk free integration of electrophysiology, simultaneous optical imaging and modulation to study the regions of the brain where surface electrodes cannot reach. Finally, miniaturized wireless systems for recording and stimulation are necessary when freely-moving animal models are involved in behavioral studies such as motor learning. Further research and development are needed to combine wireless operation, data transfer and power telemetry with graphene-based neurotechnologies especially for long-term studies. Therefore, as demanded by advanced neuroscience research, high density electrical recording at single neuron resolution, penetrating electrode arrays, and wireless systems are the next steps in the field of graphene-based neurotechnologies regarding material engineering, device fabrication, and system design.

Going beyond neuroscience research toward potential medical applications, investigation of *in vivo* biocompatibility of graphene has the top priority. All the experiments described in Section 1.3.4 are conducted *in vitro*, however chronic recording calls for further studies of the *in vivo* biocompatibility of graphene-based devices. The longevity of graphene-based neurotechnologies in chronic settings needs to be tested, so that these technologies could be further engineered to minimize both tissue damage and device degradation. Faced with enormous opportunities and challenges, we envision that the worldwide interdisciplinary studies will bring up the best potential of various graphene neurotechnologies in the near future.

5.2 Acknowledgement

We would like to acknowledge Office of Naval Research Young Investigator Award (N00014161253), National Science Foundation (ECCS-1752241, ECCS-1734940), San Diego Frontiers of Innovation Scholars Program, and Kavli Institute for Brain and Mind Innovative Research for funding this research.

Chapter 5 is in part a reprint of Y. Lu, X. Liu, D. Kuzum, Graphene-based neurotechnologies for advanced neural interfaces. Current Opinion in Biomedical Engineering 6, 138-147 (2018). The dissertation author was the first author of this article.

5.3 Reference

1 Thunemann, M., Lu, Y., Liu, X., Kılıç, K., Desjardins, M., Vandenberghe, M., Sadegh, S., Saisan, P. A., Cheng, Q., Weldy, K. L., Lyu, H., Djurovic, S., Andreassen, O. A., Dale, A. M., Devor, A. & Kuzum, D. Deep 2-photon imaging and artifact-free optogenetics through transparent graphene microelectrode arrays. *Nature Communications* **9**, 2035 (2018).